THE FORMATION AND EVOLUTION OF GALAXIES IN AN EXPANDING UNIVERSE

BY

DANIEL CEVERINO-RODRIGUEZ, B.S., M.S.

A dissertation submitted to the Graduate School

in partial fulfillment of the requirements

for the degree

Doctor of Philosophy

Major Subject: Astronomy

New Mexico State University

Las Cruces New Mexico

August 2008

"The Formation and Evolution of Galaxies in an Expanding Universe," a dissertation prepared by Daniel Ceverino-Rodriguez in partial fulfillment of the requirements for the degree, Doctor of Philosophy, has been approved and accepted by the following:

Linda Lacey
Dean of the Graduate School

Anatoly A. Klypin
Chair of the Examining Committee

Date

Committee in charge:

Dr. Anatoly A. Klypin, Chair

Dr. Christopher W. Churchill

Dr. Jon A. Holtzman

Dr. William R. Gibbs

DEDICATION

To Maria Jose, “mi reina”, for all your support and love

and in memory of my grandmother, Teresa.

ACKNOWLEDGMENTS

First of all, I would like to thank my advisor, Dr Anatoly Klypin, for all his support, his advice and dedication. Thank you for teaching me how to do research. I am grateful to Dr Andrey Kravtsov for providing the hydro code. Without that amazing piece of ART, this PhD would have been impracticable. I am also in debt to Dr Nick Gnedin for giving us the wonderful graphics package IFRIT. This research has been infinitely easier with the help of that little genie.

To my parents, back in Sevilla, thank you for all your support and understanding. I know that I went much further than you had imagined. Thank you for being on the other side of the phone every day, sharing all my efforts. Specially, I would like to thank my wife, Maria Jose, for being very patience with me during these years. Thank you for sharing with me this huge adventure, called life. This PhD thesis is also yours.

Octavio also deserves all my gratitude. He paved my first steps in Las Cruces and in the graduate school. Finally, I would like to thank Glenn, Ryan and all "mis amigos" of Las Cruces, for making very enjoyable these 5 years in Las Cruces and in my American adventure. Thank you all.

VITA

February 11, 1978	Born at Sevilla, Spain.
1996-2002	B.S. in Fundamental Physics, "Universidad de Sevilla", Spain.
2003-2006	M.S., Astronomy Department, New Mexico State University, Las Cruces, New Mexico.
2003-2008	Teaching and Research Assistant, Astronomy Department, New Mexico State University, Las Cruces, New Mexico.

PROFESSIONAL AND HONORARY SOCIETIES

2003-2004	Sigma-Xi, Scientific Research Society
2007-2008	American Astronomical Society

HONORS AND AWARDS

2001: Award from the Spanish Goverment for an outstanding research in the department of condensed matter, "Universidad de Sevilla".

2007: Best-poster award in the IAU Symposium "Formation and Evolution of Galaxy Bulges", Oxford, UK.

The Zia Award for an outstanding research by a graduate student in the NMSU Astronomy Department.

2008: The Scoot Murrel Award in recognition of professional development and research accomplishment by a graduate student in the NMSU Astronomy Department.

PUBLICATIONS [or Papers Presented]

Ceverino, D., & Klypin, A. 2007, ArXiv e-prints, 712, arXiv:0712.3285

Ceverino, D., & Klypin, A. 2007, MNRAS, 379, 1155

Ceverino, D., & Klypin, A. 2007, ArXiv e-prints, 710, arXiv:0710.1666

Kacprzak, G. G.; Churchill, C.W., Ceverino, D., Steidel, C. C, Klypin, A. A.; Murphy, M. T., 2008, submitted to ApJ.

Klypin A., Ceverino D., Tinker J., submitted to Review of Modern Astronomy, 2007

Kacprzak, G. G., Churchill, C. W., Steidel, C. C., Ceverino, D., Klypin, A. A., & Murphy, M. T. 2007, ArXiv e-prints, 710, arXiv:0710.4962

Ceverino, D., & Klypin, A. 2007, American Astronomical Society Meeting Abstracts, 211, #111.03

Kacprzak, G., Churchill, C. W., Steidel, C. C., Ceverino, D., Klypin, A., and Murphy, M. T. 2007, American Astronomical Society Meeting Abstracts, 211, 84.01

Widhalm, A. M., Churchill, C., Ceverino, D., & Klypin, A. 2007, American Astronomical Society Meeting Abstracts, 211, #97.19

Churchill, C. W., Klypin, A., Ceverino, D., & Kacprzak, G. G. 2007, American Astronomical Society Meeting Abstracts, 211, #54.05

Churchill, C. W., Kacprzak, G., Ceverino, D., Evans, J., & Widhalm, A. 2006, Bulletin of the American Astronomical Society, 38, 998

Ceverino, D., & Klypin, A. 2005, ArXiv Astrophysics e-prints, arXiv:astro-ph/0503710

FIELD OF STUDY

Major Field: Astronomy

ABSTRACT

THE FORMATION AND EVOLUTION OF

GALAXIES

IN AN EXPANDING UNIVERSE

BY

DANIEL CEVERINO-RODRIGUEZ, B.S., M.S.

Doctor of Philosophy

New Mexico State University

Las Cruces, New Mexico, 2008

Dr. Anatoly A. Klypin, Chair

This PhD thesis is part of an ongoing effort in improving the theory of galaxy formation in a ΛCDM Universe. We include more realistic models of radiative cooling, star formation, and stellar feedback. A special attention has been given to the role of supernova explosions and stellar winds in the galaxy assembly. These processes happen at very small scales (parsecs), but they affect the interstellar medium (ISM) at Kpc-scales and regulate the formation of a whole galaxy.

Previous attempts of mimicking these effects in simulations of galaxy formation use very simplified assumptions. We develop a much more realistic prescription for modeling the feedback, which minimizes any ad hoc sub-grid physics. We start with developing high resolution models of the ISM and formulate the conditions required for its realistic functionality: formation of a multi-phase medium with hot chimneys, super-bubbles, cold molecular phase, and very slow consumption of gas. We find that this can be achieved only by doing what the real Universe does: formation of dense (>10 H atoms cm^{-3}), cold ($T \approx 100$ K) molecular phase, where star formation happens, and which young stars disrupt. Another important ingredient is the effect of runaway stars: massive binary stars ejected from molecular clouds when one of the companions becomes a supernova. These stars can move to 10-100 parsecs away from molecular clouds before exploding themselves as supernovae. This greatly facilitates the feedback. Once those effects are implemented into cosmological simulations, galaxy formation proceeds more realistically. For example, we do not have the overcooling problem. The angular momentum problem (resulting in a too massive bulge) is also reduced substantially: the rotation curves are nearly flat. The galaxy formation also becomes more violent. Just as often observed in absorption lines studies, there are substantial outflows from forming and active galaxies. At high redshifts we routinely find gas with few hundred km s^{-1} and occasionally $1000-2000$ km s^{-1}. The gas has high metallicity, which may exceed the solar metallicity. The temperature of the gas in the outflows and in chimneys can be very high: $T = 10^7 - 10^8$ K. The density profile of dark matter is still consistent with a cuspy profile. The simulations reproduce this picture only if the resolution is very high: better than 50 pc, which is 10 times better than the typical resolution in previous cosmological simulations. Our simulations of galaxy formation reach a resolution of 35 pc.

At the time in which most of the mass is assembled into a galaxy, a big fraction of the gas in the galactic disk has already been converted into stars. Therefore, we can assume that the remaining gas does not affect the evolution of the stellar distribution. In this approximation, all gasdynamical processes are neglected and we treat a galaxy as a pure collisionless system. Then we use N-body-only models to study the long-term evolution of an already formed stellar disk. During this evolution, the disk develops a bar at the center through disk instabilities. We find dynamical resonances between the bar and disk or halo material. These resonances can capture stars near certain resonant orbits. As a result, resonances prevent the evolution of the stars trapped around these orbits.

CONTENTS

LIST OF TABLES

LIST OF FIGURES

1 INTRODUCTION

Since Charles Messier (1730-1817) published his *Catalogue of Nebulae and Star Clusters* (1781), the origin of some of these "fuzzy" spiral nebulae has been a mystery for many generations of astronomers. A key milestone on the nature of these nebulae and the size of the Universe was dubbed *The Great Debate* (1920) between Harlow Shapley (1885-1972) and Heber Curtis (1872-1942). In the traditional picture, supported by Shapley, these spirals were clouds of gas inside our Galaxy: the Milky Way (MW). Therefore, our Galaxy was the entire Universe. In contrast, Curtis supported the revolutionary idea that these nebulae were other galaxies, similar to the Milky Way but at incredible distances. As a result, the Universe was much larger than was previously thought and it contained countless galaxies separated by large distances. The idea of these *Island Universes* finally was confirmed with the measurements of their distances. Walter Baade (1893-1960) and Edwin Hubble (1889-1953) identified variable stars in several spiral nebulae, including the Andromeda Galaxy. Their estimated distances turned to be much greater than the size of the MW in Shapley's model.

Since then, our knowledge about galaxies has grown exponentially. Nearby galaxies have been observed in detail. Their photometric properties, kinematics and morphologies have been characterized and classified (de Jong & van der Kruit, 1994; Persic et al., 1994; Tully & Fisher, 1977; Courteau, 1997; Kennicutt et al., 1994; Blanton et al., 2003, etc) Today, we know that galaxies consist of stars, the interstellar medium (ISM), mainly composed of gas in different phases, and dark matter. Evidence for the content of dark matter in galaxies comes from observations of rotation curves at large galactocentric radii (Rubin et al., 1980). At large distance the galaxy rotation predicted using the observed amount of stars and gas should decline with radius. However, observed rotation curves do not decline, indicating that there are large amounts of mass at large radii. Today it is generally accepted that galaxies are embedded in halos of dark matter, although the nature of this dark matter is still unknown. This current picture of galaxies gives strong insights about the present conditions and the relevant physics of present-day galaxies ($z \sim 0$). Galaxies are well-evolved objects that started to form several billions of years ago (Wood, 1992). As a result, we still need detailed observations of very distant galaxies at high redshifts to look back in time into the main epoch of galaxy formation ($z > 2$).

In spite of all the current knowledge about galaxies, fundamental questions remain unanswered: How did galaxies form? How did they evolve to the galaxies that we observe today? In order to address these questions from first principles, a model for galaxy formation needs to start from the small fluctuations in density in the early Universe, when the Universe was only a few million years old. Such model needs to follow the growth of these fluctuations and their evolution until they form galaxies. In other words, we need to follow the formation of galaxies in a cosmological context. We should link galaxy formation with the evolution of the Universe and the formation of cosmological structures.

In traditional models of the formation of cosmological structures, ordinary matter ("baryons"), which emits and absorbs light, passively follows the evolution of the dark matter. This should be corrected, if we want to make a realistic theory at the scales in which galaxies form. At these scales, the physics of baryons becomes important. The modeling of astrophysical processes, such as star formation and stellar feedback becomes necessary. These processes happen at very small scales (e.g. 1-10 pc), but they affect larger scales. For example, metals synthesized in stars and ejected in supernova explosions enrich and modify the conditions in the interstellar medium (Kpc scales) and in the intergalactic medium (Mpc scales). There is a complex interplay between small-scale astrophysical processes and large-scale cosmological processes (e.g., the motion of gas in cosmic filaments). Predictions are much less certain even on large scales, and on the scales of galaxies they become absolutely exciting but qualitatively uncertain. I argue that a significant effort – comparable to what cosmology has done with the gravitational dynamics – must be devoted to the theory of galaxy formation.

2 THE FORMATION OF COSMOLOGICAL STRUCTURES IN AN EXPANDING UNIVERSE

Here I present a brief overview of the current state of the part of cosmology that deals with the formation of different structures in the hierarchical model. Modern cosmology covers a vast range of physical phenomena and scales ranging from large scales, which are dominated by gravitational dynamics, to scales interior to galaxies, where the physics of baryons plays an important role.

Driven by both observations and theory, the gravitational dynamics has made remarkable progress, giving rise to the notion of precision cosmology. I discuss such characteristics as the power spectrum, mass function and halo concentration, which are predicted by the theory with the accuracy of few percent. Finally, other properties of the internal dynamics of dark matter halos: the angular momentum and virial properties, are described at the end of the section. All these properties give the basis from which a successful theory of galaxy formation should be developed.

2.1 The Field of Structure Formation

The current cosmological paradigm, the ΛCDM Universe, is remarkably successful on scales larger than ∼Megaparsec. ΛCDM cosmology predicted the amplitude and spectrum of fluctuations in the cosmic microwave background (CMB) and the spectrum of large-scale fluctuations in the distribution of galaxies (Bardeen et al., 1987; Holtzman, 1989). Those predictions were later verified by observational measurements (Netterfield et al., 2002; Tegmark et al., 2004; Cole et al., 2005; Spergel et al., 2007). The recent success of theoretical cosmology is impressive, but one should not forget that the current model is the result of a long process of selection and perfection of competing theoretical models. Many models were not successful and were rejected. Historically, the ΛCDM model had not been a favored model. The main objection to the model involves an ad-hoc component – the cosmological constant, or the dark energy. The ΛCDM model started to "win" well before the CMB measurements became available. A combination of the measurements of the Hubble constant (thus, the age of the Universe) and the abundance of high redshift objects (clusters of galaxies in particular) left a choice of either the ΛCDM model (a flat universe with low density of the dark matter) or an open CDM model (a model with negative curvature). Then, the first measurements of the position of the first acoustic peak in the CMB spectrum (de Bernardis et al., 2000; Bond et al., 2000) eliminated the open CDM model.

To a large degree, the theory is successful because it is based on well-understood and simple physics: the growth of linear perturbations. We should not underestimate the effort put into making the physics "well-understood": it took more than 30 years (e.g., Lifshitz & Khalatnikov, 1963; Eisenstein & Hu, 1999) to bring about this understanding. Still, if we compare this part of cosmology with other fields of astronomy such as star formation or stellar evolution, it is clear that linear perturbations in cosmology deal with simple physics. This is why theoretical predictions can be very accurate.

The field of structure formation (quasi-linear and strongly non-linear fluctuations) is split into two almost independent parts: physics of clustering of the dark matter and the theory of the galaxy formation. Gravitational dynamics is a complicated field in comparison with the growth of linear perturbations. Yet it is much simpler than galaxy formation. Thus, statistics and properties of structures in the dark matter can be predicted with extraordinary accuracy. The gravitational dynamics of the dark matter is actually a complicated field. The structures in general are neither spherical nor stationary. There is substantial coupling of different modes (scales) with long waves substantially affecting small-scale dynamics. The range of scales is astounding. For example, in modern computer simulations it is not unusual to have a dynamic range of 100,000 or even more. Reducing this dynamical range may result in incorrect results. These are the reasons why it is very difficult to make analytical predictions in this field. Indeed, there are very few useful analytical solutions.

There are two factors that dramatically simplify the theory. (1) In cosmology we deal with collisionless dynamics. Mathematically this means solving the Vlasov-Poisson system of equations for which the phase-space density is preserved along the trajectory of each particle. Physically, this means that we do not have complicated processes such as two-body scattering or the gravothermal catastrophe. (2) Long waves are only weakly affected by the short-scales: what happens on small scales does not significantly affect perturbations on large scales. Because of this weak coupling, one can simulate a relatively small volume and obtain reasonably accurate results. How small? This depends on required accuracy and particular properties studied. There is no a priori rule for how large the volume should be. This is found only by comparing results from different volumes.

The theory of galaxy formation, which involves complicated physics of gas and star formation, is still in a very preliminary stage. Here the situation is very different compared to the dynamics of the dark matter. The accuracy of the results is not much of an issue: one does not worry about the accuracy, when it is not clear whether all the basic physics is included. So, the main thrust is to identify and include the most important physical processes. The complexity of the problem derives from the fact that small-scale phenomena affect large scales in a very profound way. For example, the motions and metallicity of gas in a galactic halo ($\sim$ 100 kpc scales) are affected by the energy released in regions of active star formation in the galaxy itself (few parsecs scales). In turn, the physics on parsec scales is affected by the star formation processes and by the environment, which are on scales well below a parsec. In other words, the minimum scale is not clear, but it must be included in the analysis to produce the correct treatment of gas and stars on large scales. The situation may not be as hopeless as it looks: there should be a minimum scale, which is sufficient for the accurate description of the main physical processes responsible for the formation of galaxies and for the large-scale dynamics of baryons inside galaxies.

Because of the complexities and uncertainties in galaxy formation, it is highly unlikely that predictions of galaxy formation will be used to constrain the parameters of cosmological models. Fluctuations in the CMB, geometrical tests (such as distances to SNI), and results from dark matter clustering are the main tools for testing the global parameters of cosmological models.

The theory of non-linear structures has different components. (1) *Numerical simulations* play an important role. Sophisticated codes were developed to simulate different aspects of the theory (e.g., ART - Kravtsov et al (1997); GADGET - Springel et al. (2001) ; GASOLINE - Wadsley et al. (2004) ; Enzo - O'Shea et al. (2004)). To a large degree, the progress in the field was driven by numerical simulations. In turn, numerical effort is driven by observational needs and by computer hardware. Numerical simulations have one limiting factor: they do not provide explanations. For example, simulations predict that the density profiles of dark matter halos are reasonably well fit by the Navarro-Frenk-White (NFW, 1997) approximation. Yet, the simulations do not tell us why this is the case.

(2) *Analytics* are important because they provide understanding of what occurs in simulations. Unfortunately, analytical models are very difficult to construct. There are two special cases: the halo mass function and the quasi-linear regime of clustering. There has been a dramatic improvement in both statistics from traditional-style approximations. In the case of quasi-linear clustering, one expands the fluctuations using perturbation theory and collects leading terms. The calculations are tedious but tractable. Predictions were tested against N-body simulations with impressive results (Crocce & Scoccimarro, 2007). In fact, some simulations were not accurate enough and were re-done. The mass function is estimated using a different type of approximation. Press & Schechter (1974) derived the scaling law for the mass function, which is based on Gaussian statistics. The scaling is then used with additional fitting factors to approximate the halo mass function. Results depend on the particular choice (and ideas) for the extra fitting factors (Sheth & Tormen, 1999; Jenkins et al., 2001).

(3) There is another type of prediction in cosmology, which is called *semi-analytics* (e.g., Kauffmann et al., 1994; Somerville & Primack, 1999; Benson et al., 2003). A semi-analytical model is not an approximation in the usual sense:

It does not make an analytical approximation of any law of physics nor of any equations. A semi-analytical model is a set of prescriptions, which guess the outcome of complicated (and often poorly understood) processes. For example, one assumption is that the collision of two spiral galaxies of comparable mass (major merger) results in the formation of an elliptical galaxy. In reality, this may not be true, but there is no way of testing it within the framework of the semi-analytical models. Semi-analytical models have another limitation; they cannot be used to learn about new physical phenomena. If the rules include only spiral and elliptical galaxies, the results cannot address the existence of other types of galaxies (e.g., lenticular or barred galaxies). Semi-analytical models are often criticized for having too many free parameters: this is not right. It is an ambitious prospect to explain the whole universe, and extra 200 free parameters is a small price to pay. Semi-analytical models can be a powerful tool, if used cautiously and in conjunction with numerical simulations. Semi-analytical models are excellent tools for making mock catalogs for testing statistical effects or for designing observational strategies.

Results of numerical simulations are the main goal of this review. Numerical simulations in cosmology have a long history and numerous important applications. Such work began in the 60s (Aarseth, 1963) and 70s (Peebles, 1970) with simple problems solved using N-body codes with a few hundred particles. Peebles (1970) studied the collapse of a cloud of 300 particles as a model of cluster formation. After the collapse and virialization the system resembled a cluster of galaxies. Those early simulations of cluster formation, though they produced cluster-like objects, pointed the first problem – a simple model of an initially isolated cloud (top-hat model) results in a density profile which is too steep (power-law slope -4) as compared with real galaxy clusters (slope -3). Gunn & Gott (1972) introduced the notion of secondary infall in an effort to solve that problem. Another keystone work of those times was performed by White (1976), who studied the collapse of 700 particles with different masses. He showed that if one distributes the mass of a cluster into individual galaxies, two-body scattering would result in mass segregation not compatible with observed clusters. This was another manifestation of the dark matter in clusters, demonstrating that inside a cluster the dark matter cannot reside inside individual galaxies.

Survival of substructures in galaxy clusters was another problem addressed by White (1976). It was found that lumps of dark matter, which in real life may represent galaxies, do not survive in the dense environment of galaxy clusters. White & Rees (1978) argued that the real galaxies survive inside clusters because of energy dissipation by the baryonic component. That point of view was accepted for almost 20 years. However, recently it was shown that energy dissipation does not play a dominant role in the survival of galaxies and that dark matter halos are not destroyed by tidal stripping and galaxy-galaxy collisions inside clusters

(Klypin et al., 1999; Moore et al., 1999). The reason early simulations yielded incorrect results was purely numerical: they did not have high enough resolution and the integration of trajectories was not accurate enough. But 20 years ago, it was physically impossible to perform a simulation with sufficient resolution; even if at that time we had present-day codes, it would have taken about 600 years to make one run.

Starting in the mid 1980s, the field of numerical simulations began to bloom: new numerical techniques were invented, old ones were perfected. The number of publications based on numerical modeling skyrocketed. To a large extent, this has changed our way of doing cosmology. Instead of questionable assumptions and handwaving arguments, we have tools for testing our hypotheses and models. As an example, we mention two analytical approximations that were validated by numerical simulations. The importance of both approximations is difficult to overestimate. The first is the Zeldovich approximation, which paved the way for understanding the large-scale structure of the galaxy distribution. The second is the Press & Schechter (1974) approximation, which gives the number of objects formed at different scales at different epochs. Both approximations cannot be formally proved. The Zeldovich approximation is not applicable for hierarchical clustering because it works only with smooth perturbations that have a truncated spectrum. Nevertheless, numerical simulations have shown that even for hierarchical clustering this approximation can be used with appropriate filtering of the initial spectrum. The Press-Schechter approximation and its siblings are also difficult to justify without numerical simulations. The approximation utilizes the initial spectrum and linear theory, but then (a very long jump) it predicts the number of objects at a very nonlinear stage. Because it is not based on any realistic theory of nonlinear evolution, its justification is based solely on numerical simulations.

2.2 Evolution of Density Perturbations

Figure 2.1 shows the evolution of the power spectrum of perturbations in a large simulation of the ΛCDM model: 1Gpc box with 1024^3 particles. Longest waves in the simulation have small amplitude and must grow according to the linear theory. This indeed is the case, as seen in the bottom panel. Note that a small dip $\sim -2\%$ at $k = 0.05 - 0.07h^{-1}$Mpc is what the quasi-linear theory of perturbations predicts (Crocce & Scoccimarro, 2007). The plot also shows the main tendency: in the non-linear stage the perturbations at the beginning grow faster than the predictions of the linear theory (we neglect a possible small negative growth extensively discussed by Crocce & Scoccimarro (2007)). At later stages the growth slows down, which is seen as bending down of $P(k)$ at high

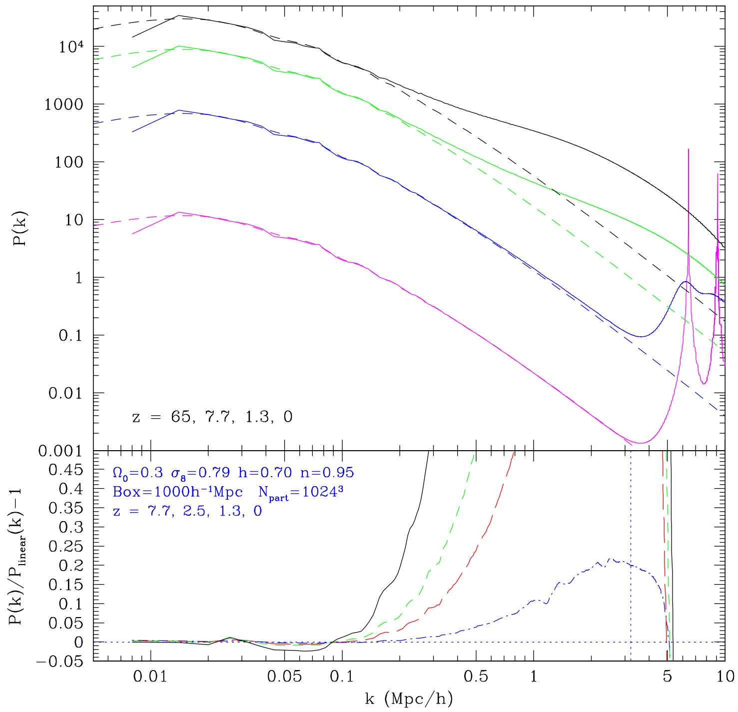

Figure 2.1 Growth of perturbations in the ΛCDM model. The top panel shows the evolution of the power spectrum $P(k)$ in the simulation (full curves) as compared with the linear theory (dashed curves). From bottom to top the curves correspond to decreasing redshifts: the lowest curve is for the initial conditions ($z = 65$) and the top curve is for $z = 0$. The bottom panel shows deviations from the predictions of the linear theory. Fluctuations on large scales (small k's) grow according to the linear theory. The dot-dashed ($z = 7.7$) and the long-dashed curves ($z = 2.5$) show that non-linear evolution increases the power spectrum on all scales proceeding from high k, where the non-linear effects are strongest, to low k, where the effects are weakest. Vertical dotted line shows the Nyquist frequency of particles.

frequencies (Peacock & Dodds, 1996). The deviation in the first harmonic (the smallest k) is due to small statistics of the longest waves. Two strong spikes at large k's are above the Nyquist frequency: the N-body code does not "see" them.

Figure 2.2 shows the distribution of the dark matter in a $\sim 10h^{-1}$Mpc slice of a 1024^3 particles simulation. The simulation used a special technique – constrained simulations – to set initial conditions, when long waves are taken for the distribution of matter and velocities of galaxies in the real Universe, but small-scale perturbations are from a realization of the ΛCDM model. Details can be found in Klypin et al. (2003). Because the long waves are taken from the observations, the simulation has large-scale features in the right places. In this figure our Galaxy (or a candidate for MW) is in the middle in a relatively weak filament. Just above it at a distance of about $10h^{-1}$Mpc is the "Virgo" cluster. Other well-known objects are also marked in the plot. Dominating the field are dark matter halos, which are seen as tight bright round knots in the figure. Yet, the whole distribution is a complex web of filaments, voids, and halos.

2.3 Halo Mass Function and Halo Concentration

For a given set of cosmological parameters, the number of dark matter halos at different redshifts is defined by the shape and amplitude of the initial density field, making observational measurements of the mass function a powerful constraint on cosmological parameters, primarily the matter density Ω_m and the amplitude of the power spectrum σ_8 defined at scale the $8h^{-1}$Mpc (scale of galaxy clusters). The evolution of cluster statistics with time is a primary method for measuring the equation of state of dark energy w, a leading problem in observational cosmology and fundamental physics. Precise theoretical understanding of the mass function and its dependence on cosmology and redshift are required by upcoming programs that seek to use the abundance of clusters to constrain cosmology. In addition to constraining cosmological parameters, dark matter halos are also the key to our understanding of galaxies. Precise interpretation of observational data requires precise theoretical predictions for the properties of dark matter halos: their abundance, their bias, and their density profiles.

The standard for a precise determination of the mass function from simulations was set by Jenkins et al. (2001), who improved on earlier analytic predictions by Press & Schechter (1974); Lee & Shandarin (1998); Sheth & Tormen (1999). The primary result of the Jenkins study was a fitting function accurate to $\sim (10-20)\%$. The authors also claimed that this function was universal for variations in cosmology and redshift. Although encouraging, efforts to constrain dark energy from galaxy clusters require theoretical uncertainty of order 5%, a level of precision achieved by Warren et al. (2006) for a fixed cosmology at $z = 0$. Tinker et al.

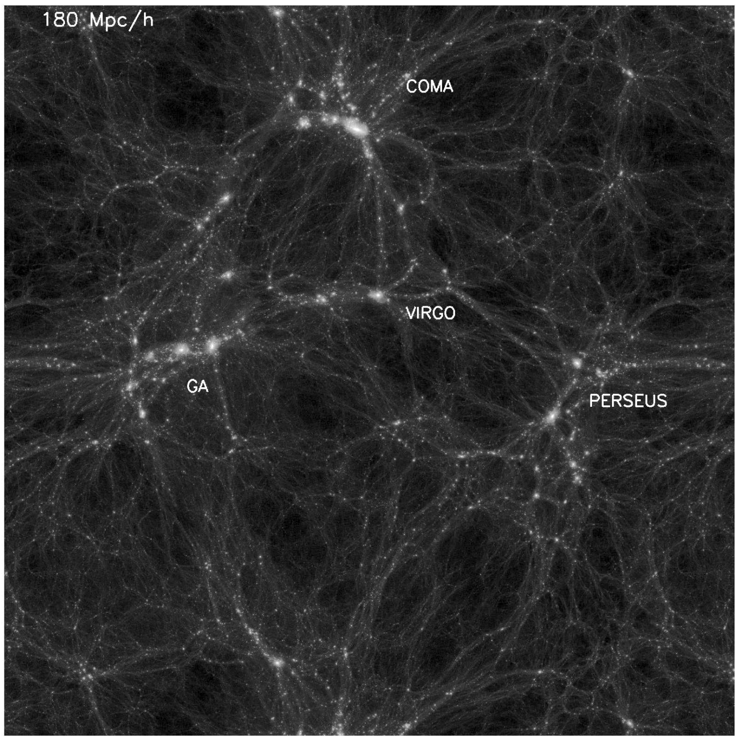

Figure 2.2 Distribution of the dark matter in simulations constrained by the distribution and motion of galaxies in the real Universe. An analog of our Galaxy is a tight small halo in the center of the plot. The distribution of dark matter is a hierarchy of filaments, voids, and halos

(2008) use a large set of cosmological N-body simulations to estimate the halo mass function with accuracy better than 5% over a mass range of five orders of magnitude. Their simulation set spans six orders of magnitude in volume and has different cosmologies and redshifts in the analysis.

Figure 2.3 shows an example of the halo mass function of the so-called millennium simulation (Springel et al., 2005). This simulation was a benchmark at that time. it contains $\sim 10^{10}$ dark matter particles in a box of 500 h^{-1} Mpc on a side. As a result, the halo mass function extends from dwarf galaxy halos, 10^{10} $\mathrm{M}_\odot$, to super galaxy cluster halos, 10^{16} $\mathrm{M}_\odot$. Some features in this plot emphasize how hierarchical clustering works. Low-mass halos form first at very high redshift and more massive structures form later from the clustering and merging of smaller objects. The strongest evolution in the number density of dwarf halos ($M < 10^{11}h^{-1}\mathrm{M}_\odot$) happens at $z > 3$. Even the number density of galaxy-size halos ($M < 10^{12}h^{-1}\mathrm{M}_\odot$) evolve very little after $z = 1.5$. This has important implications for galaxy formation. It shows that the main epoch for galaxy assembly happened before $z = 1.5$.

Concentration is another important property of a dark matter halo. It is defined as the ratio of the virial radius, r_{vir}, to the radius r_s, where the slope of the density profiles is equal to -2 (core radius in the NFW approximation): $c_{\mathrm{vir}} = r_{\mathrm{vir}}/r_s$. The reference point for halo concentrations is the paper by Bullock et al. (2001a), who parameterized the halo concentration as a function of mass and redshift:

$$c_{\mathrm{vir}}(M, z) \propto (1+z)^{-1}, \quad \text{for M=constant} \tag{2.1}$$

$$c_{\mathrm{vir}}(M, z=0) \propto M^{-0.13}, \quad \text{for distinct halos} \tag{2.2}$$

It predicts that halos of the same mass are less concentrated at higher redshifts and that the median c_{vir} of a population of distinct halos decreases with growing mass (Figure 2.4).

2.4 Angular Momentum

It is convenient to characterize the rotation of a dark matter halo using a dimensionless spin parameter λ:

$$\lambda = \frac{J|E|^{1/2}}{GM^{5/2}}, \tag{2.3}$$

here J is the angular momentum, E is the total energy, and M is the mass of a halo. The value of the spin parameter roughly corresponds to the ratio of the angular momentum of an object to that needed for rotational support. Typical values of the spin parameter of individual halos in simulations are in the range

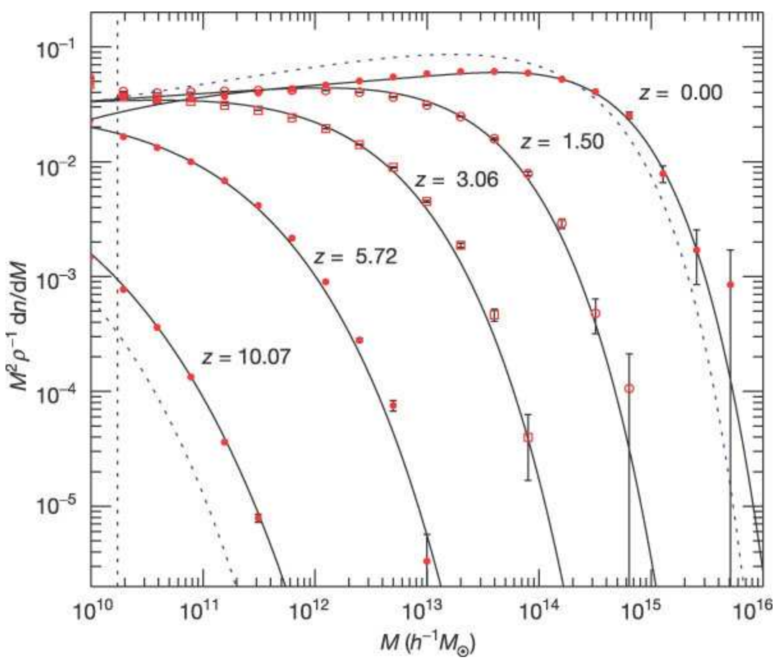

Figure 2.3 Halo mass function in the millennium simulation (Springel et al., 2005) for different redshifts. The function $n(M, z)$ gives the comoving number density of halos less massive than M. ρ is the main density of the Universe. The vertical dotted line shows the mass resolution limit. Solid lines are predictions from the Jenkins et al. (2001) fit and dashed lines show the Press-Schechter approximation at $z = 10.07$ and $z = 0$.

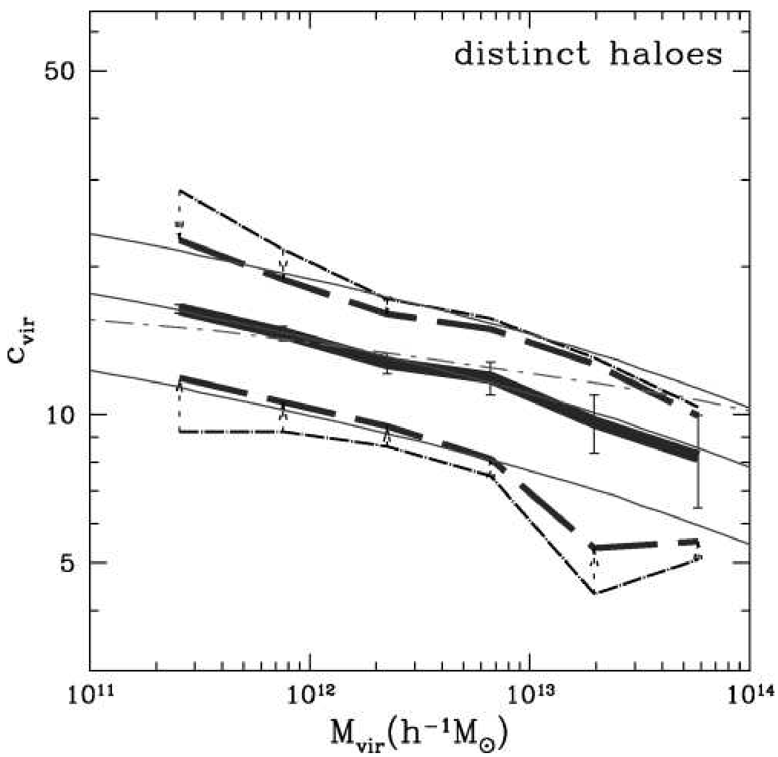

Figure 2.4 Concentration versus mass for distinct halos at z=0 in Bullock et al. (2001a). The thick solid curve shows the median value. The error bars show the Poisson errors in each mass bin. The outer dot-dashed curves cover 68% of the values. The inner dashed curves represent the intrinsic scatter in c_{vir}, after removing all random scatter. The central and outer thin solid lines are the theoretical expectations.

0.02 to 0.11 (e.g., Barnes & Efstathiou, 1987). The distribution of spin parameters in N-body simulations is well described by the log-normal distribution:

$$p(\lambda)d\lambda = \frac{1}{\sigma_\lambda\sqrt{2\pi}}\exp\left(-\frac{\ln^2(\lambda/\bar{\lambda})}{2\sigma_\lambda^2}\right)\frac{d\lambda}{\lambda}, \tag{2.4}$$

where $\bar{\lambda} = 0.037$ and $\sigma_\lambda = 0.51$ (e.g., Bett et al., 2007). Figure 2.5 shows an example for the simulations of Bullock et al. (2001b). However, there are indications that the log-normal distribution underestimates the number of halos with small spin parameters (Bett et al., 2007).

It is clear that the distribution of the spin parameter is very stable: it does not depend on halo mass or redshift (Bullock et al., 2001b; Vitvitska et al., 2002; Hahn et al., 2007). Spins of neighboring halos do not correlate (e.g., Hahn et al., 2007): the source of the angular momentum (be it the tidal torques or satellite accretion) does not have a long-distance memory. There are some correlations of the halo spin. The direction of the spin tends to be parallel to the minor axis of halo mass distribution (e.g., Bett et al., 2007), though the distribution of disalignment angles is quite broad. Halos with larger spin are more clustered (Bett et al., 2007).

In spite of the fact that the overall distribution of spins does not change with time, each individual halo changes its angular momentum quite substantially (Vitvitska et al., 2002; Hetznecker & Burkert, 2006; D'Onghia & Navarro, 2007). Figure 2.6 shows the evolution of spin parameters and masses for three halos with mass $\sim 10^{12}h^{-1}\mathrm{M}_\odot$ at $z = 0$. The spin tends to increase to very large values of $\lambda = 0.05 - 0.1$ when a large satellite is accreted. Figure 3 in D'Onghia & Navarro (2007) gives two more examples of this process: λ increased by factor of three, when either a major merger (mass ratio 1:3 of satellite to primary) or a 1:15 merger occurred. Interpretation of the subsequent evolution is still controversial. Vitvitska et al. argued that the decline of the spin after merger is caused by accretion of satellites with small net angular momentum resulting in dilution of the large initial angular momentum over bigger mass. D'Onghia & Navarro argue that the decline "is due to the internal redistribution of mass and angular momentum that occurs during virialization". However, if a system does not grow and does not interact with its environment, then its total energy, mass, and angular momentum are preserved. Because the spin parameter depends only on those quantities, no internal process (including virialization) can change it. The angular momentum can be lost to immediate environment of a halo through tidal interactions. Whatever is the explanation of the subsequent evolution of the angular momentum, all the results agree that the angular momentum dramatically increases during the merging process and it stays in the system for a long time. This may have an effect on the angular momentum of gas during this merging process: if the gas has large angular momentum, it will change the final angular momentum of the

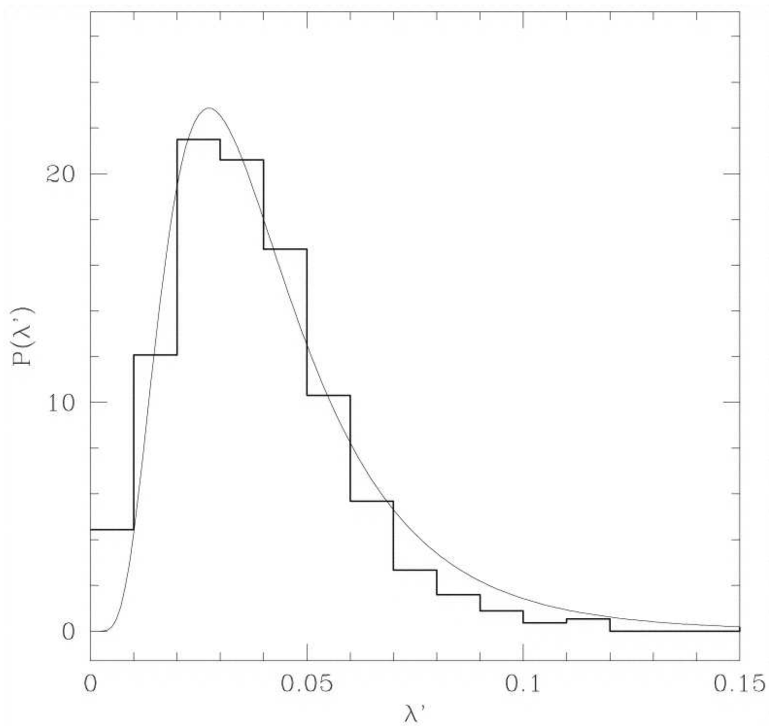

Figure 2.5 The distribution of spin parameters of the halos in the simulations of Bullock et al. (2001b). The thin curve is a log-normal distribution with $\bar{\lambda} = 0.035$ and $\sigma_\lambda = 0.50$. However, there are indications that the log-normal distribution underestimates the number of halos with small spin parameters (Bett et al., 2007). Nevertheless, this distribution is very stable: it does not depend on halo mass or redshift.

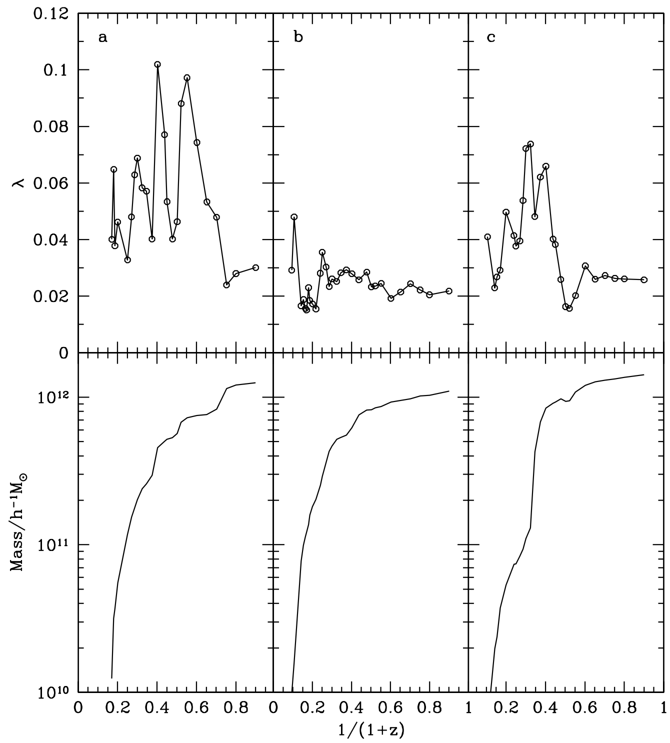

Figure 2.6 Three examples of evolution tracks of Milky-Way galaxy-size halos in N-body simulations from Vitvitska et al. (2002). All halos show fast mass growth at high redshifts. At that epoch their spin parameters change very violently, but subsequently they mostly decline as the mass growth slows down.

galaxy forming from the gas. If we further assume that large mergers produce ellipticals, then ellipticals should have larger angular momentum.

2.5 Structure of Dark matter Halos

There are numerous aspects regarding the internal structure of dark matter halos. Spherically averaged density profiles have probably the most well studied statistics. The density profile is reasonably accurately approximated by the NFW profile: $\rho(r) = \rho_o/x(1+x)^2$, where $x = r/r_s$. Here ρ_0 and r_s are two free parameters, which can be replaced by, say, virial mass and concentration. The central

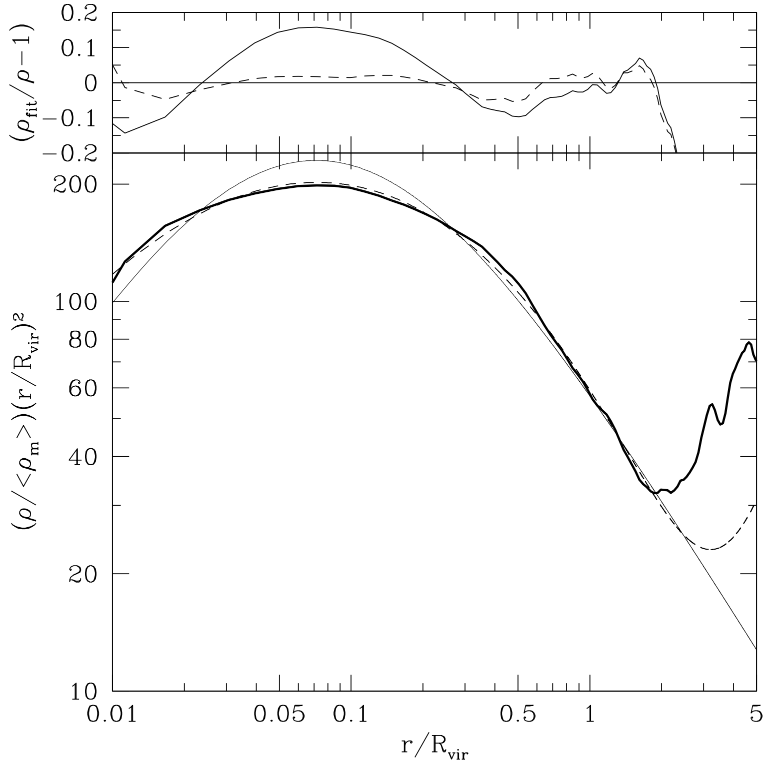

Figure 2.7 Comparison of the NFW and the Einasto fits from Prada et al. (2007). The thick full curve in the bottom panel shows the average density for halos with mass $< M >= 3 \times 10^{11} h^{-1}\mathrm{M}_{\odot}$. The Einasto fit is the dashed curve. The NFW fit is presented by the thin full curve. The top panel shows the errors of the fits. The full curve is for the NFW approximation, and the dashed curve is for the Einasto fit. In outer regions $r = (0.3 - 2)R_{\rm vir}$ both fits have practically the same accuracy. Both fits start to fail at larger distances. Overall, the Einasto approximation provides a remarkable accurate fit.

slope of the density profile is a very much debated characteristics. For the NFW it is $\gamma = -1$. Recent simulations of Diemand et al. (2007) with $\sim 1/4$ billion particles give $\gamma = -1$ at 0.34% of $r_{\rm vir}$. The problem with the NFW is that on average it overestimates by $\sim 20\%$ the density in the region $r \approx r_s$. Figure 2.7 shows the average profile for halos with mass $< M >= 3 \times 10^{11} h^{-1} {\rm M}_\odot$ (Prada et al., 2007). The NFW provides a reasonable fit over a wide range of radii. Still, it is not accurate even on average. A more accurate fit is provided by the three parameter Einasto profile (Navarro et al., 2004; Prada et al., 2007; Gao et al., 2007):

$$\rho = \rho_s \exp\left(-\frac{2}{\alpha}[(\frac{r}{r_s})^\alpha - 1] \right). \tag{2.5}$$

On average the parameter α correlates with halo mass: the larger is the mass the larger is α. Combining results presented by Prada et al. (2007) and by Gao et al. (2007) we get the following approximation for $\alpha(M)$ for halos at $z = 0$:

$$\alpha = 0.155 + 0.015 \log(M/10^{12} h^{-1} {\rm M}_\odot). \tag{2.6}$$

The steep increase in the density of the dark matter results in significant tensions with observations of rotation curves of dwarf irregular galaxies (e.g., de Blok et al., 2001). There are some cases where observed rotation curves measured by the motion of neutral hydrogen, molecular gas (Simon et al., 2005), or Hα emission (de Blok et al., 2001) fall below theoretical predictions and, if naively interpreted, predict constant density core for the dark matter. This is the so called cores vs. cusps problem. These contradictions with the theoretical predictions are not universal: in a large fraction of measured galaxies the NFW profile gives a match to observations (Hayashi et al., 2004; Simon et al., 2005).

So far the main contenders for the resolution of the problem are different effects related with the motion of gas in the central regions of galaxies. Valenzuela et al. (2007) argue that cold gas in the central regions of dwarf spheroids moves slower than what would be naively expected. Additional support for the gas is provided by a combination of few factors: small-scale non-circular motions and pressure support due to low-level star formation (measured in these galaxies), and large-scale distortions in the gravitational potential produced either by weak stellar bars or non-spherical dark matter halos. Recently, Mashchenko et al. (2007) blamed violent motions in the gas during early stages of galaxy formation for flattening the dark matter cusp. It is a possibility, though it is not clear how efficient is the process and how realistic are the processes leading to such violent gas motions.

Interestingly enough, it seems that dwarf spheroidal galaxies, which are typically smaller than dwarf irregulars, do not have much of the problem. Recent extensive measurements of random velocities of stars in many dwarf spheroids in the Local Group are coming along with the theoretical expectations of cuspy dark matter profiles (Walker et al., 2007).

Figure 2.8 illustrates the overall dynamical structure of dark matter halos (see Cuesta et al. (2007) for details). All the curves were normalized to the virial values for each halo. Therefore, we are looking at relative differences. The plots show that massive halos are less concentrated than small halos (bottom panels). The velocity dispersions (top panels) indicate that larger halos dynamically dominate their environment: rms velocities in the environment of clusters are much smaller than in their interiors. Dwarf halos are different in that respect: just outside their formal radii the velocities start to increase.

Results in this figure give us an important lesson: There is nothing very special about the virial radius. There are no discontinuities, there is no "truncation" or a boundary of a halo, and halo properties smoothly change when we cross the formal virial radius. Prada et al. (2007) and Cuesta et al. (2007) made a detailed analysis of outer regions of halos with a conclusion that halos of small mass ($\sim 5{\times}10^{12}h^{-1}\mathrm{M}_{\odot}$ and below) may extend 2-3 times beyond their formal virial radius. They measure the average radial velocity of dark matter as a function of distance. Figure 2.9 shows the profiles for halos of different mass. The cluster-size halos behave as expected: just outside their virial radius there is a broad region where matter falls into the central halo as indicated by negative radial velocities. Dwarf halos gave a surprise: there is no infall region and on average the matter does not fall.

It should be remembered that the formal virial radius is not estimated using any obvious virial relations. One may think of using the virial ratio $2K/U - 1$, but it appears not to be very useful in practice. So, to large degree, the "virial radius" in cosmology is mostly convention. This also explains why there are many definitions of halo radii. Typically one uses some constant overdensity radius. Early simulations indicated that the radius of overdensity 178 is close to the virial radius. Thus, the radius of overdensity 200 ($\approx$ 178) became the virial radius. The reason why this was a good approximation is simply coincidental: the early simulations were mostly done for cluster-size halos and, indeed, for those masses the virial radius is close to the radius of overdensity 200. The early models were flat models without the cosmological constant. Models with the cosmological constant have produced significant confusion in the community. The top-hat model must be modified to incorporate the changes due to the different rate of expansion and due to the different rate of growth of perturbations. That path produced the so called virial radius, which for the standard cosmological model gives the radius of overdensity relative to matter of about 340. Still, a large group of cosmologists uses the old overdensity 200 relative to the critical density even for the models with the cosmological constant.

Cuesta et al. (2007) argue that the radius inside which the radial velocity is zero – the static radius – is a better approximation for the virial radius. In the sense of dynamics the static radius is the virial radius. Here the system is stationary

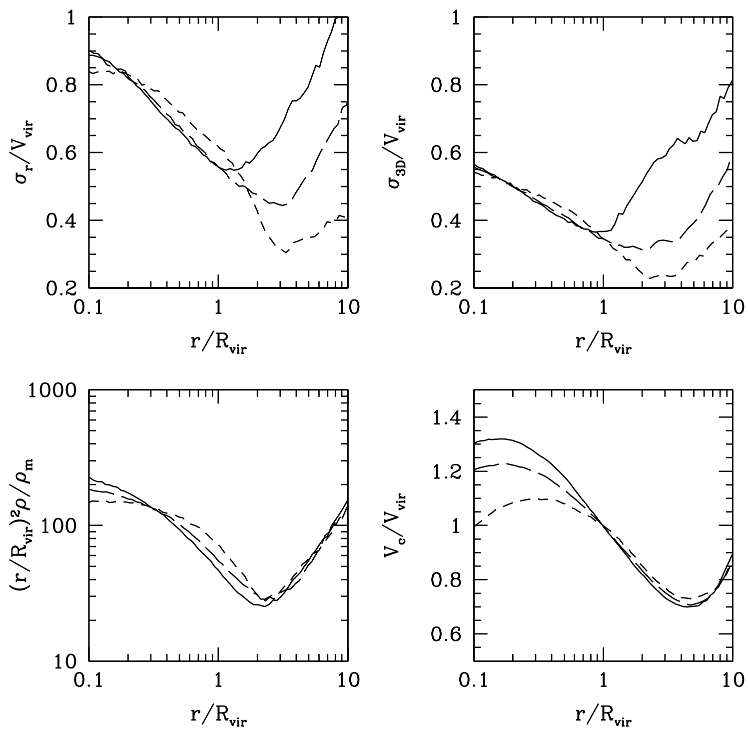

Figure 2.8 Profiles for halos with different mass from Cuesta et al. (2007). The profiles were obtained by averaging over hundreds of distinct halos on each mass bin. Top left panel: radial velocity dispersion. Top right: 3D velocity dispersion. Bottom left: density profile. Bottom right: Circular velocity profile. Full curves are for dwarf with mass $\sim 10^{10}h^{-1}\mathrm{M}_{\odot}$; long dash curves are for Milky Way-type halos with $\sim 10^{12}h^{-1}\mathrm{M}_{\odot}$. Short dash curves are for cluster-size halos with $\sim 10^{14}h^{-1}\mathrm{M}_{\odot}$.

(may not be relaxed) and stationary systems obey the virial theorem. The notion of the static radius should be important for dynamics of environment of isolated halo. For example, motion of satellites at $2-3$ formal virial radii reflects the mass distribution of the central object. For other tests, such as abundance of clusters of galaxies at different redshifts, the distinction between true and convention virial radii does not seem to be an issue. There is only one condition: We need to follow the same definition in the theory and in observations.

There is another interesting result which follows from the analysis of outer regions of halos. It appears that halos of small mass (such as our Milky Way) may not have changed much in their density distribution since $z = 1 - 2$. Figure 2.10 shows the density profile of the halos in proper (physical) units. Within 400 kpc the density of the halos was nearly the same at $z = 1$ as it is now.

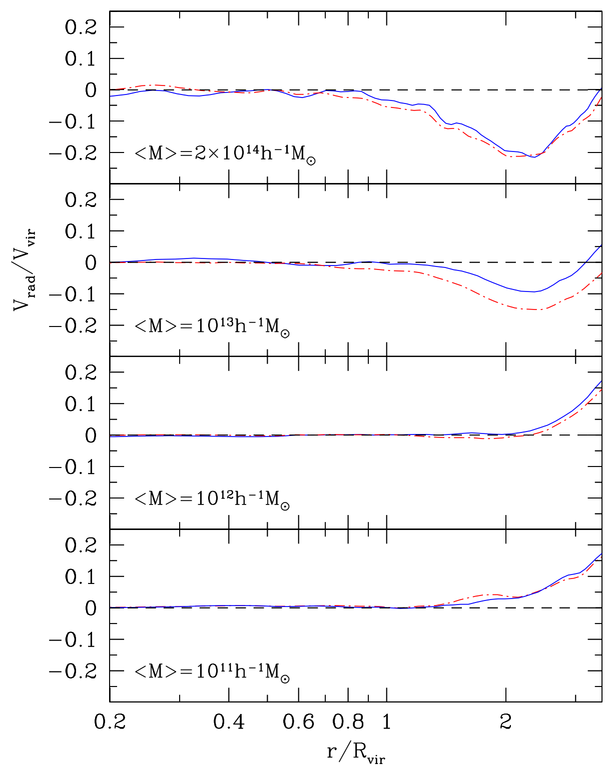

Figure 2.9 Average radial velocities for halos with different virial masses from Cuesta et al. (2007). The full curves show results for isolated halos and the dot-dashed curves are for distinct halos. The velocities are practically zero within $(2-3)R_{\rm vir}$ for halos with mass smaller than $10^{12}h^{-1}\mathrm{M}_{\odot}$. The situation is different for group- and cluster- sized halos (two top panels). For these large halos there are large in- fall velocities, which amplitude increases with halo mass.

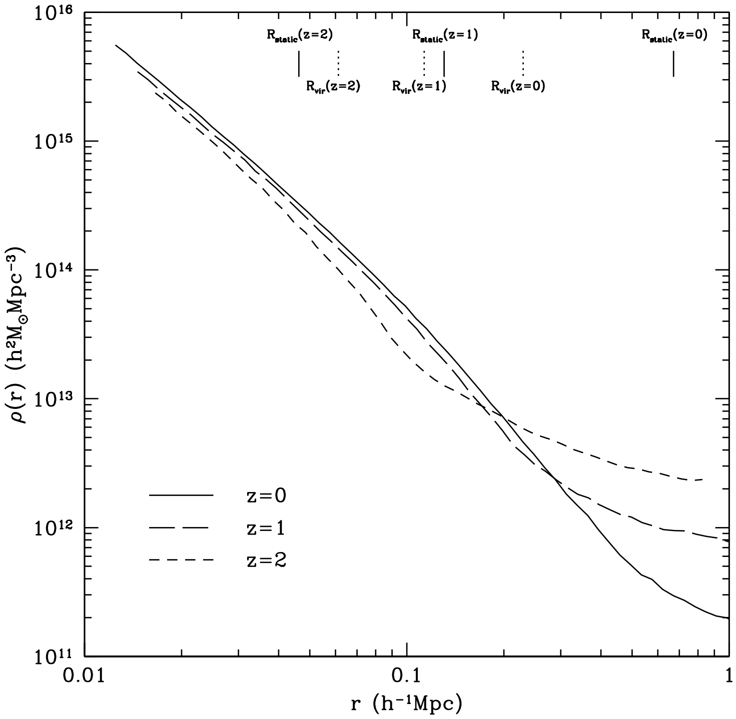

Figure 2.10 Evolution of dark matter density profile from Cuesta et al. (2007). The evolution of the density profile from $z = 2$ to $z = 0$ for galactic-size halos. There has been very little change in this profile from $z = 1$ up to the present epoch. The vertical dotted lines marks the virial radii at $z = 2$ (left), $z = 1$ (middle) and $z = 0$ (right). Static radii are shown with vertical solid lines. The growth of the static radius in Milky-Way size halos from $z = 1$ to $z = 0$ is not due to accretion but virialization of the surrounding regions of the halo.

3 GALAXY FORMATION

The classical picture of galaxy formation was outlined several decades ago. Early analytical models showed the importance of gas-dynamical dissipative processes in galaxy formation (Rees & Ostriker, 1977; Silk, 1977). The basic idea is that gas falls into dark matter halos and it is shock heated at the virial radius. Then the gas looses its energy through dissipative processes and collapses in self-gravitated objects inside dark matter halos (White & Rees, 1978). The angular momentum is preserved in this collapse. Thus, cold gas settles in a thin disk (Fall & Efstathiou, 1980). Inside the disk, the gas achieves high densities and forms stars. Finally, these stars modify the surrounding gas through different mechanisms of feedback, such as supernova explosions. This energy feedback can affect the formation of the whole galaxy (Dekel & Silk, 1986).

Although the previous picture of galaxy formation may be qualitatively correct at some degree, it depends on several important assumptions and simplifications. As a result, it can only make gross predictions about the physical scales of galaxies and it can miss important physical processes relevant for galaxy formation. Nevertheless, this classical picture shows that radiative cooling, star formation and stellar feedback are key processes in the assembly of baryons in galaxies. However, there is a complex interplay between these processes and large-scale cosmological processes. Galaxy formation is linked to the hierarchical formation of large-scale structures. For example, baryons can flow from cosmological distances to the center of dark matter halos along cold flows, which are not being shock heated at the virial radius (Birnboim & Dekel, 2003; Kereš et al., 2005; Dekel & Birnboim , 2006). Another example is the role of stellar feedback in galaxy formation. Stellar feedback injects energy at parsecs scales but it produces galactic outflows that reach Megaparsecs scales (Ceverino & Klypin, 2007). These outflows are routinely detected in high redshift star-forming galaxies (Law et al., 2007).

In short, the current picture of galaxy formation is more complicated than the classical paradigm. An interconnected set of processes with very different spatial scales drives the galaxy assembly. In order to get more accurate predictions about galaxy formation and evolution, it is necessary to follow the dynamics of the gas and dark matter. This is why N-body + gasdynamical simulations have become a very important method to model galaxy formation in a cosmological context. They are able to simulate the internal gasdynamics of galaxies, as well as the gas accretion from the cosmic web and the assembly of gas in galaxy disks.

3.1 Early Simulations of Galaxy Formation

Early gasdynamical simulations started to appear in the last decade of the 20th century (Lake & Carlberg, 1988; Navarro & Benz, 1991; Katz, 1992; Navarro & White, 1994; Barnes & Hernquist, 1996; Quinn et al., 1996; Haehnelt et al., 1998; Mac Low & Ferrara, 1999; Cen & Ostriker, 1999). These simulations faced two main problems: the overcooling problem and the angular momentum catastrophe. Even now, in 2008, these problems are not completely solved.

The Overcooling Problem

Because the radiative cooling is very efficient in low-mass halos at high redshift, the overcooling problem is an issue in the hierarchical clustering scenario of galaxy formation (White & Rees, 1978; White & Frenk, 1991). If most of the gas inside these galactic halos cools, collapses, and forms stars, almost all baryons inside galactic halos should have been locked into stars well before the assembly of present-day galaxies. However, the fraction of baryons found in galaxies at low redshift is significantly smaller than the universal baryonic fraction (Fukugita & Peebles, 2004). In addition, a large fraction of baryons (about 1/2), which is naively expected to be inside galaxies such as our Milky Way, is not accounted for (Klypin et al., 2002; Conroy et al., 2007) – they are not in stars and not in the observed gas. It is clear that in order to produce realistic models, the theory should include mechanisms that prevent catastrophic cooling of gas and its conversion into stars.

It was quickly realized that stellar feedback can potentially solve the overcooling problem (White & Frenk, 1991; Navarro & Benz, 1991). However, the modeling of stellar feedback and its efficiency in cosmological simulations turned out to be a difficult task. Early attempts to introduce stellar feedback into simulations found the obstacle of strong radiative cooling. Katz (1992) is one of the earliest attempts to include radiative cooling, star formation and stellar feedback in gasdynamical simulations of galaxy formation. With only 4,000 gas particles, the simulation resolved the formation of a galaxy with 3 components: a stellar spheroid, a disk and a dark matter halo. However, one of the main results was that most of the energy deposited by supernova explosions was radiated away without any effect in the evolution of the simulated galaxy. Therefore, the overcooling problem was still an issue.

The Angular Momentum Catastrophe

Early cosmological simulations of galaxy formation reported a catastrophic loss of angular momentum during the galaxy assembly, resulting in too small and concentrated galactic disks and very massive spheroids (Navarro & Benz, 1991; Navarro & White, 1994; Navarro et al., 1995; Navarro & Steinmetz, 1997, 2000; SommerLarsen et al., 1999).

Figure 3.1 shows an example from Navarro & Steinmetz (2000). At a given galaxy rotational velocity, the specific angular momentum of observed disks exceeded that of numerical models by more than an order of magnitude. These

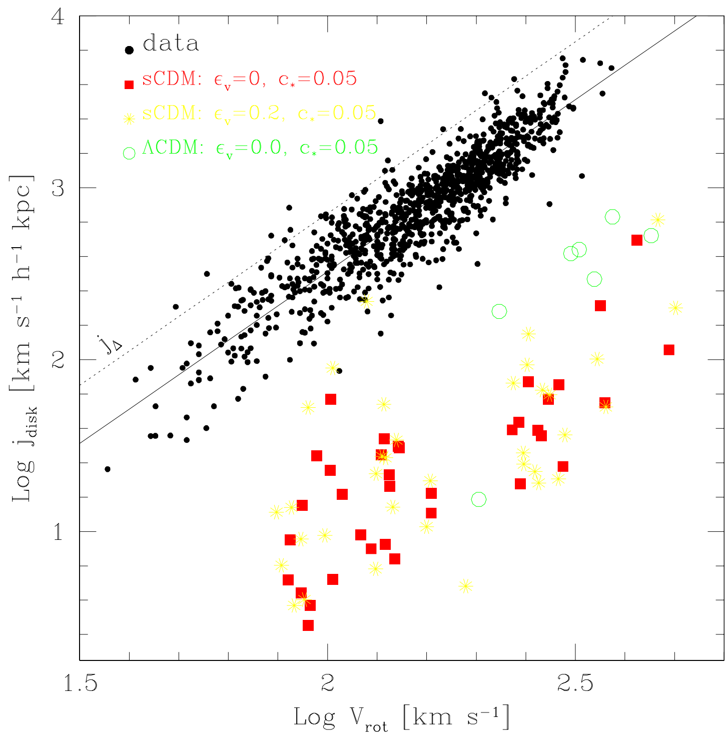

Figure 3.1 Specific angular momentum versus circular velocity of simulated and observed galaxies (Navarro & Steinmetz, 2000). The models have an order of magnitude less specific angular momentum than observations. This is an example of the angular momentum catastrophe in early numerical models of galaxy formation

models failed to reproduce the zero-point of the Tully-Fisher relation, although its slope and scatter were well reproduced.

This angular momentum catastrophe has a double origin. A part of the problem is related to the overcooling problem. Clumps of too cold and dense gas lose all angular momentum due to dynamical friction during the early infall or during mergers at high redshifts (Navarro & Benz, 1991). As a result, most of the angular momentum is transferred from disk material to the halo at high redshift. A second origin is related to the resolution of these early simulations. Numerical artifacts can cause a numerical loss of angular momentum if the simulations has too low resolution to accurately solve for the gasdynamical equations at galactic scales. This is specially a problem for SPH (smoothed particle hydrodynamics) simulations, the most commonly used method for galaxy formation simulations (Mayer et al., 2008).

One example of a numerical model which suffered from this angular momentum problem was provided in Abadi et al. (2003). They performed simulations of galaxy formation with a mass resolution of $1.8 \times 10^7 \mathrm{M}_\odot$ for dark matter particles and a force resolution of 0.5 Kpc. This was consider "high resolution" at that time. They were able to study the properties of the galactic disks formed in the simulations. Figure 3.2 shows the predicted circular and rotational velocity profiles for a MW-type galaxy. It clearly shows that the model failed to reproduce a flat rotation curve typical of massive disk galaxies. The stellar spheroid component is very concentrated. A lot of angular momentum was lost into this slow-rotating component. As a result, the stellar disk did not contribute much to the total mass of the galaxy. They concluded that a better modeling of feedback was required to inhibit the early collapse and cooling of gas at high redshifts.

3.2 Models of Stellar feedback

Simulations of galaxy formation lack the necessary resolution to follow correctly the effect of supernova explosions and stellar winds in the ISM (Thacker & Couchman, 2000). Because of this lack of resolution, the modeling of stellar feedback has relied on ad-hoc assumptions about complex gasdynamical processes at scales unresolved by these simulations (0.2-1 Kpc). Currently, there are three main "recipes" for stellar feedback.

The most common method is to artificially stop cooling when the stellar energy is deposited (Gerritsen & Icke, 1997; Thacker & Couchman, 2000; Sommer-Larsen et al., 2003; Kereš et al., 2005; Governato et al., 2007). This approach prolongs the adiabatic phase of supernova explosion (the Sedov solution) to about 30 Myr. The motivation behind this ad-hoc assumption is that the combination of blastwaves from different supernova explosions and turbulent motions produces hot bubbles

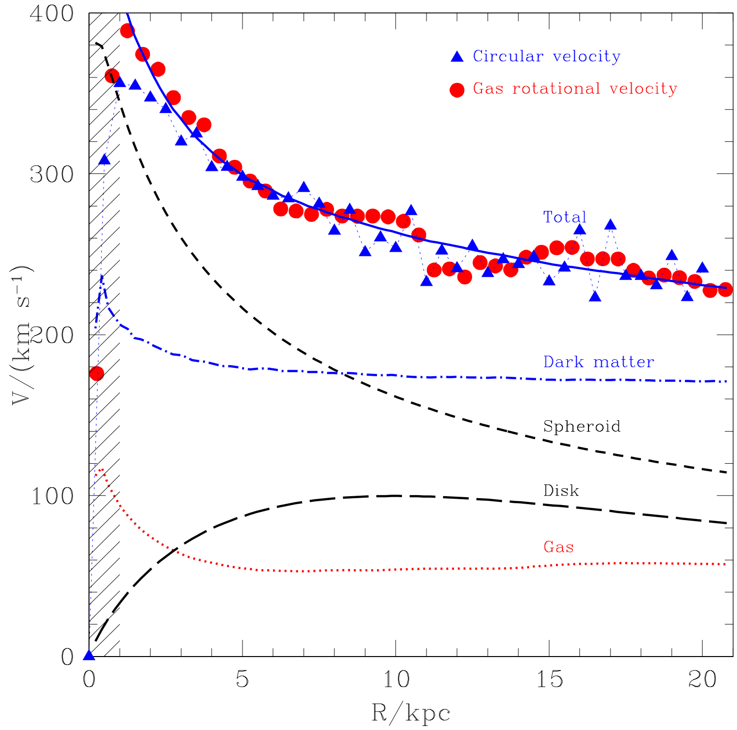

Figure 3.2 Circular velocity and rotational velocity of the gas in a MW-model at $z = 0$ from Abadi et al. (2003). Different curves correspond to the contribution of different galaxy components to the circular velocity. The velocity profiles are very steep, because the spheroidal component with low angular momentum dominates over the rotating disk

much larger than individual supernova remnants and last longer. All these effects are not resolved with the current resolution. These processes do not develop in a self-consistent way. Thus, the delay in the cooling is introduced by hand. The problem is that other effects can be missed at the same time due to a lack of resolution and an inaccurate modeling of feedback.

Another method is to introduce a sub-resolution model in which the energy from supernova explosions is stored in an unresolved hot phase, which does not cool and loses energy through the evaporation of cold clouds (Yepes et al., 1997; Springel & Hernquist, 2003; Oppenheimer & Davé, 2006). In this model, the only effect of stellar feedback is to regulate the star formation: the hot gas is coupled with the cold phase through cloud formation and evaporation. As a result, this high entropy gas is artificially trapped within the galactic disk. Thus, galactic winds are introduced in a phenomenological way in order to reproduce other natural effects of stellar feedback, such as galactic outflows. In this model, each parcel of gas has a probability to rise from the disk according to its star formation rate. In one of these events, the material is given a "kick" in a given direction and the gasdynamical forces are temporally removed to allow the gas to escape from the disk. This produces a galactic outflow which is crucial in this model for matching the star formation rate density observed at high redshifts.

An alternative approach assumes kinetic feedback instead of thermal feedback (Navarro & White, 1993; Abadi et al., 2003). In that case, the energy from supernova explosions or stellar winds is transferred to the kinetic energy of the surrounding medium. This energy is not dissipated directly by radiative cooling. However, in order to resolve this effect accurately, simulations should be able to resolve the expansion of individual supernova explosions or the stellar winds from individual stars. Currently, this is not possible. At larger scales, the picture is more complicated. Different blastwaves from different supernova explosions can collide, dissipating their kinetic energy. The same dissipation of energy happens in collisions of stellar winds in stellar clusters. So, it is commonly assumed that most of the kinetic energy from stellar feedback is dissipated into thermal energy at the smallest scales resolved by simulations. Nevertheless, this feedback-heated gas can expand. As a result, thermal energy can be transferred to kinetic energy. The net results are flows at large scales powered by the thermal feedback. However, feedback heating should dominate over radiative cooling: only in this case are those flows produced.

To summarize, the main problems of current simulations of galaxy formation are the lack of the necessary resolution and too simplified models of the complex gasdynamical processes in the multiphase ISM.

3.3 Current Models of Galaxy Formation

Recent improvements in the resolution of the simulations and in the modeling of the feedback have produced galaxies with more extended galactic disks (Sommer-Larsen et al., 2003; Governato et al., 2004; Robertson et al., 2004; Brook et al., 2004; Okamoto et al., 2005; Governato et al., 2007). Figure 3.3 from Governato et al. (2008) shows the effects of the numerical resolution and the stellar feedback in the growth of either an extended disk or a massive spheroid. The galactic disk looks more extended and well defined in the simulation with 4×10^6 particles, a mass resolution of $8 \times 10^5 M_\odot$ and a force resolution of 0.3 Kpc. (top-right panel). Runs with lower resolution show a more massive and extended spheroidal component. At the same time, the bottom panels show the effect of different models of stellar feedback in runs with the same resolution. The standard thermal feedback model from Katz (1992) produces a more massive spheroid than the "blastwave feedback" model in which radiative cooling is prevented where the energy from supernovae is deposited.

High-resolution models also produce more realistic rotation curves. Figure 3.4 shows the circular velocity profiles, $V_c = (M/r)^{-1/2}$, where M is the total mass in stars, gas and dark matter inside a radius r, for models with a different resolution and implementation of stellar feedback. The high-resolution case produces a less pronounced peak and a more extended stellar distribution. As a result, higher resolution models are less centrally concentrated. The angular momentum problem now is not as severe as it was before. However, it is still an issue.

These state-of-the-art cosmological gasdynamical simulations still have not converged to resolution-independent results. A part of the problem is still related with the artificial loss of angular momentum in SPH simulations (Kaufmann et al., 2007; Naab et al., 2007). For example, Kaufmann et al. (2007) has tested an SPH code in models of galaxy formation within isolated dark matter halos. They are not cosmological models. Instead, they follow the formation of a galactic disk starting from a spherical gas distribution within a preexisting dark matter halo. Due to radiative processes the gas dissipates its energy and settles into a cold disk. Neither star formation nor stellar feedback are included. Nevertheless, these very simplified modes are good test grounds to check for numerical defects, particularly artificial loss of angular momentum. Figure 3.5 shows an example of three face-on views of galactic disks with different resolutions Kaufmann et al. (2007). It is clear that the high-resolution case (HR) with 5×10^5 gas particles, a mass resolution of 2×10^5 $M_\odot$ and a force resolution of 0.5 kpc, forms a larger disk (leftmost panel).

However, the convergence in the final angular momentum of the disk is not reached even with more than 10^5 gas particles (Figure 3.6). Their HR case has $\sim 13\%$ more specific angular momentum than the IR case. The situation in the central disk is worse: the material which ends up within 1 Kpc from the center

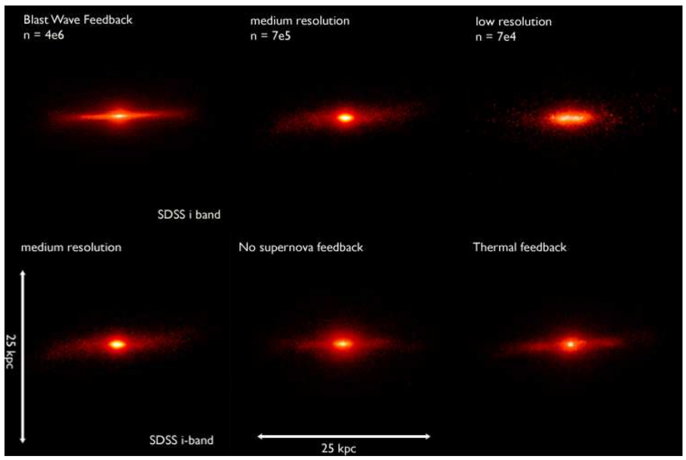

Figure 3.3 Edge-on views of a MW model in the I-band for different models of feedback and different numerical resolutions from Governato et al. (2007). Top panels show simulations with the "blastwave feedback" model and high, medium and low resolutions. Bottom panels show the medium resolution with blastwave feedback, no feedback and normal thermal feedback. The models with feedback and high resolution form galaxies with less concentrated spheroids and more extended disks.

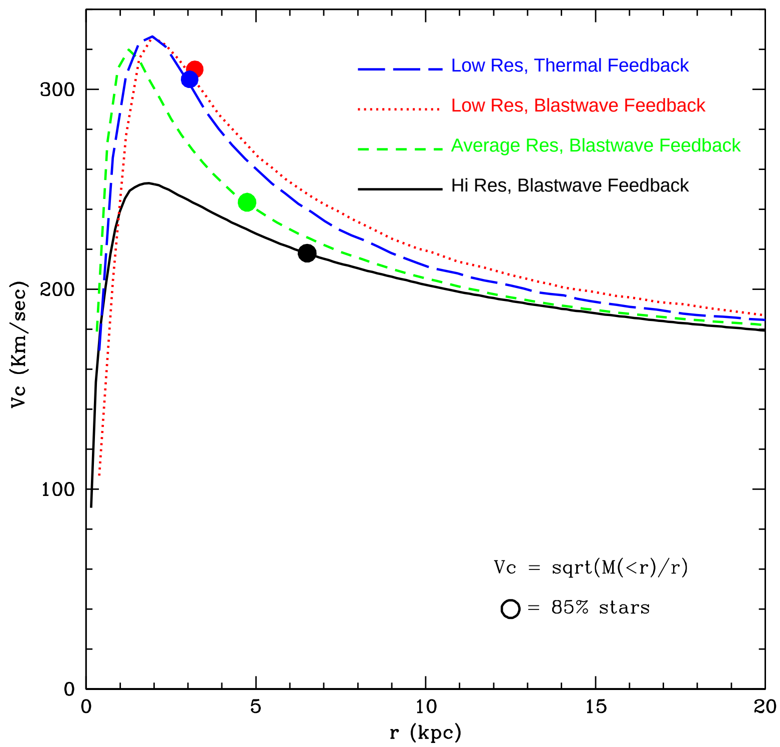

Figure 3.4 The circular velocity profile, $V_c = (M/r)^{-1/2}$, where M is the total mass in stars, gas and dark matter inside a radius r from Governato et al. (2008). Each large dot marks the radius that contains 85% of the stars in each model of the same MW-type galaxy. The low-resolution cases produce a very steep curve which is less pronounced in the high-resolution case. At the same time, the stellar distribution is also more extended.

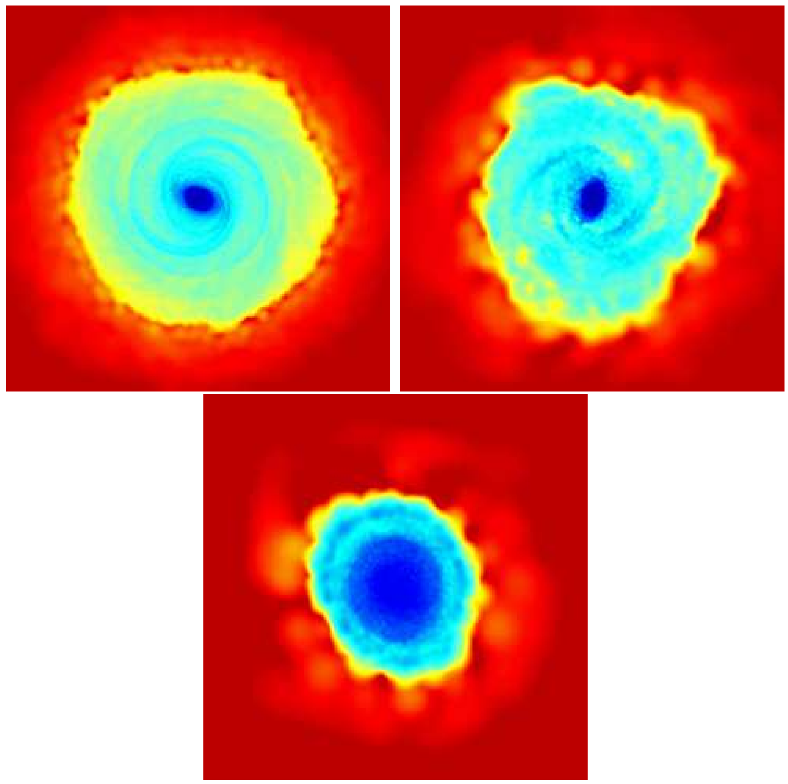

Figure 3.5 Gas density distribution of a galactic disk formed in a isolated MW-size halo after 5 Gyr from Kaufmann et al. (2007). Different panels show different resolution runs. The upper-left panel is high-resolution (HR) run with 5×10^5 gas particles. The upper-right panel has an intermediate resolution (IR) of 9×10^4 gas particles. Finally the bottom panel shows the low resolution case (LR) with 3×10^4 particles. It is clear that the disk is larger and better defined in the high resolution case.

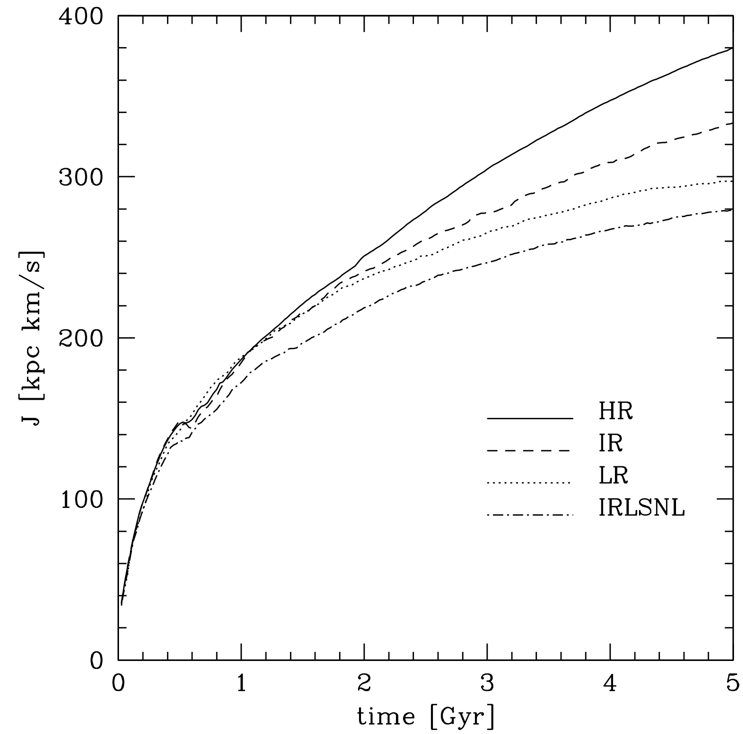

Figure 3.6 Evolution of the specific angular momentum in the disk as a function of resolution from Kaufmann et al. (2007). The HR case has $\sim 13\%$ more specific angular momentum than the IR case.

after 5 Gyr have lost $\sim 80\%$ of their original angular momentum. A significant fraction of this loss is due to numerical artifacts of the SPH implementation. A more detailed discussion of these issues can be found in a recent review paper by Mayer et al. (2008).

3.4 The Merger-driven Scenario for Galactic Disk Formation

Improvements in the resolution of simulations and in the modeling of stellar feedback have produced a new scenario in which galactic disks are more robust that it was previously thought. In the traditional picture for the evolution of galaxy morphology, the merger of two spiral galaxies invariably produces an elliptical galaxy (Toomre & Toomre, 1972). However, new evidence suggests that a merger of two gas-rich galaxies may produce a disk galaxy (Springel & Hernquist, 2005; Robertson et al., 2006).

Springel & Hernquist (2005) showed an extreme example of a coplanar merger of two pure-gas disks. A rotation-supported disk was formed from the leftover gas that was not consumed during the merger. They used a multiphase subgrid model of the ISM. As a result, star-formation regions are "pressurized" by feedback. This delays the gas consumption. However, the mass decomposition showed that the remnant was bulge-dominated: only 30% of the stars were actually in the disk. The galaxy resembled a S0 galaxy, rather than a late-type spiral. Still, it is remarkable how an extended disk can form after a violent merger without late gas accretion.

Robertson et al. (2006) and Cox et al. (2006) extended the study of galaxy mergers, considering other, less extreme, examples. Robertson et al. (2006) concluded that only if more than half of the mass of the progenitors is gas at the moment of the merger, the remnant exhibits a large disk. Otherwise, the remnant resembles a disky elliptical galaxy (Cox et al., 2006). Figure 3.7 shows an example of a merger of two gas-rich disks that produces a remnant disk from Robertson et al. (2006). The progenitors disks are already distorted by tidal interactions after the first passage (T=0.35 Gyr). After the merger (T=0.75 Gyr), the remaining gas settles into a rotation-supported disk and forms and extended stellar disk. As a result, a galactic disk can be formed right after a major merger, without waiting for new material to be accreted.

This merger-driven scenario for disk formation implies that galactic disks started to form at high-redshift, during the epoch of gas-rich mergers. Cosmological simulations support this scenario (Brook et al., 2004; Governato et al., 2007). The initial assembly of present day galactic disks occurred right after their last major merger. Subsequent accretion of gas and star formation contributed to the posterior disk growth until present. This early assembly produced kinematically hot and thick disks (Brook et al., 2004). This may be consistent with the observed thick disk components of nearby galaxies.

To conclude, the galaxy disks are more robust structures than early models had predicted. The factors that determinate the morphology of nearby galaxies: disk or spheroids, are tightly coupled with the details of their merger histories. Galaxies with a late major merger between stellar-dominated objects may generally be elliptical galaxies. These mergers are also called "dry" mergers. In contrast, "wet" mergers between gas-rich galaxies may produce more disky-like galaxies. Due to the fact that wet mergers were more common in the past, the number of disk galaxies should overcomes the number of spheroidal galaxies at high redshifts ($z > 2$), as some cosmological simulations start to indicate (Brook et al., 2004; Governato et al., 2007).

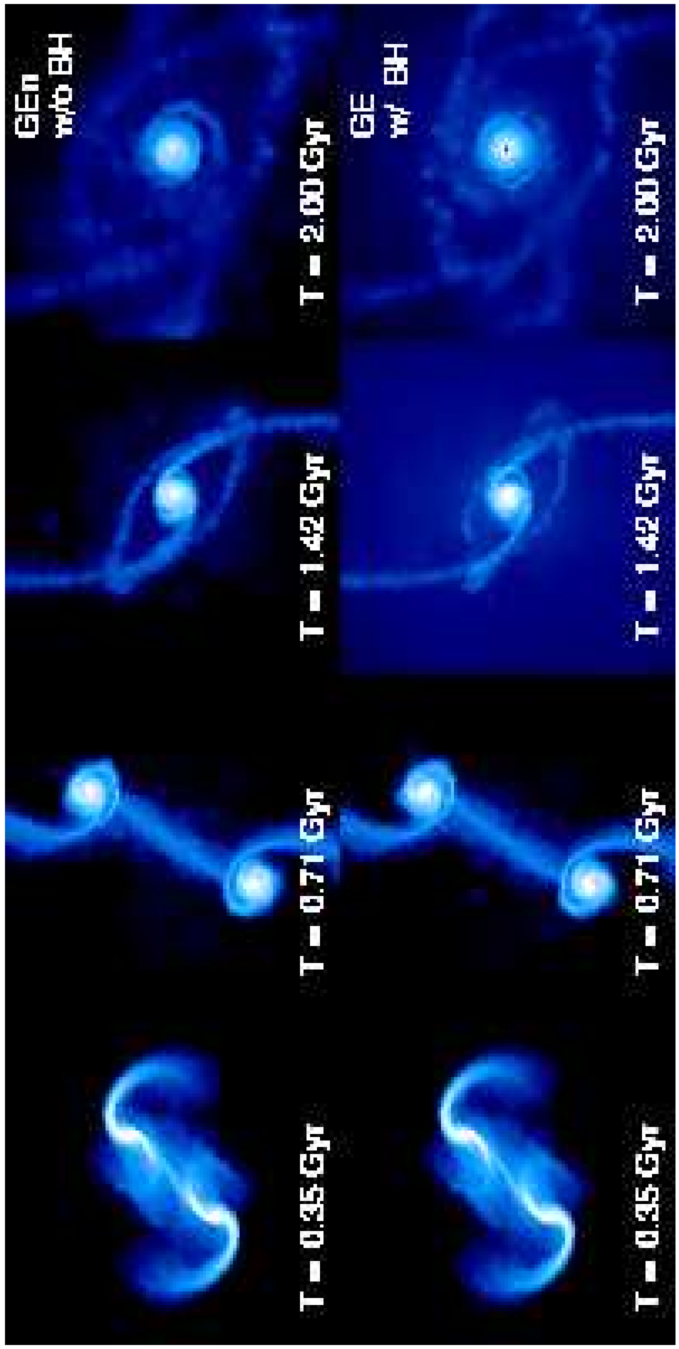

Figure 3.7 Merger of two gas-rich disks that produces a remnant disk from Robertson et al. (2006). The bottom sequence includes the effect of a supermassive black hole feedback. Each panel is 140 Kpc $\times$ 140 Kpc.

4 THE AIM OF THIS PhD

The main purpose of this PhD thesis is to reach a better understanding of galaxy formation within the current cosmological paradigm, the ΛCDM Universe. This cosmological model sets the framework from which a successful theory of galaxy formation should be established. The ΛCDM model predicts a hierarchical clustering scenario for the formation of cosmic structures. In this picture, galaxies form within dark matter halos, which grow through clustering and merging. The statistics and properties of these halos have been extensively studied and have reached an excellent level of accuracy, thanks to N-body models. The mass function is one example. The internal properties of dark matter halos are consistent with the picture of virialized objects, not supported by rotation. However, tidal torques and mergers provide the angular momentum content, which is necessary to produce rotation-supported galaxy disks. Therefore, the physics of the clustering of dark matter is the starting point for modern theories of galaxy formation. Our aim is to extend the ΛCDM paradigm and to include galaxies in our model of the Universe.

Thanks to a better modeling of baryonic physics and a higher resolution, current models of galaxy formation are able to resolve, to some degree, the physics within galaxies. This yields the formation of extended galactic disks. However, they are still too concentrated: state-of-the-art cosmological gasdynamical simulations fail to reproduce rotation curves consistent with observations. The rotation curves from galaxy models rise too fast at the center and tend to have a declining shape, inconsistent with the typical, almost flat, rotation curve of observed disk galaxies. This happens because current models still have too much material with low angular momentum (van den Bosch et al., 2001). They cannot form galaxies with the right distribution of disk and spheroid components: The latter is too massive and concentrated. As a result, the current theory fails to reproduce the right distribution of stars within galaxies. This means that both the overcooling and the angular momentum problems are still not solved.

In summary, the theory of galaxy formation is far from complete. It is not simply a case in which some details of the formation of galaxies are still missing. Current models of galaxy formation use too simplistic models at small scales. Any successful theory of galaxy formation should catch the relevant physics of the interstellar medium (ISM) inside galaxies. It should *resolve* the multiphase nature of the ISM: the cold and dense star-forming gas, the warm and diffuse medium and the hot and dilute gas. The use of simplistic models that do not resolve the thermodynamical conditions of the ISM can lead to erroneous results which lack some important processes for galaxy formation, such as galactic-scale outflows powered by the injection of energy from stars at small scales (Ceverino & Klypin, 2007). These outflows can reach Mpc-scales and enrich the intergalactic medium with the metals produced in the supernova explosions. This is an example of how the physics at small scales has a significant impact on larger scales, from Kpc to Mpc scales. As a result, it is crucial to resolve the thermodynamical state of the star-forming regions. These conditions are determined by a competition between cooling and heating processes. This balance should be resolved in order to account for the right efficiency of stellar feedback (See §5). Otherwise, its effect can be underpredicted (Katz, 1992) or overpredicted (Governato et al., 2007).

This PhD thesis describes our effort in improving the theory of galaxy formation by including more realistic models of radiative cooling (§6.2), star formation (§6.3), stellar feedback (§7) and new effects not considered before, like runaway stars (§7.2). Our approach is to minimize the typical ad hoc assumptions about the complex gasdynamical processes at 10-pc scales. Instead, our simulations *resolve* these processes: the overheating regime (§5), a multiphase ISM (§8) and galactic outflows (§9).

Our model has a metallicity-dependent cooling which takes into account cooling from metal lines as well as molecular cooling. This allows us to model cold ($T \sim 100$ K) gas and to reproduce the physical conditions of the cold star-forming phase of the gas. This is crucial for the efficiency of stellar feedback (§5). This is an important step forward in comparison with other models which only has cooling processes from hydrogen and helium (Governato et al., 2007; Springel & Hernquist, 2003). These models can only cool to $\sim 10^4$ K. This minimum temperature is completely inappropriate for the thermodynamical conditions in star-forming regions, such as molecular clouds.

A model for star formation should have higher efficiency in higher density regions (Krumholz & Tan, 2007). Due to the limited resolution in previous models of galaxy formation, these high density regions within galaxies were not resolved. As a result, the star formation has usually been modeled with low efficiency throughout the galaxy in order to mimic the slow consumption of gas into stars at galactic scales (Governato et al., 2007; Springel & Hernquist, 2003). In our models, we can resolve these high density peaks within galaxies: spiral arms and molecular clouds complexes. As a result, we employ a model of star formation with high efficiency but stars form only in these high density regions. Therefore, we also achieve a slow consumption of gas when averaged throughout a whole galaxy (Tasker & Bryan, 2006). This realistic model of star formation has huge consequences for stellar feedback. The efficiency of stellar feedback in heating the cold star-forming gas is proportional to the star formation rate in the star forming region. A higher star formation rate means a larger number of young and massive stars which inject more energy back to the gas.

However, even at our highest resolution of 30 pc, we still cannot model individual supernova explosions in cosmological simulations. As a result, the modeling of stellar feedback still needs some assumptions. Basically, we assume that all the kinetic energy released by stellar winds and supernova explosions in a small stellar cluster is efficiently thermalized through shocks. As a result, the net effect of stellar feedback is to heat the surrounding medium. This is an conservative approach because it is possible that some fraction of this kinetic energy stays in the gas, in the form of turbulent or expanding motions. In the future, we plan to relax this assumption and include a fraction of kinetic feedback as Navarro & White (1993).

The present work is part of an ongoing effort in the understanding of galaxy formation using cosmological gasdynamical simulations. We start by asking ourselves what are the conditions required for a correct behavior of the interstellar medium within galaxies (§5) and then we build a model for galaxy formation that is able to fulfill these conditions (§6-§7). We have performed simulations of a piece of a galactic disk in order to check our model (§8). It successfully produces the right conditions of the ISM: formation of a multi-phase medium with hot chimneys, super-bubbles, cold molecular phase, and very slow consumption of gas. The critical step has been to check that this picture holds when the resolution is degraded to the resolution that our cosmological simulations can achieve at high redshift. Finally, we have performed cosmological simulations of galaxy formation and studied the effect of stellar feedback in the galaxy growth at high redshifts (§9) and its evolution at lower redshifts (§10).

Once the stellar disk is well formed, a large fraction of the gas in the disk has already been converted into stars. Then, we can assume that the remaining gas does not affect the evolution of the stellar distribution. In this approximation, all gasdynamical processes are neglected and galaxies are treated as pure collisionless systems. In this context, the long-term evolution of galaxies is driven by stellar dynamics. The effects of the gas are secondary. Instead, other purely dynamical effects with time-scales of Gyr start to play a role in the evolution of galaxies. We have used N-body-only models of a stellar disk embedded in a dark matter halo to study this long-term evolution of galaxies. Particularly, the project has been focused on the role of dynamical resonances in stellar disks (§11).

4.1 Project Goals

In summary, this PhD work addresses the following questions:
Can we get extended disks at $z \sim 0$?
What is the physics needed to avoid a too massive spheroid?
Can we solve (or reduce) the overcooling and angular momentum problems?
What is the role of stellar feedback in galaxy formation?

Can our simulations achieve the minimum scale at which stellar feedback is resolved with its full efficiency?

What is the role of dynamical resonances in the long-term evolution of galaxies?

4.2 PhD Thesis Outline

This PhD thesis is organized as follows. Section 5 describes the physics of stellar feedback and the necessary conditions in which stellar feedback dominates over radiative cooling. Section 6 describes the N-body/gasdynamical code used, as well as the details of the implementation of the baryonic physics: radiative cooling and star formation. Section 7 describes all details of the modeling of stellar feedback. Section 8 is devoted to the effect of stellar feedback in the ISM. Section 9 shows the effect of stellar feedback in galaxy formation at high redshift using cosmological simulations of galaxy formation. Section 10 describes galaxy evolution. Finally, Section 11 describes the role of dynamical resonances in the long-term evolution of galaxies.

5 PHYSICAL CONDITIONS FOR THE HEATING REGIME

The contents of this chapter will appear in the paper: *The role of stellar feedback in the formation of galaxies*, Ceverino, D., & Klypin, A. 2007, submitted for publication.

The thermodynamical state of the gas depends on two competing processes: heating from stellar feedback and cooling from radiative processes. They appear as source and sink terms of internal energy in the equation of the first law of thermodynamics:

$$\frac{du}{dt} + p\nabla \cdot \mathbf{v} = \Gamma - \Lambda \tag{5.1}$$

where u is the internal energy per unit volume, p is the pressure of the gas, and $\mathbf{v}$ is its velocity. Parameter Γ is the heating rate due to stellar feedback, and Λ is the net cooling rate from radiative processes.

The heating rate from stellar feedback can be expressed as the rate of energy losses from a young and active single stellar population with a given density, $\rho_{*,\mathrm{young}}$:

$$\Gamma = \rho_{*,\mathrm{young}}\Gamma' \tag{5.2}$$

where Γ' is the specific rate of energy losses of the stellar population according to its age. The cooling rate can be expressed as:

$$\Lambda = n_H^2\Lambda', \tag{5.3}$$

where n_H is the hydrogen number density.

5.1 Heating versus Radiative Cooling

Now, we can ask ourselves under which conditions the feedback heating dominates over the radiative loses. Using the expression, $n_H = \rho_{\mathrm{gas}}/(\mu_H m_H)$, where ρ_{gas} is the gas density, μ_H is the molecular weight per hydrogen atom and m_H is the hydrogen mass, the condition for heating ($\Lambda \leq \Gamma$) can be expressed as:

$$n_H\Lambda' \leq \frac{\rho_{*,\mathrm{young}}}{\rho_{\mathrm{gas}}}\mu_H m_H \Gamma' \tag{5.4}$$

Using typical values, we can rewrite the condition for the heating regime in the following way:

$$\left(\frac{n_H}{0.1\,\mathrm{cm}^{-3}}\right)\left(\frac{\Lambda'}{10^{-22}\,\mathrm{erg\,s^{-1}\,cm^{-3}}}\right) \leq \left(\frac{\rho_{*,\mathrm{young}}}{\rho_{\mathrm{gas}}}\right)\left(\frac{\Gamma'}{10^{34}\,\mathrm{erg\,s^{-1}\,M_{\odot}^{-1}}}\right) \tag{5.5}$$

The cooling rate, Λ', is a strong function of gas temperature. So, the temperature and the density of the gas are two key properties in establishing the cooling or the heating regimes. The following two examples illustrate common situations.

At temperatures around 10^4 K, the cooling rate is close to its maximum value. We use $\Lambda' = 10^{-22}$ erg s^{-1} cm^3 as a fiducial value. In this case eq.(5.5) shows that the heating overcomes the cooling only at very low densities $n_H \leq 0.1$ cm^{-3}, optimistically assuming that the ratio of densities, $\rho_{*,\rm young}/\rho_{\rm gas}$ is about unity. As a result, stellar feedback is not able to heat the gas beyond 10^4 K for densities higher than 0.1 cm^{-3} and typical values of Γ'. This is the well known overcooling problem for simulations, which allow cooling only up to a temperature of 10^4 K at which the star formation is assumed to happen. The energy from stellar feedback is radiated away very efficiently and the thermal feedback cannot play any role. In this case one needs to invoke "subgrid physics" – a guess how the system should react to the energy released by the stars.

The situation is completely different if the gas is allowed to cool to 100 K. The cooling is very inefficient at that temperature: $\Lambda' = 10^{-25}$ erg s^{-1} cm^3. So, stellar feedback can produce the net gas heating even if the density is large: $n_H \approx 100$ cm^{-3} for $\rho_{*,\rm young} \approx \rho_{\rm gas}$. Our conclusion is that simulations should include cooling process below 10^4 K. The cold phase should be resolved in order to get a high efficiency of stellar feedback.

However, heating to high temperatures is still problematic because as the gas is heated, the cooling rate increases. So, the peak of the cooling rate at 10^4 K is a bottle-neck for heating gas to higher temperatures. Nevertheless, temperatures of diffuse gas as high as $10^6 - 10^7$ K have been observed around star-forming regions such as the Rosette nebulae (Townsley et al., 2003; Wang et al., 2007), M17 (Townsley et al., 2003), and the Orion nebula (Feigelson et al., 2005; Guedel et al., 2007). The main question is how young and massive stars can heat their surrounding medium to these high temperatures, if the original medium, in which they were born had high densities.

The answer likely depends on the distance from those young stellar clusters. At small 1-2 pc distances it is likely to have the collisions of stellar winds (Townsley et al., 2003; Feigelson et al., 2005). At larger distances the heating is related to the formation of superbubbles: the cumulative effect of winds and shocks generated by many young stars. One way or another, the density of gas around the young stellar population decreases and the ratio $\rho_{*,\rm young}/\rho_{\rm gas}$ increases as the over-pressured bubble of gas expands. Once the density goes below 0.1 cm^{-3}, eq.(5.5) can be fulfilled even at 10^4 K. The net result is a heating regime, in which the surrounding gas can be heated to very high temperatures. In other words, the process starts with expanding bubbles at low temperatures and then proceeds to a runaway-overheating regime.

As an example, we consider a typical GMC with a mass of 10^5 M$_\odot$ and a size of 50 pc. These are the typical values found in recent catalogs of GMCs in M33 (Rosolowsky et al., 2007), M31 and the Milky way (Sheth et al., 2008). Therefore, the mean density is $n_H = 50$ cm^{-3}. This value seems low compared with typical observed densities of molecular clouds. However, GMCs are highly clumpy. High-density clumps are usually embedded in a low density inter-clump medium. As a result, the volume-averaged density inside clouds is much smaller than the typical observed mass-weighted density (McKee, 1999).

Now, we consider an Orion-like stellar cluster formed at the center of the cloud. The mass of the stellar cluster is $5 \times 10^3\,M_\odot$ (Hillenbrand & Hartmann, 1998). In a region of mass $10^4\,M_\odot$, the stellar cluster has the ratio $\rho_{*,\rm young}/\rho_{\rm gas}$ equal to 0.5, and the condition for heating, eq.(5.5), is fulfilled. This heating produces an over-pressured hot bubble with a pressure 100 times higher than the surrounding unperturbed medium. As a result, the bubble expands, the density decreases, and the ratio $\rho_{*,\rm young}/\rho_{\rm gas}$ increases. Then we get a runaway bubble, which proceeds to blow away all gas (Kroupa et al., 2001).

Simulations should resolve the expansion of bubbles over-pressured by stellar feedback. The density of young (and active) stars and the density of gas should be comparable at the smallest scales resolved by the simulations. The minimum value of the ratio $\rho_{*,\rm young}/\rho_{\rm gas}$ depends on the gas density (eq. 5.5). For moderate gas densities, $n_H = 10 - 100$ cm^{-3}, the above ratio should be around 0.1-1.

The above condition can be achieved if the star formation efficiency, the fraction of the progenitor cloud consumed in stars is 10%-50% at the resolution scale. This high efficiency is consistent with the observed value of 10%-40% found in Galactic stellar clusters, (Greene & Young, 1992; Elmegreen et al., 2000; Kroupa et al., 2001). Due to the fact that 80% of the Galactic star formation occurs in stellar clusters (Lada & Lada, 2003), this high efficiency of star formation should be considered in any star formation model which can resolve the sites where star formation occurs.

5.2 Local Gravity versus Pressure Gradient

As we saw in the previous section, low densities are required in order to heat the gas beyond the peak of the cooling curve. Stellar feedback should evacuate the gas by creating an expanding bubble around young stellar clusters. However, the over-pressured bubble expands only if the pressure gradient overcomes self-gravity.

If we consider an over-pressured bubble of radius R in a homogeneous medium of density ρ, we can derive a Jeans-instability type of condition. As a result, the bubble expands only if the difference in pressure with its surroundings, ΔP, satisfies the following relationship:

$$\Delta P/k \geq \frac{4\pi}{3k} G(\rho R)^2 = 10^{-1}(n_H R_{pc})^2 \tag{5.6}$$

where k is the Boltzmann constant, G is the gravitational constant, and $R_{\rm pc}$ is the radius in pc. The above equation sets the conditions for the bubble expansion. For the Galactic plane the pressure is $P/k \sim 2 \times 10^4$ cm^{-3}K (Cox, 2005). For example, a region of 50 pc in radius and a density of 100 cm^{-3} will only expand if the difference in pressure is bigger than 2×10^6 cm^{-3} K. This can be achieved if the bubble is over-pressured by more than 100 times. Stellar feedback can produce this overpressure just by raising the temperature from 100 K to 10^4 K. The resulting over-pressured region will expand, and the density as well as the cooling rate will decrease. So, the efficiency of stellar feedback increases, raising the temperature and pressure further.

Eq. 5.6 also sets an upper limit on the resolution. Using the equation of state of the ideal gas $P = nkT$, where n is the mean number density and T is the temperature of the gas, the over-pressured bubble should be resolved with a spatial resolution $X_{pc} = R_{pc}/2$, such that the expansion is resolved:

$$\left(\frac{X_{pc}}{75\,\rm pc}\right)^2 \leq \left(\frac{T}{10^4\,\rm K}\right)\left(\frac{n_H}{10\,\rm cm^{-3}}\right)^{-1} \tag{5.7}$$

As a result, for typical values of these over-pressured regions, the resolution should be better than $\sim$ 70 pc. Otherwise, the bubble cannot overcome its self-gravity and cannot expand.

6 THE GASDYNAMICAL MODEL (I): Basic Equations and Physics

The numerical simulations were performed using the Eulerian gasdynamics + N-body Adaptive Refinement Tree (ART) code (Kravtsov et al, 1997; Kravtsov, 1999). This code basically solves the equations of gasdynamics of an ideal fluid plus the equations of motion for particles (dark matter and stars) on an adaptive mesh.

In addition to the basic equations of dynamics, several astrophysical processes relevant for galaxy formation are also taken into account (Kravtsov, 2003). These include radiative cooling, star formation and stellar feedback. The first two processes are described in detail in the following subsections. The modeling of stellar feedback requires a separate section (§7), because of its complexity and relevance for galaxy formation.

6.1 Basic Equations of Gasdynamics and N-body

The fundamental equations of gasdynamics are the continuity, momentum, and energy equations, the Poisson equation and the equation of state of an ideal gas:

$$\begin{aligned}
\frac{\partial \rho_{\rm gas}}{\partial t} + \nabla \cdot (\rho_{\rm gas}\mathbf{u}) &= \mathcal{S}_{\rho_{\rm gas}}, &(6.1)\\
\frac{\partial \mathbf{u}}{\partial t} + (\mathbf{u}\cdot\nabla)\mathbf{u} &= -\nabla\Phi - \frac{\nabla P}{\rho_{\rm gas}} + \mathcal{S}_{\mathbf{u}}, &(6.2)\\
\frac{\partial E}{\partial t} + \nabla \cdot [(E+P)\mathbf{u}] &= -\rho_{\rm gas}\mathbf{u}\cdot\nabla\Phi + (\Gamma - {\rm L}) + \mathcal{S}_E, &(6.3)\\
\nabla^2\Phi &= 4\pi G(\rho_{tot} + 3P_{tot}/c^2) - \Lambda, &(6.4)\\
\varepsilon &= \frac{1}{\gamma-1}\frac{P}{\rho_{\rm gas}}, &(6.5)
\end{aligned}$$

where $\rho_{\rm gas}$ is the gas density, $\mathbf{u}$ is the gas velocity, P is the gas pressure, $E = \rho_{\rm gas}(\varepsilon + \mathbf{u}^2/2)$ is the total gas energy density, and ε is the internal energy of the gas per unit mass.

In the energy equation (eq. 6.3), Γ and L are the heating and cooling rates per unit volume. They take into account radiative processes (§6.2) and thermal feedback (§7.1). In the Poisson equation (eq. 6.4), Φ is the potential, ρ_{tot} is the density of all the components of matter (gas, stars and dark matter), P_{tot} is the total pressure in the universe, and Λ is the cosmological constant. For our simulations, we assume that $P_{\rm tot} \approx 0$. In the equation of state (eq. 6.5), γ is the adiabatic index. In our case, the internal energy is simply the specific kinetic energy of the gas particles. As a result, γ takes the value of an ideal monoatomic gas, $\gamma = 5/3$. Finally, $\mathcal{S}_{\rho_{\rm gas}}$, $\mathcal{S}_{\mathbf{u}}$, and $\mathcal{S}_E$ are source/sink terms in the continuity, moment and energy equations. These terms are coming from the processes of star formation (§6.3) and stellar mass looses (§7.5), which modify the gas density, momentum and energy. They will be described in the following sections.

In addition to the equations of gasdynamics, the code also includes the self-consistent advection of metals produced in stars. These metals are released into the gas by supernova explosions and stellar winds from massive stars (§7.4) and evolved stars (§7.5):

$$\frac{\partial \rho_{Z_{SNII}}}{\partial t} + \nabla \cdot (\rho_{Z_{SNII}} \mathbf{u}) = \tag{6.6}$$

$$\mathcal{S}_{Z_{SNII},\text{feedback}} + \mathcal{S}_{Z_{SNII},\text{Stellar mass looses}} + \mathcal{S}_{Z_{SNII},\text{star formation}}$$

$$\frac{\partial \rho_{Z_{SNIa}}}{\partial t} + \nabla \cdot (\rho_{Z_{SNIa}} \mathbf{u}) = \tag{6.7}$$

$$\mathcal{S}_{Z_{SNIa},\text{feedback}} + \mathcal{S}_{Z_{SNIa},\text{Stellar mass looses}} + \mathcal{S}_{Z_{SNIa},\text{star formation}}$$

where $\rho_{Z_{SNII}}$ and $\rho_{Z_{SNIa}}$ are the mass density of metals ejected in supernova-II and supernova-Ia. The source terms will be described in §6.3, §7.4 and §7.5.

The gasdynamical equations are coupled to the equations of motion of dark matter particles and stellar particles:

$$\frac{d\mathbf{r}}{dt} = \mathbf{v}, \tag{6.8}$$

$$\frac{d\mathbf{v}}{dt} = -\nabla\Phi \tag{6.9}$$

where $\mathbf{r}$ and $\mathbf{v}$ are the particles positions and velocities. Finally, the code also tracks the mass fraction of metals locked into stars, $X_{*,\rm SNII}$ and $X_{*,\rm SNIa}$. Each stellar particle has the metallicity of its parent gas.

The differential equations of gasdynamics (eqs. 6.1-6.3) are integrated using the gasdynamics solver described in (Khokhlov, 1998). It uses a second-order Godunov solver (Godunov, 1959) that evaluates Eulerian fluxes by solving the Riemann problem at every cell interface (Colella & Glaz, 1985). Left and right states for the Riemann problem are obtained by piecewise linear interpolation (van Leer, 1979). Finally, a small amount of artificial diffusion is added to the numerical fluxes in order to avoid extreme discontinuities (Colella & Woodward, 1984).

The global time step of integration is determined by the Courant-Friedrichs-Lewy (CFL) condition:

$$\Delta t_0 \quad = \quad cfl \times \frac{\Delta x_0}{v_{\max}} \tag{6.10}$$

where cfl is a constant smaller than unity, Δx_0 is the size of a 0-Level cell and $v_{\max}$ is the maximum velocity component found in the simulation. In other words, $v_{\max}$ is the maximum value of the field: $c_s + |u_i|$, where c_s is the sound speed and u_i is the bulk velocity in the direction i=x,y,z.

Extensive tests show that this gasdynamics solver can resolve shocks up to the resolution scale. One of the definitive tests is to reproduce the Sedov solution for the propagation of a blastwave produced by a point explosion. More details about the numerical integration and other tests of the gasdynamics solver can be found in Kravtsov (1999).

6.2 Radiative Processes

The interaction between the "ordinary matter" and radiation is one of the main differences with respect to the dark matter. The internal energy of the baryonic gas can change due to these interactions. The gas loses internal energy (cools) mainly due to inelastic collisions between electrons and other particles. At the same time, the gas gains internal energy (heats) mainly through photoionization heating from an external UV field. In this process, the new free electron has an extra kinetic energy that is transferred to the thermal energy of the gas through elastic collisions. Thus, the net radiative cooling rate is just the difference between the cooling and heating rates.

We use the model of net radiative cooling described in Kravtsov (2003). The model includes Compton heating/cooling, metal lines, hydrogen, helium and molecular cooling plus a UV heating due to a cosmological ionizing background (Haardt & Madau, 1996). The cooling and heating rates from radiative processes are tabulated using the CLOUDY code (version 96b4; Ferland et al., 1998).

Cosmological Ionizing Background

The external ionizing field is assumed homogeneous. It is treated as a background produced by quasars, active galaxies and young stars. The spectral shape is assumed to be independent of the origin of the radiation:

$$J_\nu \quad = \quad J_{\nu_0} \left(\frac{\nu}{\nu_0} \right)^{-\alpha} \tag{6.11}$$

where J_{ν_0} is the amplitude of the radiation, ν_0 is the Lyman limit frequency (λ=912 Å) and $\alpha \sim -1.8$

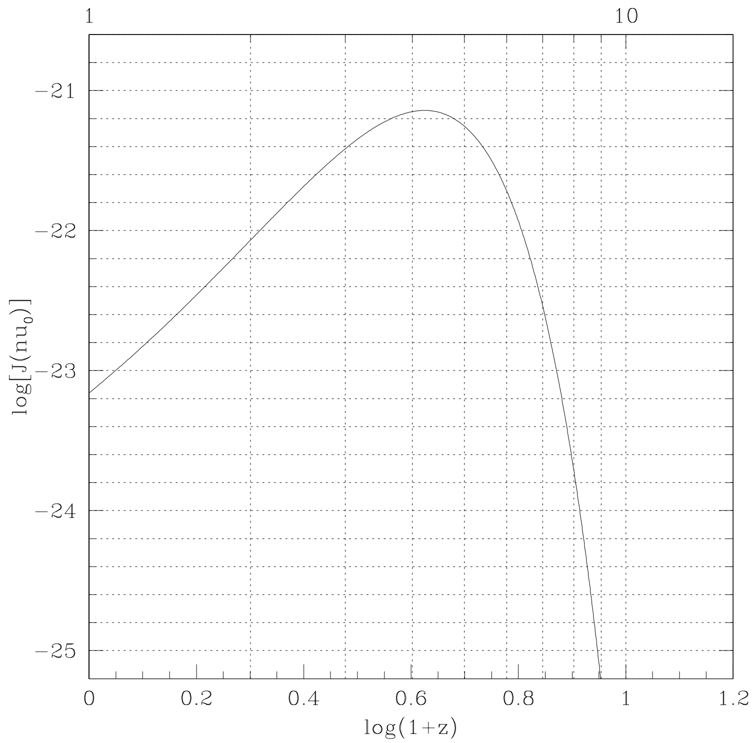

Figure 6.1 Redshift-dependence of the ionizing background amplitude, $J_{\nu_0}(z)$

The amplitude of the radiation depends on the redshift through the model of Haardt & Madau (1996) for a cosmologically averaged UV background:

$$J_{\nu_0}(z) = J_0(1+z)^B \exp\left(-(z-z_c)^2/S\right) \tag{6.12}$$

The parameters, $J_0 = 2.5 \times 10^{-22}$, $B = 0.75$, $z_c = 3.0$, and $S = 2.5$ where chosen to roughly approximate observational constraints (Scott et al., 2002). Figure 6.1 shows $J_{\nu_0}(z)$ for this choice of parameters.

Cooling and Heating Rates: CLOUDY Tables

CLOUDY is a spectral synthesis code that simulates the steady-state conditions within an astrophysical plasma exposed to an external radiation field (Ferland et al., 1998). These conditions are controlled by a large set of microphysical processes. These processes set the ionization fractions of about 30 different elements, the population of the excited levels of all existing ions and the kinetic temperature of the free electrons.

The level of ionization is determined by balancing all ionization and recombination processes. Ionization processes include photoionization, Auger and collisional ionization and charge transfer. Recombination processes include radiative, dielectronic and three-body recombination and charge transfer. The free electrons are assumed to have a predominantly Maxwelian velocity distribution with a kinetic temperature determined by the balance between heating and cooling processes. In summary, the calculation of the cooling and heating rates takes into account more than 10^4 different processes.

A normal setup in CLOUDY consists in an optically thick slab of plasma illuminated from both sides with an ionizing background. The "cloud" is divided into a large number of parallel pieces, so that the plasma conditions smoothly change from one region to the next one. The cooling and heating rates at the center of the slab are tabulated for different conditions of density, temperature and metallicity of the plasma and different strength of the redshift-dependent UV flux. In our case, the slab has a thickness of 1 Kpc, a typical galactic scale. These tables are then used by the gasdynamical code to estimate the cooling and heating rates from radiative processes according to the local conditions of the gas.

However, two caveats remain in these CLOUDY tables. The molecular cooling is based on published cooling curves. It does not include the detailed microphysics implemented for atomic cooling. As a result, the lowest temperature in which radiation equilibrium is possible is around 4×10^3 K (Ferland et al., 1998). The second caveat is that the effect of dust is marginally included.

6.3 A Model of Star Formation for Scales Below 100 pc

A successful model of star formation in simulations should take into account the spatial resolution. For example, in typical cosmological simulations with a resolution of ~ 1 Kpc, the star formation is averaged over a large volume of ISM. These simulations should have a star formation model with low star formation efficiency in order to reproduce the global efficiencies found in nearby galaxies. Observations of quiescent galactic disks show long gas consumption time-scales averaged over a significant piece of a galaxy, $\tau_{\rm global} = \Sigma_{\rm gas}/\Sigma_{\rm SFR} \sim 1$ Gyr , where $\Sigma_{\rm SFR}$ is the star formation rate surface density an $\Sigma_{\rm gas}$ is the gas surface density (Kennicutt, 1998; Kennicutt et al., 2007). At the same time, for starburst galaxies, the global gas consumption time-scale is much shorter, $\tau_{\rm global} = 0.1$ Gyr (Kennicutt, 1998).

However, if the resolution is high enough to resolve the regions where star formation mainly occurs (giant molecular clouds) the star formation efficiency can be much higher: the time-scales for the formation of Galactic stellar clusters are around few Myr and 10% - 40% of the gas is consumed (Greene & Young, 1992; Elmegreen et al., 2000). As a result, simulations which can resolve the sites of star formation should have a high star formation efficiency only in the high-density regions, where molecular clouds can form (Tasker & Bryan, 2006). In practice, the maximum resolution that we can afford is between 30-70 pc. This

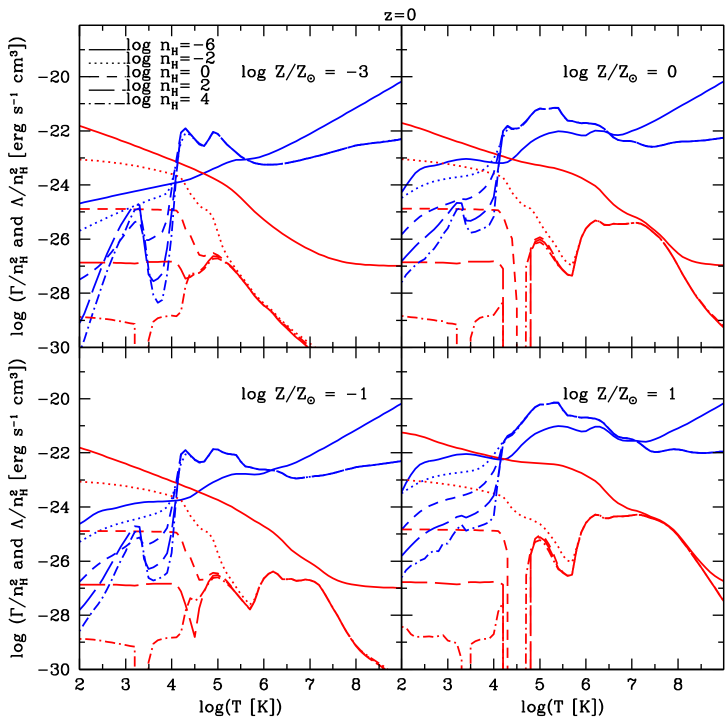

Figure 6.2 Cooling rates (Blue curves) and heating rates (Red curves) from radiative processes using CLOUDY. The rates are tabulated for different conditions of density, temperature and metallicity of the plasma and different strength of the redshift-dependent UV flux The different panels show different metallicities at redshift z=0.

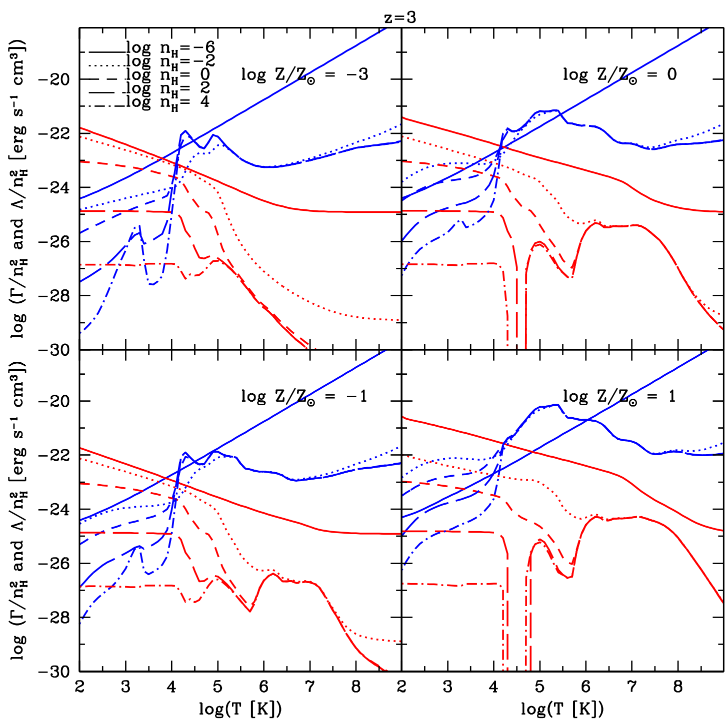

Figure 6.3 Same as figure 6.2 but for redshift z=3

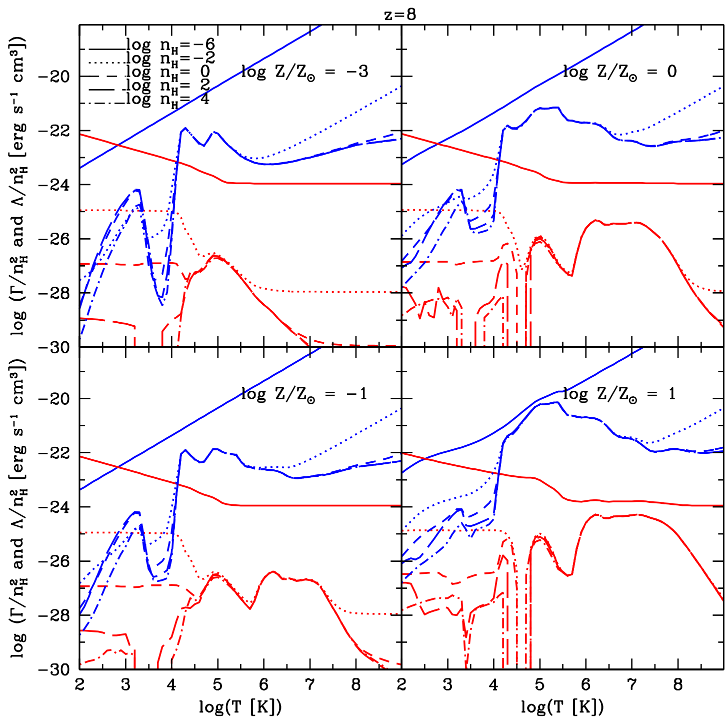

Figure 6.4 Same as figure 6.2 but for redshift z=8

limits the maximum density that our simulations can resolve. For example, if we consider a typical giant molecular cloud of 10^5 $M_\odot$ (Rosolowsky et al., 2007), the mean density averaged over 30-80 pc scales will be 10-200 cm^{-3}. This gives an idea of the typical densities where star formation occurs in our simulations.

In our code, star formation is allowed in a time step, $dt_{\rm SF}$, which is equal to the time step of the 0-Level of resolution. This time step is controlled by the Courant condition for hydrodynamics and in our cosmological simulations, $dt_{\rm SF}$ = 1-2 Myr. During this period of time, a stellar particle can form only where the density and temperature reach a given threshold: $\rho_{\rm gas} > \rho_{\rm SF}$ and $T_{\rm gas} < T_{\rm SF}$. Even in these cold and dense regions, each star formation event is treated as a random event with a probability Pr to occur. We roughly approximate the fact that regions with higher densities have a higher probability to host star formation events by assuming a simplified formula:

$$Pr = \frac{\rho_{\rm gas}}{100\rho_{\rm SF}} \tag{6.13}$$

In this way, the number of stellar particles remains at a value that is not computationally prohibited. In the formation of a single stellar particle, the star formation rate is proportional to the gas density (Kravtsov, 2003):

$$\frac{d\rho_{*,\rm young}}{dt} = \frac{\rho_{\rm gas}}{\tau} \tag{6.14}$$

where $\rho_{*,\rm young}$ is the density of new stars, $\rho_{\rm gas}$ is the gas density and τ is a constant star formation timescale. The density and temperature thresholds used are $\rho_{\rm SF}$ = 0.035 $M_\odot$ pc^{-3} ($n_H = 1$ cm^{-3}) and $T_{\rm SF} = 10^4$ K. In spite of the fact that we allow star formation starting at 10^4 K, in practice the vast majority (> 90%) of "stars" form at temperatures below 1000 K and more than half of the stars form below 300 K and densities larger than 10 cm^{-3}.

As described in §5, the ratio $\rho_{*,\rm young}/\rho_{\rm gas}$ should be $\sim$ 0.1-0.5 for typical conditions of dense, star-forming gas. Only in this case thermal feedback can produce over-pressured hot bubbles in the sites of star formation (eq. 5.5). Based on equation 6.14, this ratio of densities can be expressed as

$$\frac{\rho_{*,\rm young}}{\rho_{\rm gas}} = \frac{dt_{\rm SF}}{\tau} \tag{6.15}$$

As a result, thermal feedback is only efficient in dense, cold, star-forming gas if $dt_{\rm SF}/\tau \sim 0.1 - 0.5$. This sets the value of τ, because $dt_{\rm SF}$ is set by the conditions of hydrodynamics, as explained before: $dt_{\rm SF} = 1 - 2$ Myr. Therefore, the value of τ should be in the range 2-20 Myr, consistent with the gas consumption timescales during the formation of Galactic stellar clusters (Greene & Young, 1992; Elmegreen et al., 2000). However, this high local efficiency of star formation in high-density regions produces the observed low global efficiency, $\tau_{\rm global} = 0.1 - 1$ Gyr, as discussed in §8.5.

Each newborn stellar particle can be treated as a single stellar population with the same age and metallicity. Its internal evolution is controlled by the initial mass function. The code uses the Miller & Scalo (1979) initial mass function with a 0.1-100 $M_\odot$ mass range:

$$\psi(m) = \frac{C_0}{\ln 10} m^{-1} \exp\left[-C_1(\log m - C_2)^2\right] \tag{6.16}$$

where C_1 and C_2 take the commonly used values of $C_1 = 1.09$ and $C_2 = -1.02$. C_0 is just an arbitrary normalization factor.

The IMF controls the total number of core-collapsed supernovae (supernovae-II) and supernovae-Ia that occurs in a single stellar particle. We assume that supernova-II occurs for all stars with masses between 8 and 100 $M_\odot$ and supernova Ia occurs for 3-8 $M_\odot$ stars. Therefore, the integration of the IMF gives 1 supernova-II per 134 $M_\odot$ of stellar mass and 1 supernova-Ia per 90 $M_\odot$. More details about the process of stellar feedback are given in the next section.

The consumption of gas into stars also depletes the gas density, momentum and total energy. As a result, the continuity, momentum and energy equations (eq. 6.1-6.3) have sink terms where star formation occurs:

$$\mathcal{S}_{\rho_{\rm gas},\rm Star\ formation} = -\frac{\rho_{\rm gas}}{\tau} \tag{6.17}$$

$$\mathcal{S}_{\mathbf{u},\rm Star\ formation} = -\frac{\mathbf{u}}{\tau} \tag{6.18}$$

$$\mathcal{S}_{E,\rm Star\ formation} = -\frac{E}{\tau} \tag{6.19}$$

At the same time, the formation of stars depletes the amount of metals in the gas. This results in sink terms in the equations of metal advection (Eq. 6.6-6.7):

$$\mathcal{S}_{Z_{SNII},\rm Star\ formation} = -\frac{\rho Z_{SNII}}{\tau} \tag{6.20}$$

$$\mathcal{S}_{Z_{SNIa},\rm Star\ formation} = -\frac{\rho Z_{SNIa}}{\tau}. \tag{6.21}$$

7 THE GASDYNAMICAL MODEL (II): STELLAR FEEDBACK

We assume a model of thermal feedback for the injection of energy from stellar winds and supernova explosions. The kinetic energy from these processes is efficiently dissipated into thermal energy due to shocks at scales below the spatial resolution.

The net thermal rate, heating rate minus cooling rate, is used to update the internal energy in each step of the simulation. This approach is rather different than the deposition of energy. Instead, the energy injection from stellar feedback is treated in a self-consistent way along with the radiative loss.

7.1 Heating Rate from Stellar Feedback

The heating rate from stellar feedback in a given volume element is modeled as the rate of energy loss from a set of single stellar populations present in that volume:

$$\Gamma = \frac{1}{V}\sum_i M_i \Gamma'(t_i), \tag{7.1}$$

where M_i and t_i are the mass and the age of each single stellar population.

The modeling of the specific release of energy over time, Γ', is motivated by the results from population synthesis codes, such as STARBURST99 (Leitherer et al., 1999). Figure 7.1 shows different models of Γ' and the results of a STARBURST99 computation with a Miller-Scalo IMF from 0.1 $M_\odot$ to 100 $M_\odot$. Γ' is dominated by stellar winds from massive OB main-sequence stars and WR stars during the first few Myr. Later, the energy is produced by core-collapse supernovae from stars more massive than 8 $M_\odot$. After 40 Myr, the release of energy comes from stellar winds of AGB stars and other less powerful sources, and the injection rate drops 6 orders of magnitudes. Supernovae Ia dominate the feedback at much longer time-scales. We assume a peak of the SNIa rate at 1 Gyr. However, this peak is 3 orders of magnitude lower than the contribution from core-collapse supernovae. This is because the energy from a population of SNIa is diluted over a much longer time scale than the energy from core-collapse supernovae.

We model Γ' with a constant rate of 1.18 $\times 10^{34}$ erg $s^{-1} M_\odot^{-1}$ over 40 Myr. This is equivalent to the injection of 2×10^{51} erg of energy from stellar winds and supernova explosions per each massive star with $M > 8$ $M_\odot$ during its lifetime. We assume a Miller-Scalo IMF in the mass range $(0.1 - 100)$ $M_\odot$. Note that this constant heating rate is the sum of the contributions from all massive stars in a single stellar population. We also consider a simpler model, which we call a

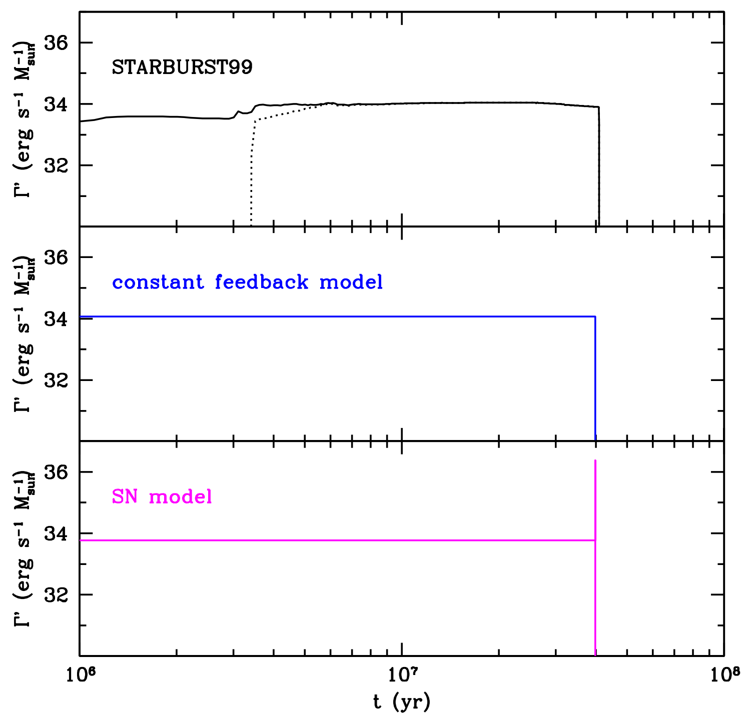

Figure 7.1 Rate of energy losses per unit mass from a single stellar population. The top panel shows the results from the STARBURST99 code, assuming a Miller-Scalo IMF for a mass range $(0.1-100)$ $M_{\odot}$. The dotted line shows the contribution of supernova explosions and the full line shows the total rate. Although supernova explosions dominate the overall energy release, stellar winds are the only mechanism of energy release during the first few Myr. Middle and bottom panels show two different models: a constant feedback model and a model of stellar wind plus core-collapse supernova. Although the total energy released is the same in both models, the SN model is more elementary and takes into account the explosive nature of core-collapse supernova.

SN model. In this case, an energy of 10^{51} erg is injected at constant rate due to stellar winds over 10 or 40 Myr. Then it follows a strong peak of energy release due to the supernova explosion, in which 10^{51} ergs are released during 10^5 yrs – the typical age of young supernova remnants. Although the total energy released is the same in both models, the SN model takes into account the explosive nature of core-collapse supernovae.

7.2 A Model of Runaway Stars

It is crucial to understand where and how the energy from massive stars is released back to the ISM. While a large fraction of massive stars are found in stellar clusters and OB associations, 10-30% are found in the field, away from any molecular cloud or stellar cluster (Gies, 1987; Stone, 1991). This population has peculiar kinematics. Their velocity dispersion is about 30 km s^{-1}, much higher than the velocity dispersion of the population of massive stars in clusters (10 km s^{-1}) (Stone, 1991). Some of these stars have large peculiar velocities, up to 200 km s^{-1} (Hoogerwerf et al., 2000). This is why they are called runaway stars. The current scenario of the origin of runaway stars is the ejection of these massive stars from stellar clusters. There are two possible mechanisms of this ejection. One possibility is the ejection due to a supernova explosion in a close binary system (Zwicky, 1957; Blaauw, 1961). The second mechanism is the ejection due to dynamical encounters in the crowded regions of stellar clusters (Poveda et al., 1967). In spite of the fact that a significant fraction of the stellar feedback occurs far from star forming regions, no previous attention has been paid to its effect on galaxy formation.

The effect of runaway stars is implemented by adding a random velocity to a fraction of stellar particles (10%-30%). This extra velocity has a random orientation and the value is taken from an exponential distribution with a characteristic scale of 17 km s^{-1}. This choice is motivated by Hipparcos data (Hoogerwerf et al., 2000) and Monte-Carlo simulations (Dray et al., 2005). For comparison, a Gaussian distribution is also used (Stone, 1991). However, the effect of runaway stars in the ISM is not very sensitive to the details of this velocity distribution.

7.3 Feedback from Supernovae-Ia

We assume that supernovae Ia occur in evolved stars. As a result, supernovae Ia dominate the injection of energy at much longer time-scales, several thousand Myr after the formation of a single stellar population.

The specific release of energy from SNIas of a single stellar population of age t assumes a given rate of SNIas:

$$\Gamma'_{\rm SNIa}(t) \;=\; E_{\rm SNIa} \times \frac{dN_{\rm SNIa}}{dtdM}(t) \tag{7.2}$$

where, $E_{\rm SNIa} = 10^{51}$ erg is the energy of an individual supernova explosion. This rate is given by the following formula:

$$\frac{dN_{\rm SNIa}}{dtdM}(t) \;=\; \frac{f_{\rm SNIa}}{1.75\ t_{\rm peak}} e^{-x^2}\sqrt{x}, \quad x = \frac{t_{\rm peak}}{t} \tag{7.3}$$

where $f_{\rm SNIa}$ is the total number of SNIas per solar mass, given by the IMF (§6.3) and $t_{\rm peak}$ is the age of the maximum peak in the rate of SNIas. We assume that the peak happens at 1 Gyr. The factor 1.75 is a normalization factor, so that the total amount of SNIa per solar masses is equal to $f_{\rm SNIa}$ for a significant long period of time.

Figure 7.2 shows the shape of $\Gamma'_{\rm SNIa}$. It rises strongly at $t_{\rm peak} = 1$ Gyr and then gradually declines after the peak. However, this peak is 3 orders of magnitude lower than the contribution from core-collapse supernovae. This is because the energy from a population of SNIas is diluted over a much longer time scale than the energy from core-collapse supernovae. In any case, this is the most powerful energy source for an old stellar population, after that all SNIIs have already exploded.

7.4 Metal Release

Another effect of supernova explosions is the enrichment of the ISM with newly-synthesized metals. The metal enrichment from SNII and SNIa is treated separately. This is because, both supernova populations have very different time-scales and release metals with different abundance ratios.

Each stellar particle releases metals due to SNII in a constant rate over a period in which the population remains active in SNII explosions, $t_{SN} = 40$ Myr. The total mass of heavy elements is $F_Z M_*$, where M_* is the mass of the stellar population and F_Z is the metal mass fraction averaged over the IMF, $\psi(m)$, between a lower stellar mass, $m_l = 0.1$ M$_\odot$, and an upper stellar mass, $m_u = 100$ M$_\odot$:

$$F_Z \;=\; \frac{\int_8^{m_u} m\psi(m) f_Z(m)}{\int_{m_l}^{m_u} m\psi(m)} \tag{7.4}$$

where $f_Z(m)$ is the mass fraction in metals from a supernova explosion of a star with mass m :

$$f_Z(m) \;=\; min(0.2, 0.01\ m - 0.06) \tag{7.5}$$

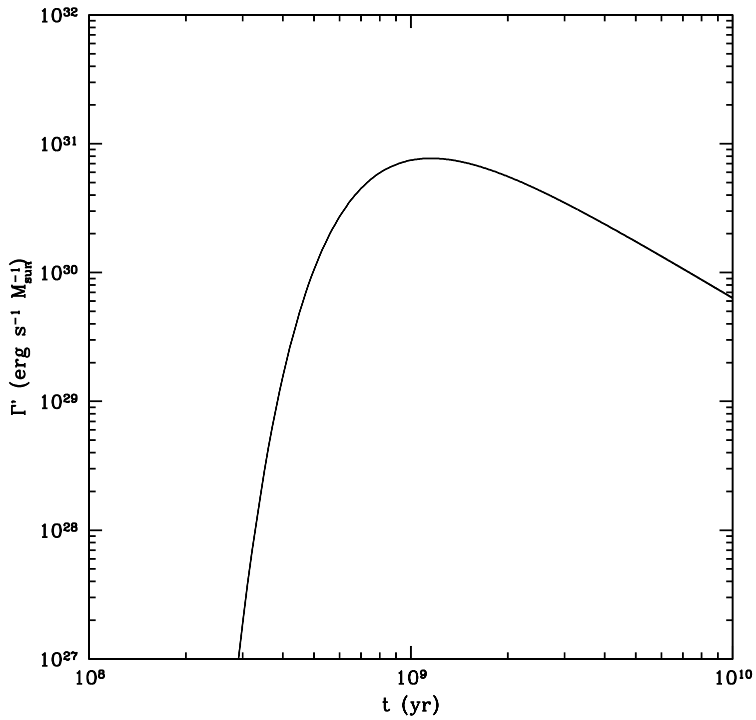

Figure 7.2 Contribution of supernovae-Ia to the rate of energy loss per unit mass of a single stellar population of age t. The maximum contribution happens at $t_{\rm peak} = 1$ Gyr. This peak is 3 orders of magnitude lower than the contribution from core-collapse supernovae. However, SNIa is the most powerful energy source for an old stellar population, after that all SNIIs have already exploded.

This model roughly approximates the results of (Woosley & Weaver, 1995). Finally, the source term for the density of SNII metals from a single stellar population of density ρ_* is just:

$$\mathcal{S}_{Z_{SNII},feedback} = \frac{F_Z \rho_*}{t_{SN}} \tag{7.6}$$

The rate of metals ejected from a population of SNIas is just proportional to the number of SNIa per unit time and mass (eq. 7.3) and the stellar mass of the stellar particle:

$$\mathcal{S}_{Z_{SNIa},feedback} = m_Z \frac{dN_{\mathrm{SNIa}}}{dtdM} \rho_* \tag{7.7}$$

where $m_Z = 1.3$ M$_\odot$ is the mass of metals ejected in a single SNIa.

7.5 Stellar Mass Loss

A stellar population can lose mass through supernova explosions and stellar winds from WR stars, AGB stars, etc. These processes inject mass, momentum, energy and metals back to the gas. The code uses a mass loss function, $f_{\mathrm{loss}}(t_{\mathrm{age}})$ for the fractional stellar loss from a single stellar population of an age t_{age}. It uses the fit provided by Jungwiert et al. (2001):

$$f_{\mathrm{loss}}(t_{\mathrm{age}}) = \frac{C0_{\mathrm{ml}}}{t_{\mathrm{age}} + T0_{\mathrm{ml}}} \tag{7.8}$$

where $C0_{\mathrm{ml}} = 0.05$ and $T0_{\mathrm{ml}} = 5$ Myr are the constants of the fit. Figure 7.3 shows that 10% of the stellar mass is lost after 40 Myr, basically through SNII explosions and stellar winds from massive stars. After 2 Gyr, 30% of the initial mass is lost, basically due to supernovae-Ia and winds from AGB stars and other evolved stars. Based on this model, the rate of mass loss of a single stellar population can be expressed as:

$$\frac{dM_*(t_{\mathrm{age}})}{dt} = -f_{\mathrm{loss}}(t_{\mathrm{age}}) M_*(t_{\mathrm{age}} = 0) \tag{7.9}$$

where $M_*(t_{\mathrm{age}})$ is the stellar mass of a population of age t_{age}. Finally, the source term in the continuity equation coming from stellar loss (Eq. 6.1) can be expressed as:

$$\mathcal{S}_{\rho_{\mathrm{gas}},\mathrm{Stellar\ mass\ loss}} = \sum_i \rho_*(t_{\mathrm{age,i}} = 0) f_{\mathrm{loss}}(t_{\mathrm{age,i}}) \tag{7.10}$$

where the sum includes all stellar particles (single stellar populations) inside a given volume with an initial stellar density of $\rho_*(t_{\mathrm{age,i}} = 0)$ and an age $t_{\mathrm{age,i}}$.

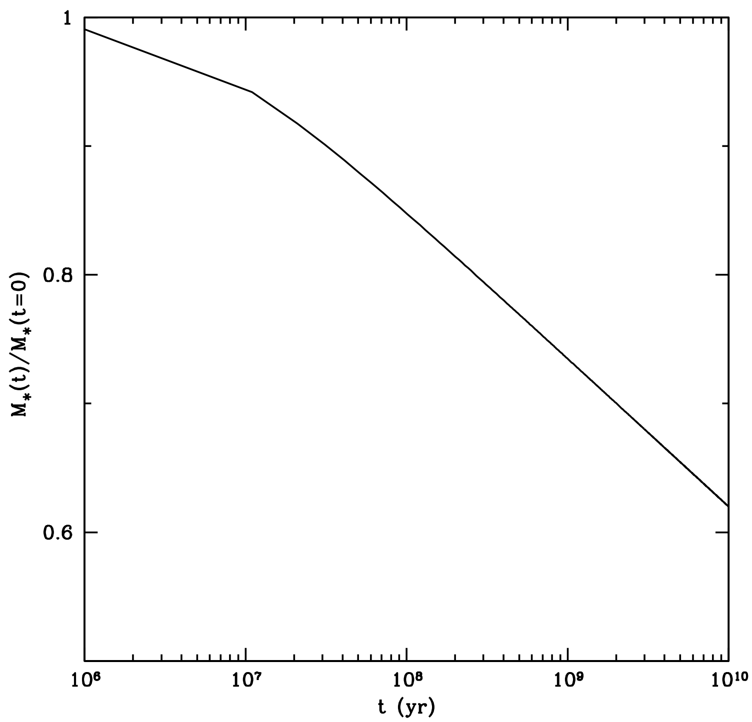

Figure 7.3 Loss of stellar mass according to the fit of Jungwiert et al. (2001)

Based on the above term, the source terms in the momentum, energy and metals equations (Eq. 6.2-6.3 and 6.6-6.7) can be expressed as:

$$\mathcal{S}_{\mathbf{u},\text{Stellar mass loss}} = \frac{\mathcal{S}_{\rho_\text{gas},\text{Stellar mass loss}}}{\rho_\text{gas}}\,\bar{\mathbf{v}}, \tag{7.11}$$

$$\mathcal{S}_{E,\text{Stellar mass loss}} = \mathcal{S}_{\rho_\text{gas},\text{Stellar mass loss}}\left(\mathbf{u}\cdot\bar{\mathbf{v}} + \mathbf{u}^2/2\right), \tag{7.12}$$

$$\mathcal{S}_{Z_{SNII},\text{Stellar mass loss}} = \mathcal{S}_{\rho_\text{gas},\text{Stellar mass loss}}\,X_{*,\text{SNII}}, \tag{7.13}$$

$$\mathcal{S}_{Z_{SNIa},\text{Stellar mass loss}} = \mathcal{S}_{\rho_\text{gas},\text{Stellar mass loss}}\,X_{*,\text{SNIa}}, \tag{7.14}$$

where ρ_gas is the gas density, $\bar{\mathbf{v}}$ is the velocity averaged over all stellar particles inside that volume, $\mathbf{u}$ is the gas velocity, $X_{*,\text{SNII}}$ and $X_{*,\text{SNIa}}$ are the mass fractions of metals locked into that stellar population.

8 UNDERSTANDING THE EFFECT OF STELLAR FEEDBACK IN THE INTERSTELLAR MEDIUM

The contents of this chapter will appear in the paper: *The role of stellar feedback in the formation of galaxies*, Ceverino, D., & Klypin, A. 2007, submitted for publication.

8.1 Introduction to the Interstellar Medium

Our first step in the understanding of stellar feedback in galaxies is to understand its effect in the interstellar medium (ISM) at galactic scales. The galactic ISM has a very wide range of densities and temperatures (for review see Cox, 2005; Ferrière, 2001). Three distinct phases are distinguished: the dense cold gas (giant molecular clouds (GMC), cold HI gas or diffuse clouds) with densities above 10 cm^{-3} and temperatures below 100 K, the warm component with densities between 0.1 and 1 cm^{-3} and temperatures of several thousand degrees, and the hot phase with temperatures above 10^5 K and densities below 10^{-2} cm^{-3}. This multiphase medium is set by the competition of cooling and heating mechanism and the onset of thermal instabilities. The hot ISM component ($T > 10^5$ K) is usually associated with gas heated by shocks. They can be produced by turbulent motions driven by gravitational and thermal instabilities. However, these turbulent driven shocks can only heat the gas up to 10^6 K (Wada & Norman, 2001). Only supernova explosions and stellar winds can produce larger gas temperatures (McCray & Snow, 1979; Spitzer, 1990).

2D and 3D hydrodynamical simulations of the ISM have enough resolution (parsecs) to resolve the multi-phase nature of the ISM and to explore complicated effects of stellar feedback on different scales (Rosen & Bregman, 1995; Scalo et al., 1998; Korpi et al., 1999; de Avillez, 2000; de Avillez & Breitschwerdt, 2004, 2007; Wada & Norman, 2001, 2007; Slyz et al., 2005). There is much to learn from these simulations. However, they typically focus on conditions in the solar neighborhood, which are different from what one may expect during early stages of galaxy formation. These simulations do not always follow the whole gas cycle: cooling, star formation, and stellar feedback. For example, de Avillez & Breitschwerdt (2004) include star formation but artificially restrict the rate of supernova explosions around a fixed value. However, this rate could be much higher in large star forming regions. As a result, the effect of stellar feedback is underestimated in these regions. Nevertheless, the effect of the stellar feedback in the ISM, such as the formation of hot bubbles and super-bubbles is resolved.

8.2 ISM Runs

We perform simulations of a $4 \times 4 \times 4$ Kpc^3 piece of a galactic disk with 8-16 pc resolution. These simulations fully resolve the effect of massive stars at galactic scales, so resolution is not longer an issue.

We can use this ISM-scale simulation as a benchmark for the effect of stellar feedback at galactic scales. Then, we can degrade the resolution to see which model of feedback reproduces the same overall picture at lower resolution. These simulations can then be used as testing grounds for these models at different resolutions. They tell us what are the necessary ingredients to reproduce the true effect of stellar feedback at the resolution that we can afford in cosmological simulations of galaxy formation.

We want to see the effect of stellar feedback in the typical conditions of normal disk galaxies with moderate gas surface densities, so we do not model starburst galaxies with large amounts of gas and high star formation rates. This type of study will be done in the future.

A 4 Kpc box of ISM represents a significant piece of a galactic disk. The simulation resolves the dense galactic plane, where molecular clouds are formed. This is important in order to follow star formation correctly. At the same time, the simulation follows the gas at few Kpc above the galactic plane. This height is similar to the scale-height of the diffuse warm phase of the ISM (Cox, 2005).

The simulation includes radiative cooling and UV heating from a uniform UV field at redshift 0 as described in section 6.2. Star formation happens in the highest density peaks with a density threshold of 100 cm^{-3}. In each star formation event, 5 % of the mass in gas inside a volume element is converted into a stellar particle with a mass of 88 $M_\odot$within a time-step set by the Courant condition ($\sim 2 \times 10^3$ yr). The supernova model is used for stellar feedback and SNIa is not included. The metallicity is assumed solar and constant throughout the simulation.

8.3 Initial Conditions

The initial distribution of gas density is uniform in the x and y directions of the box. In the z-direction, the density profile declines at both sides of the middle plane, $z = z_0 = 2$ Kpc. This plane defines the galactic plane for this ISM model:

$$n_H = n_0 \cosh^{-2}\left(\frac{z - z_0}{z_d}\right) \tag{8.1}$$

where n_0 is the gas density in that plane and z_d is the scale-height.

The choice of parameters sets the conditions of a quiescent normal galactic disk, $n_0 = 1$ cm^{-3} and $z_d = 250$ pc. Thus, the surface density is , $\Sigma_{\rm gas} = 16$ $M_\odot$

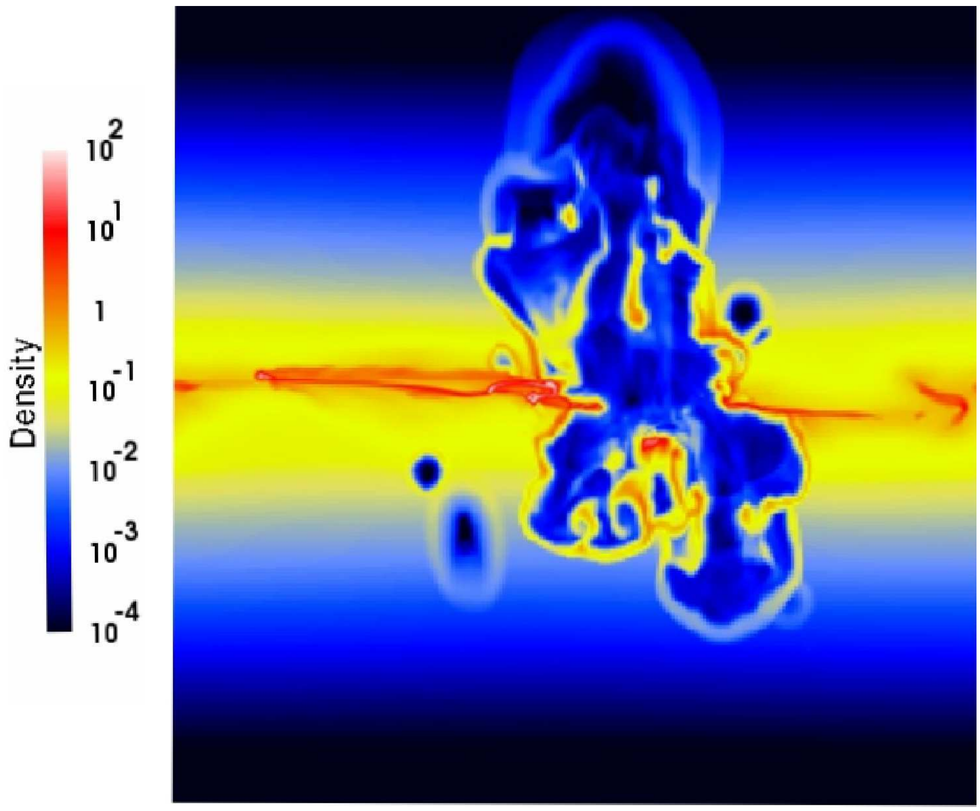

Figure 8.1 Formation of a galactic chimney. Edge-on slice through the simulation showing the gas density distribution perpendicular to the galactic plane. The chimney outflow is not a homogeneous, coherent flow: it is turbulent and it has dense and cold clumps embedded into the flow.

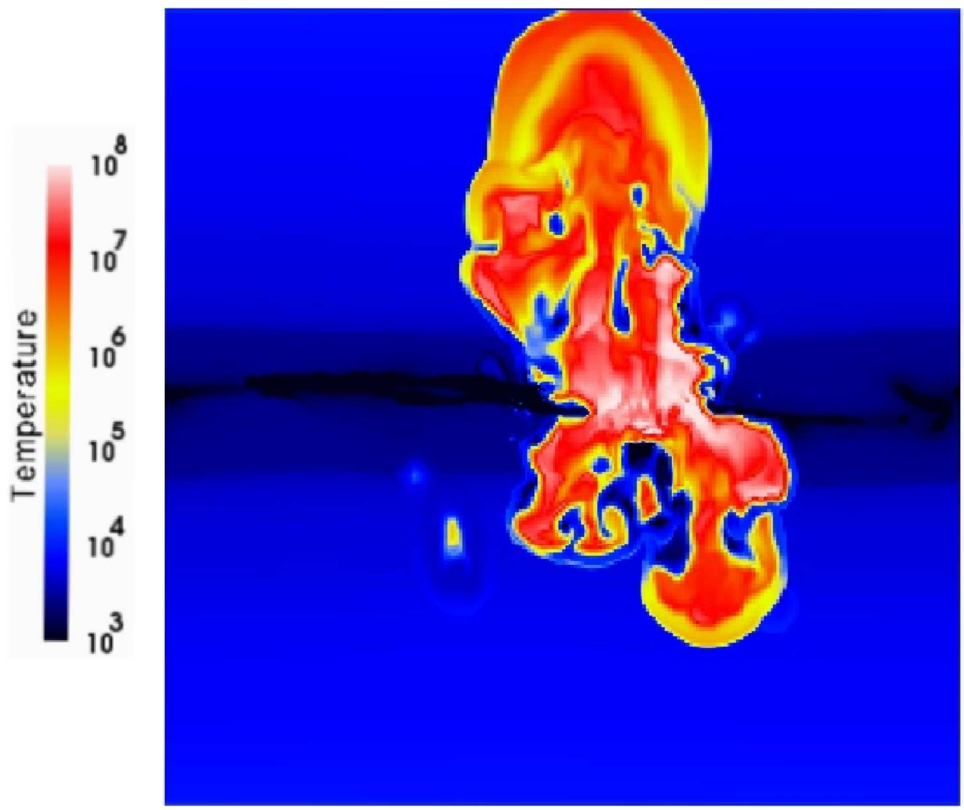

Figure 8.2 Formation of a galactic chimney. Edge-on slice through the simulation showing gas temperature. The core of the chimney reaches 10^7-10^8 K.

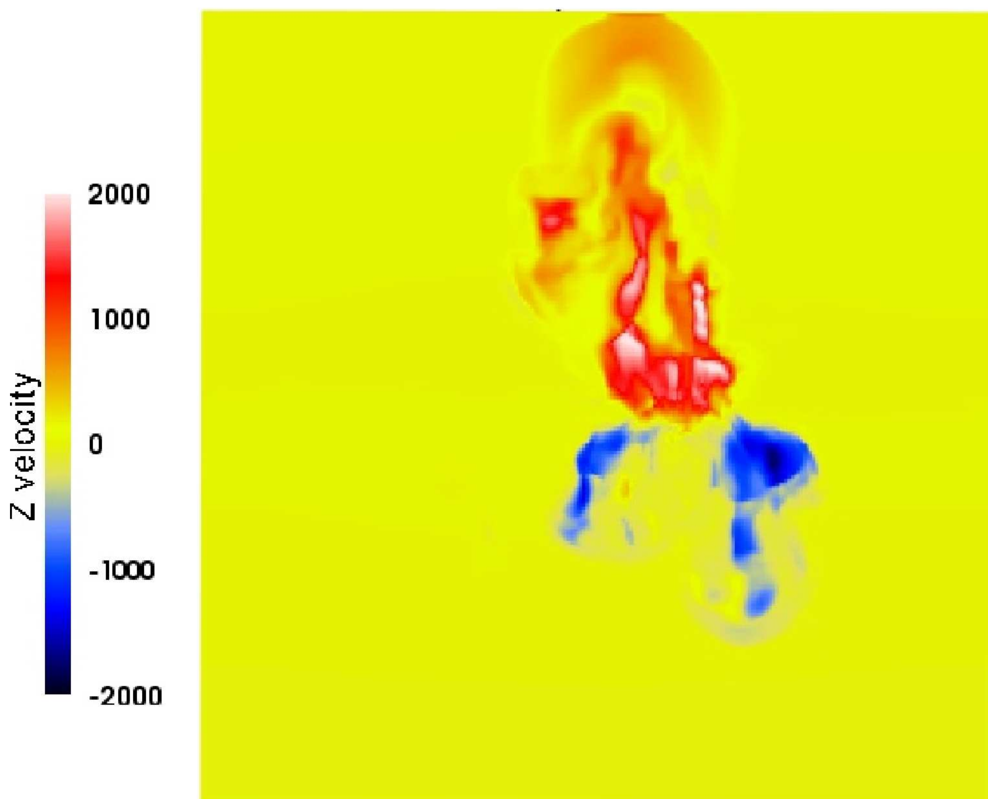

Figure 8.3 Formation of a galactic chimney. Edge-on slice through the simulation showing velocity in the vertical direction, perpendicular to the galactic plane. Outflow velocities exceed 10^3 km s^{-1}. This hot material is able to escape the disk and it generates a galactic wind.

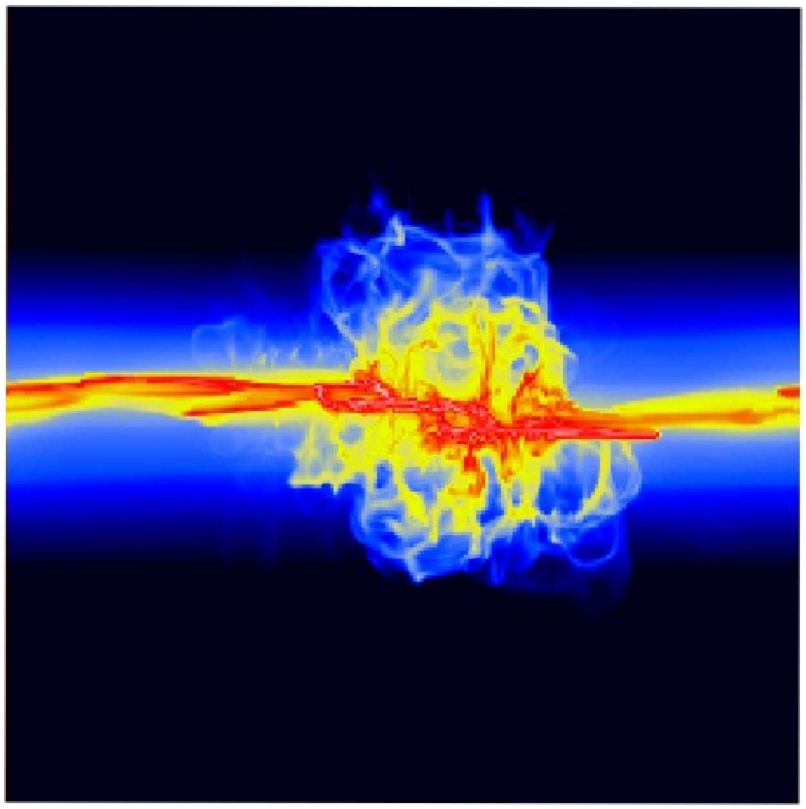

Figure 8.4 Formation of a galactic chimney. Edge-on slice through the simulation showing gas column density in arbitrary units.

pc^{-2}. The system is originally in hydrostatic equilibrium with a temperature of 10^4 K. No stars are present at the beginning of the simulation. The box has open boundaries in the z-direction. So, all material that cross these boundaries escapes the system.

The initial velocity field consists of a sum of plane-parallel velocity waves:

$$u_x = \sum_{i,j,k} A_x(i,j,k) \sin(\vec{k} \cdot \vec{r}) \exp - \left(\frac{z - z_0}{z_d} \right)^2 \tag{8.2}$$

$$u_y = \sum_{i,j,k} A_y(i,j,k) \sin(\vec{k} \cdot \vec{r}) \exp - \left(\frac{z - z_0}{z_d} \right)^2 \tag{8.3}$$

$$u_z = \sum_{i,j,k} A_z(i,j,k) \sin(\vec{k} \cdot \vec{r}) \exp - \left(\frac{z - z_0}{z_d} \right)^2 \tag{8.4}$$

The amplitudes are taken from a Gaussian field with a tilted power spectrum, $P_k \propto k^{-3}$, where k is the wavenumber, $k = \frac{2\pi}{L}\sqrt{i^2 + j^2 + k^2}$. i,j and k are integers running from -20 to 20 (excluding 0) and $u_0 = 20$ km s^{-1}. This is a typical spectrum of a compressible turbulent medium (Kraichnan, 1967; Vázquez-Semadeni et al., 1995).

$$A_x(i,j,k) = u_0 \frac{R_{Gauss}}{(i^2 + j^2 + k^2)^{3/2}} \tag{8.5}$$

$$A_y(i,j,k) = u_0 \frac{R_{Gauss}}{(i^2 + j^2 + k^2)^{3/2}} \tag{8.6}$$

$$A_z(i,j,k) = u_0 \frac{R_{Gauss}}{(i^2 + j^2 + k^2)^{3/2}} \tag{8.7}$$

R_{Gauss} is a random number taken from a Gaussian distribution.

8.4 Galactic Chimney Formation

At the beginning of the simulation, the gas starts to move according to the turbulent velocity field. As a result, the gas accumulates where different flows converge and molecular clouds [1] naturally appear in the form of filaments and shells. However, around 90% of the volume is filled with warm and diffuse gas heated by the UV background. Star formation occurs in the cores of the cold phase. Newly formed massive stars inject energy and a cavity filled with hot and very diffuse gas is formed. This over-pressured material expands and the net result is the formation of super-bubbles. This hot gas cannot stay in the plane

[1] cold and dense phase with $n_H \geq 30$ cm^{-3} and $T \leq 300K$

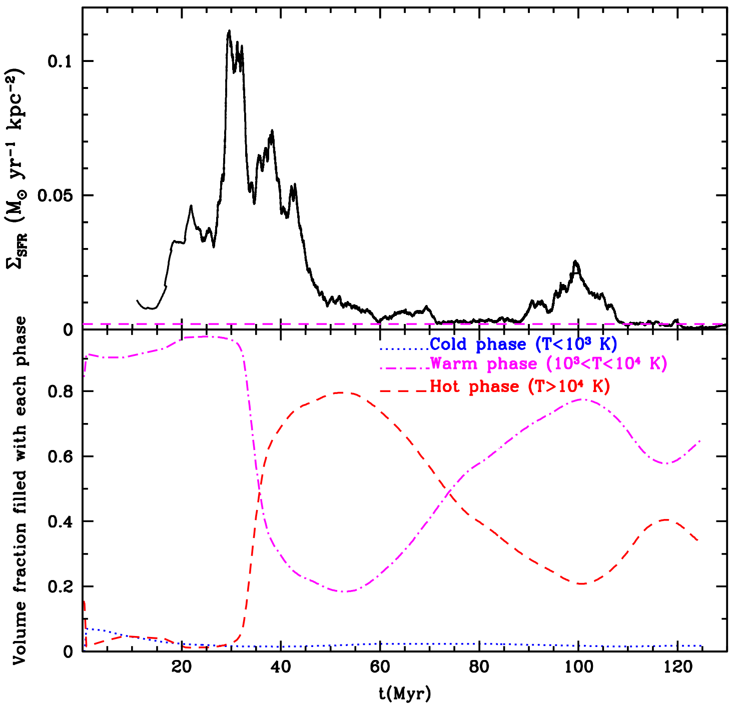

Figure 8.5 Top panel: Star formation rate surface density of the whole simulation. The value shown is also averaged over a period of $\sim 2 \times 10^5$ yr (100 time-steps). After an initial burst, the star formation rate surface density is consistent with the Kennicutt et al. (2007) empirical fit (horizontal line). Bottom panel: Fraction of volume filled with each gas phase over time. The volume occupied by the warm and the hot phase oscillates. The hot phase dominates after a burst of star formation and the warm phase dominates when the gas is cooled down. The cold phase covers a small volume, which remains constant after an initial collapse.

of the disk. As a result the bubble expands faster in the direction perpendicular to the disk because the density declines in that direction. The bubble develops into a galactic chimney (Norman & Ikeuchi, 1989). The chimney outflow does not appear as a homogeneous, coherent flow. Instead, the chimney is turbulent and has dense and cold clumps embedded into the flow. Eventually, the gas expands in the halo and cools (Figures 8.1-8.4).

Another interesting feature seen in this model is a population of isolated bubbles in the warm medium. These are the results of individual supernova explosions of runaway stars

8.5 Star Formation Rate

After an initial burst of star formation, the star formation rate is nearly constant for the rest of the evolution (Figure 8.5). We found a low star formation rate surface density, $\Sigma_{\rm SFR} = 3 \times 10^{-3}\,{\rm M_\odot\ yr^{-1}\,Kpc^{-2}}$, temporally averaged over a period of 2×10^5 yr (100 time-steps). This value is consistent with the expected value from the correlation between the star formation rate surface density and the gas surface density found in nearby galaxies (Kennicutt, 1998; Kennicutt et al., 2007). For a gas surface density of $\Sigma = 12\ {\rm M_\odot\ pc^{-2}}$ at t=90 Myr, the expected value from the Kennicutt et al. (2007) fit is $\Sigma_{\rm SFR} = 2 \times 10^{-3}\,{\rm M_\odot\ yr^{-1}\,Kpc^{-2}}$. This is very close to our results.

As observers usually do, we also calculate the gas consumption time-scale, $\tau = {\rm M_{GMC}/SFR}$, in the simulated molecular clouds, assuming that gas with a density higher than 30 ${\rm cm^{-3}}$ is mainly within GMCs. In our simulations, the amount of gas in molecular clouds is ${\rm M_{GMC}} = 8 \times 10^6\ {\rm M_\odot}$ at t=90 Myr. The star formation rate at that time is ${\rm SFR} = 4.8 \times 10^{-2}\,{\rm M_\odot\ yr^{-1}}$. As a result, the gas consumption time-scale in the simulated clouds is $\tau \approx 170$ Myr. This is quite long compared with the typical free-fall time-scale inside molecular clouds, ${\rm t_{ff}} = (3\pi/32G\rho)^{1/2} \approx 4$ Myr for $n_H = 100\ {\rm cm^{-3}}$.

In our simulations, the star formation efficiency over a free-fall time-scale, the fraction of gas consumed in stars during a free-fall time-scale, is only 2.5%. This value is consistent with observations (Zuckerman & Evans, 1974). Krumholz & Tan (2007) report a range of 0.6%-2.6% for the whole population of GMCs of the Milky-Way. Our value is also consistent with an efficiency of $\sim 3\%$ found in simulations of GMCs (Vázquez-Semadeni et al., 2003; Clark et al., 2005). Finally, our results also agree with the model of a turbulent-dominated GMC, described in Krumholz & McKee (2005). They give an efficiency per free-fall time-scale of 1.5%-3% for typical values of their model.

After 100 Myr, only 10% of the gas in the simulation has been converted into stars. Our simulations still have plenty of cold ($T \leq 10^3$ K) gas after 100 Myr. The surface density of this cold gas is $\sim 5\ {\rm M_\odot\ pc^{-2}}$. This value agrees with the

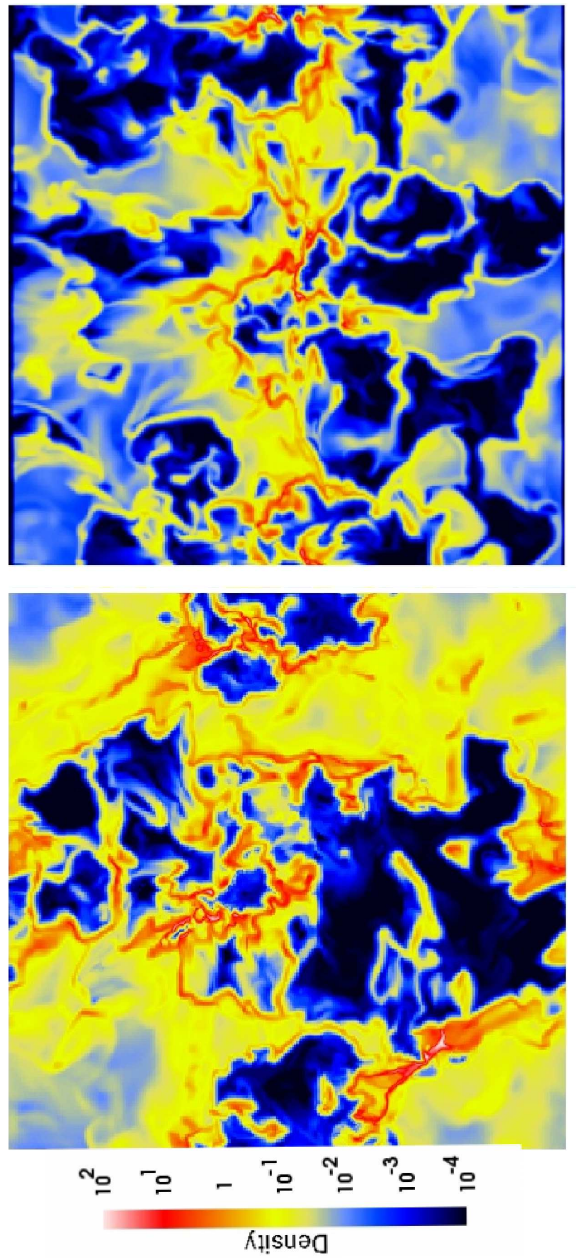

Figure 8.6 Snapshot of the model after 113 Myr, showing the density in cm^{-3}. The left panel shows a face-on view of the galactic plane ($z = z_0$) and the right panel shows an edge-on view perpendicular to that plane. The three phases of the ISM are clearly visible: dense clouds, a diffuse medium and low densities bubbles.

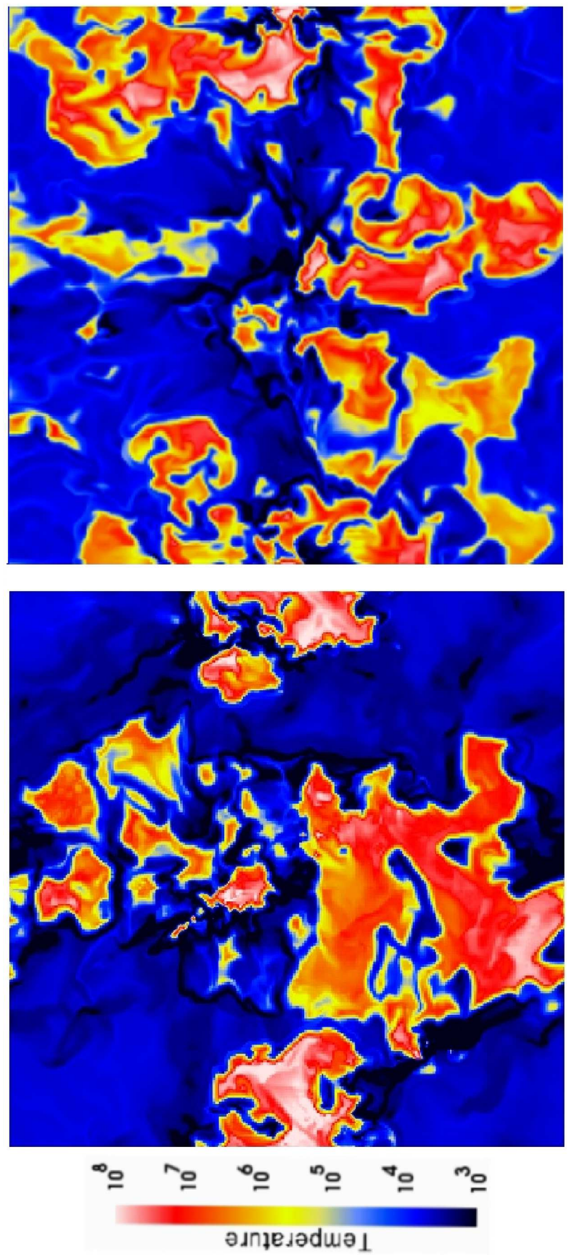

Figure 8.7 Snapshot of the model after 113 Myr, showing gas temperature in Kelvin degrees. The left panel shows a face-on view of the galactic plane ($z = z_0$) and the right panel shows an edge-on view perpendicular to that plane. The three phases of the ISM are visible: cold clouds, a warm medium and hot bubbles.

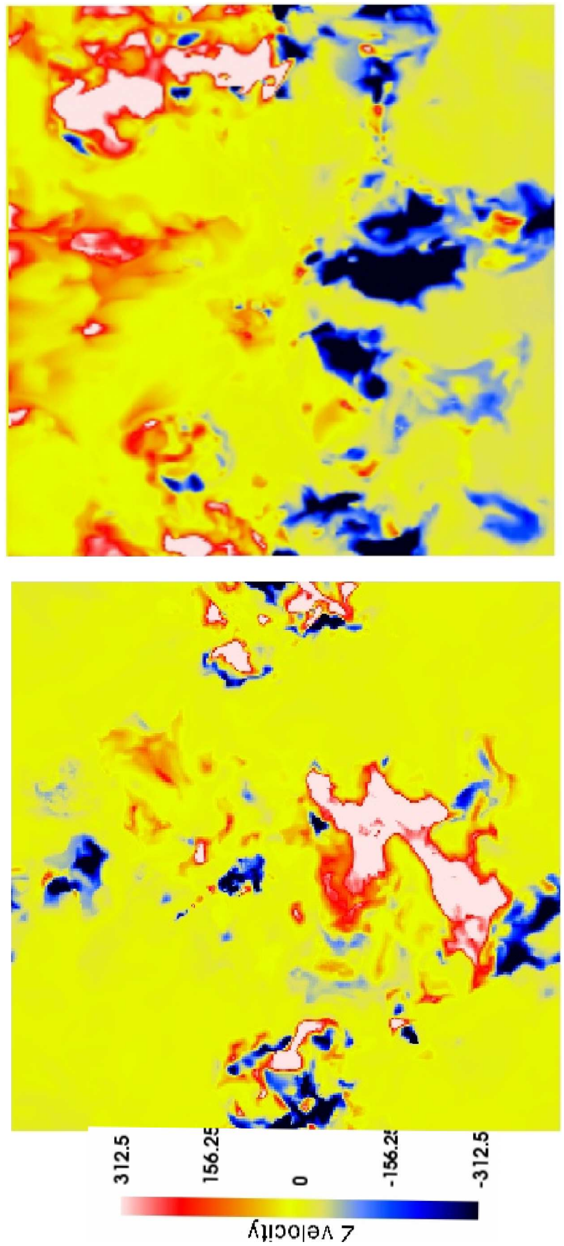

Figure 8.8 Snapshot of the model after 113 Myr, showing gas velocity in the z-direction. The left panel shows a face-on view of the galactic plane ($z = z_0$) and the right panel shows an edge-on view perpendicular to that plane. Velocities exceeding 300 km s^{-1} can be seen in outflows at both sides of the galactic plane.

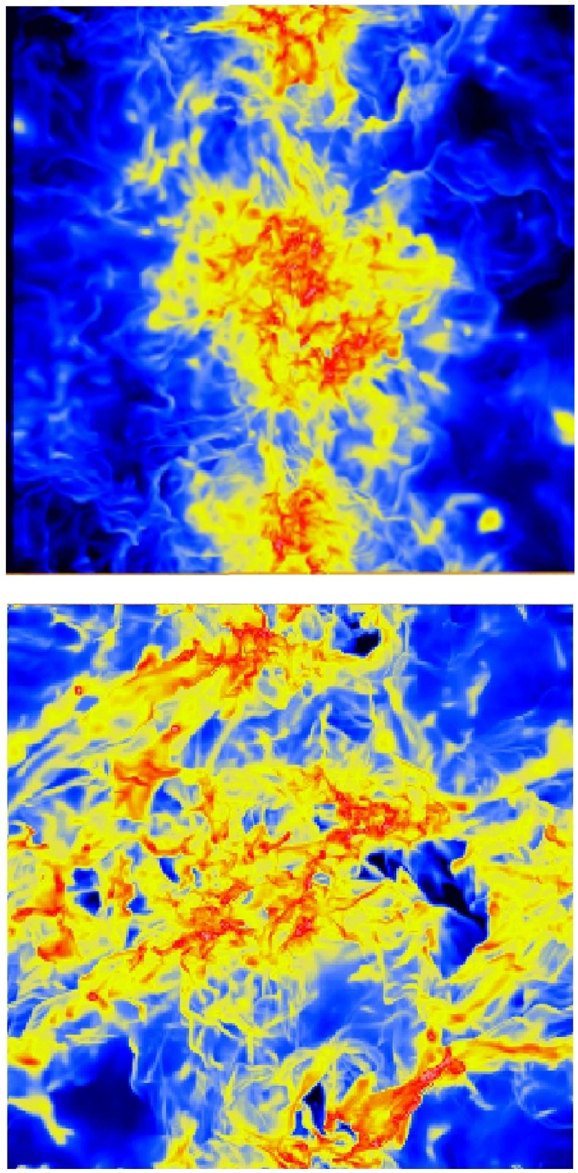

Figure 8.9 Snapshot of the model after 113 Myr, showing gas surface density in arbitrary units. The left panel shows a face-on view of the galactic plane ($z = z_0$) and the right panel shows an edge-on view perpendicular to that plane.

surface density of molecular and atomic hydrogen of ~ 6 M$_\odot$ pc^{-2} found at the solar radius (Ferrière, 2001). However, the surface density of molecular gas is low, ~ 0.5 M$_\odot$ pc^{-2}, compared with the observed value of ~ 2.5 M$_\odot$ pc^{-2} (Ferrière, 2001). This partially explains why our star formation efficiency over a free-fall time-scale is in the higher end of the observed range.

To conclude, stellar feedback is able to regulate star formation on galactic scales because it regulates the amount of gas available for star formation. Stellar feedback heats and disperses the cold and dense gas after a star formation event. In a single star formation event, a stellar particle of ~ 90 M$_\odot$ is created. This implies the formation of a single high-mass star embedded in a small stellar cluster. Due to the resolution limit, our simulation can not follow the details of the star formation process below ~ 10 pc scales, only the overall net effect. This effect is the formation of a small stellar cluster with an efficiency of 5%. As we pointed in section 5, the star formation efficiency of Galactic stellar clusters is high, regardless the details of their formation. However, although the star formation efficiency is high, subsequent feedback processes produce a low average star formation.

8.6 Volume Filling Factors in the ISM

Figure 8.5 also shows that the net effect of stellar feedback is to produce the hot phase of the ISM. After the initial strong burst of star formation, this phase can cover up to 80% of the total volume. This represents almost the entire volume above a height of 400 pc from the galactic plane. However, pockets of warm gas are embedded in this hot flow even at 2 Kpc away from the plane. It has the same inhomogeneous structure seen in the galactic fountain of figure 8.1. After 100 Myr, $\sim 25\%$ of the gas is able to escape the computational volume.

Most of the hot gas is lost or cooled down after 100 Myr. As a result, the volume of hot gas decreases because the star formation is low and the injection of energy is lower than in the initial burst. The simulation settles into a more quiescent regime in which the volume occupied by the warm and hot phases oscillates in a self-regulated gas cycle. In this cycle, bursts of star formation (much smaller than the initial one) produce super-bubbles and galactic chimneys of hot gas. Therefore, the volume of hot gas increases. As the star formation fades, the bubbles cool down and the fraction of hot gas decreases until the next stellar burst. This pattern reflects the star formation history. The particular fraction of hot and warm phases at any moment does depend to the particular star formation history, 10-40 Myr before that moment.

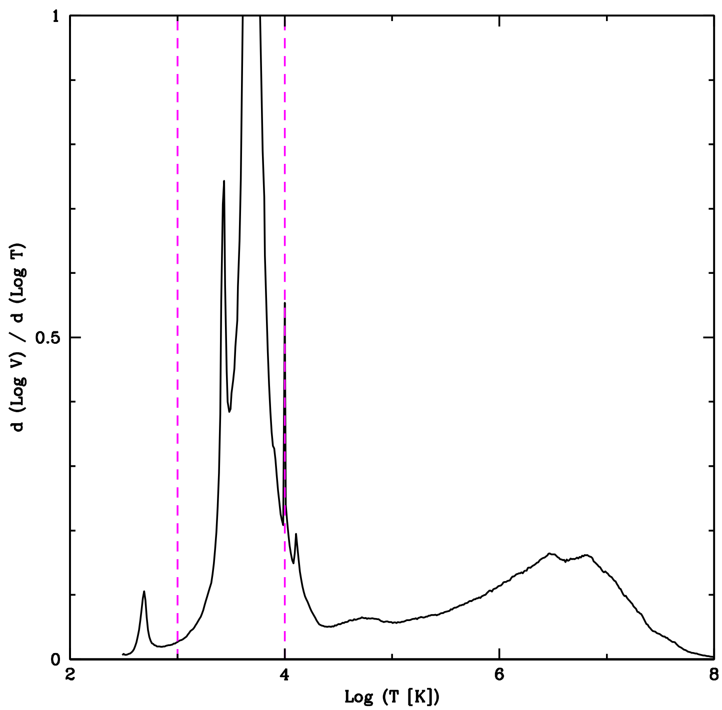

Figure 8.10 Distribution of the gas temperature at 113 Myr. The distribution has three different peaks corresponding to three different gas phases of the ISM: cold, warm and hot. Two vertical lines show the temperature cuts used throughout the paper at $T = 10^3$ K and $T = 10^4$ K.

8.7 Late Stages of Evolution

The latter stages of the simulation offer a more representative view of the ISM. The effect of the initial conditions is gone. So, we can study the characteristics of this feedback-driven ISM. We select a snapshot at 113 Myr after the second burst of star formation. At that moment, the warm phase covers $\sim 60\%$ of the volume and the hot phase filled $\sim 40\%$. X-ray emitting gas with temperatures above $10^{5.5}$ K occupies $\sim 20\%$ of the volume inside a height of 250 pc above the galactic plane. This is roughly consistent with ISM simulations with a 1-pc resolution (de Avillez & Breitschwerdt, 2004), Galactic ISM models and observations (Ferrière, 1998).

Figures 8.6-8.9 show representative slices of the box. The medium is very

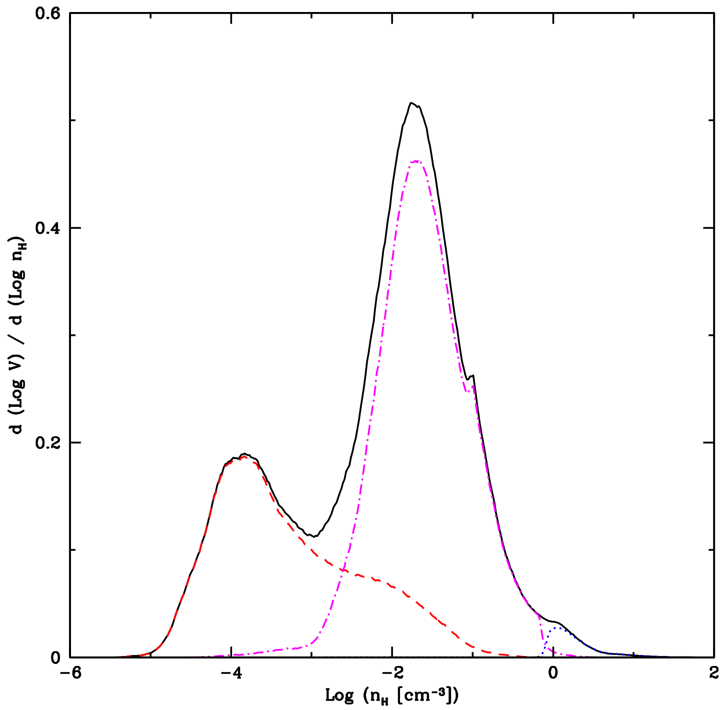

Figure 8.11 Density distribution at 113 Myr and the contribution of the three phases. The dotted curve shows the cold phase ($T < 10^3$ K), the dashed curve shows the hot phase ($T > 10^4$ K), and the dash-dotted curve shows the warm phase ($10^3\,\mathrm{K} < T < 10^4$ K). The distribution is clearly bimodal. The peaks correspond to the hot and warm phases. The cold phase dominates the high-density tail.

inhomogeneous at different scales. Large bubbles of low density coexist with long filamentary structures of dense clouds. Overall, the medium covers more than 6 orders of magnitude in density and temperature. The cold phase forms dense and cold clouds near the galactic plane. The warm phase fills old cooled bubbles and low-density clouds. Finally, the hot phase is present in the form of hot bubbles a few hundred pc wide and Kpc-scale chimneys. The gas in these chimneys is flowing away from the plane with velocities exceeding ± 300 km s^{-1}. These bubbles even break the dense plane in hot spots surrounded by cold and dense shells. All of these phenomena associated with the hot phase are driven by stellar feedback. As a result, one effect of stellar feedback is to sustain a three-phase ISM.

The distribution of temperature clearly shows the three main peaks of the three phases of the ISM (Figure 8.10). The two local minima correspond to thermally unstable gas. The minimum around 10^3 K, between the peaks of the cold and warm phases, is produced by the competition of UV heating and radiative cooling. This corresponds to the unstable regime of the classical two-phase model of the ISM in thermal equilibrium (Cox, 2005). The dip between 10^4 and 10^5 K results from the peak of the cooling curve. The gas cools very fast at these temperatures. As a result, it usually appears at the interface between hot and warm gas. As an exception, old bubbles at these temperatures are present in the simulation with very low densities and far away from the plane. So, their cooling time is very long. This temperature distribution supports the temperature cuts used throughout the paper to distinguish the three phases: 10^3 K for the cut between cold and warm phases and 10^4 for the warm-hot cut. To summarize, this model of the ISM reproduces the main properties of the temperature distribution of the ISM (Cox, 2005) and predicts that gas with very high temperatures $10^7 - 10^8$ K exists in the cores of galactic chimneys. This gas occupies only 5 % of the total volume and have a very small surface density of 4 $\times 10^{-6}$M$_\odot$ pc^{-2}.

These three phases of the ISM are also clearly visible in the density distribution (Figure 8.11). We use the temperature cuts defined before to see the contribution of the different phases. Thus, the hot phase dominates the low-density range, below 10^{-3} cm^{-3}. The warm phase covers intermediate densities, and the cold phase dominates the high density tail above 1 cm^{-3}. The density distribution of any of the three phases cannot be described by a single lognormal distribution, as claimed in Wada & Norman (2001). Instead, a combination of several lognormal distributions may give a better approximation (Robertson & Kravtsov, 2007).

The distribution of velocities (Figure 8.12) shows two distinct features. The warm phase contributes to a strong peak around 30 km s^{-1}. The hot phase dominates the high velocity tail. It has velocities as higher as 2000 km s^{-1}. The gas with velocities in this tail can easily escape the system. This gas forms hot outflows and galactic chimneys.

Finally, figure 8.13 shows the distribution of the Mach number, M=u/c, where

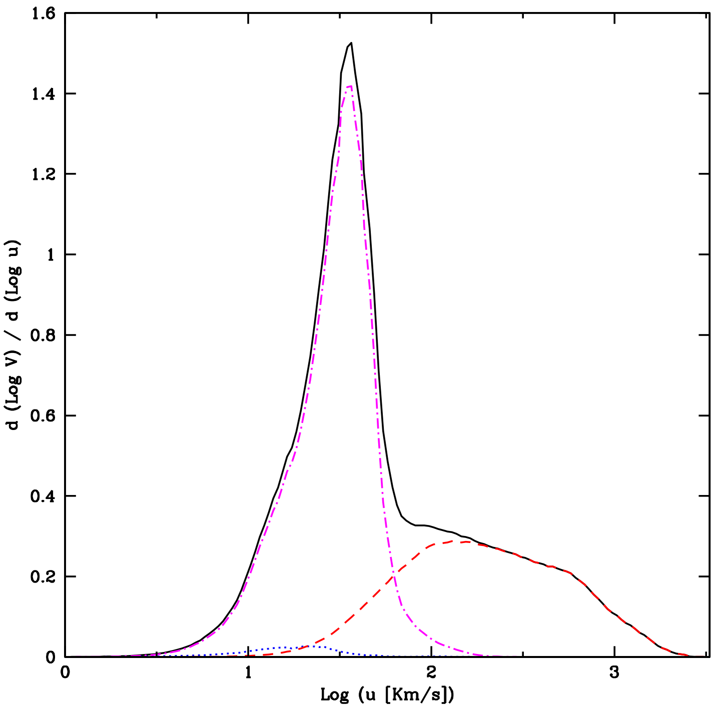

Figure 8.12 Distribution of gas velocity at 113 Myr. The curves represent the 3 gas phases as in figure 8.11. Cold and warm phases have moderate velocities, mostly below 100 km s^{-1}. The hot phase dominates the high velocity tail of the distribution with velocities up to 2000 km s^{-1}. These are outflows of gas which escape the system.

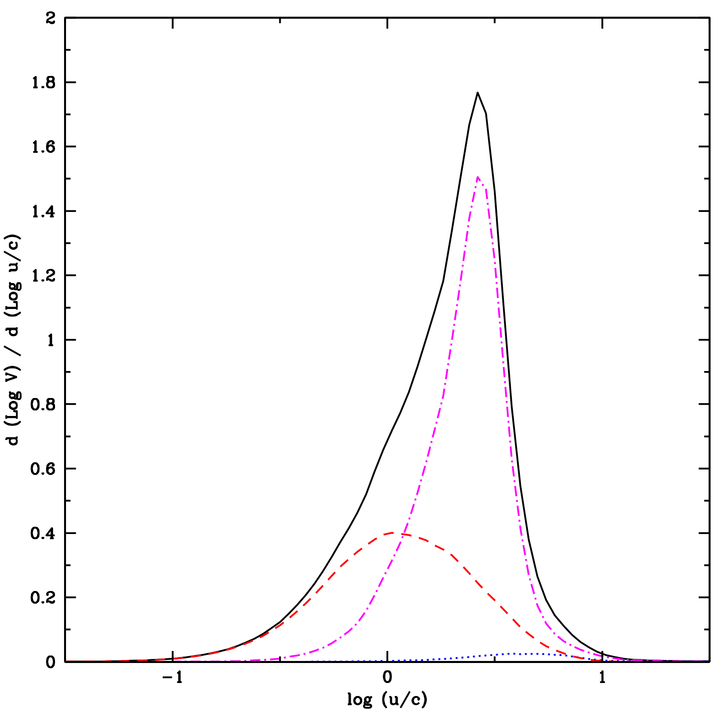

Figure 8.13 Distribution of the Mach number (u/c). The curves represent the 3 gas phases as in figure 8.11. 80% of the gas has supersonic motions. Only half of the hot phase has subsonic motions

u is the gas velocity and c is the sound speed. The distribution shows that 80% of the volume has supersonic motions. Almost all of the warm phase, half of the hot phase and all of the cold phase are supersonic flows. The subsonic range is dominated by the hot phase, In conclusion, the ISM can contain high supersonic motions, driven by stellar feedback.

8.8 Degrading Resolution

The resolution in cosmological simulations of galaxy formation is much lower than the simulations of the ISM presented before, so we can wonder if this picture of stellar feedback will hold if the resolution is degraded. Therefore, the same ISM models have been performed with high resolution (14 pc) and with low resolution (60 pc). The fraction of volume filled with each gas phase is used as a proxi to check the global effect of stellar feedback in the ISM (Figure 8.14). The left panels show that the hot phase covers a significant volume.

At low resolution and without runaway stars (top right panel), the hot gas is almost absent from the simulation. Small filaments are not resolved and the subsequent star formation is suppressed in these areas which can be easily broken by stellar feedback. As a result, star formation is concentrated at the center of big clumps of gas. Stars inject energy in high density regions, so this energy is radiated away without any thermodynamical effect in the medium.

However, if the model of runaway stars is included, the hot phase is recovered at low resolution. Stars can now migrate away from high density regions, so the injection of energy is more efficient in forming hot gas. As a result, the model with runaway stars can reproduce the effect of stellar feedback even at a resolution of 60 pc.

8.9 The Expansion of a Hot Bubble

As an example of the conditions of the overheating regime discussed in section 5, now we can ask how a hot bubble develops in the first place. Figure 8.15 shows the physical conditions of a single volume element over 10 Myr. This volume develops a hot and dilute medium starting from a cold and dense phase. The gradients are computed using a 3-point finite differences expression using the adjacent cells.

At the beginning, there are no stars present inside that volume, so there is no feedback heating. At the same time, the density is high enough so that the radiative cooling dominates over the UV background heating. As a result, the

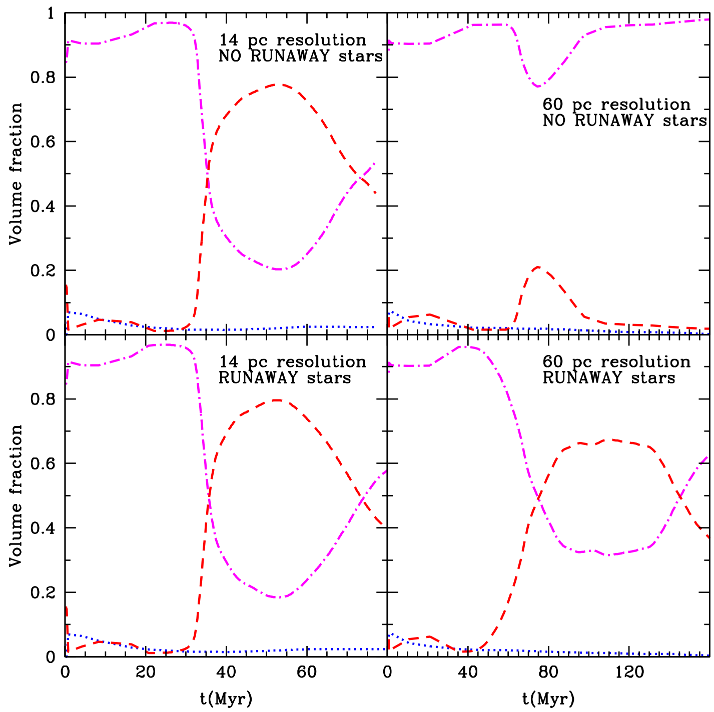

Figure 8.14 The panels show the evolution of the volume occupied by each phase of the gas in four different models. The curves represent the 3 gas phases as in figure 8.5. The hot phase is almost lost for the low resolution run without runaway stars (top right panel). If runaway stars are included, the hot phase is recovered at low resolution. As a result, a fraction of runaway stars produces an effect on the global ISM and its more evident in low resolution runs.

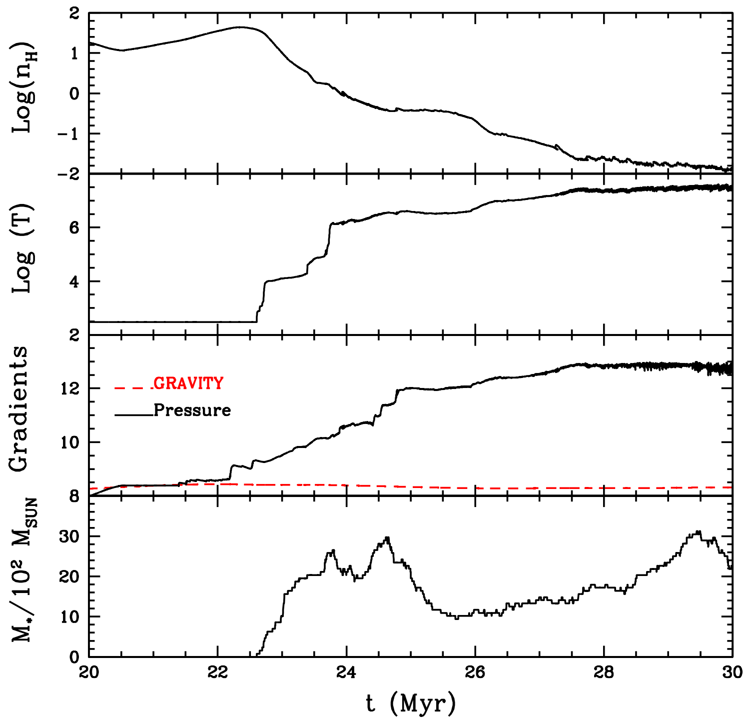

Figure 8.15 Evolution of the properties of a single volume element (Temperature, density, gradients of pressure and gravity, and the mass in young stars) in a run with 8 pc resolution. It shows an over-pressured volume that expands due to stellar feedback and produces a hot cavity filled with low-density gas.

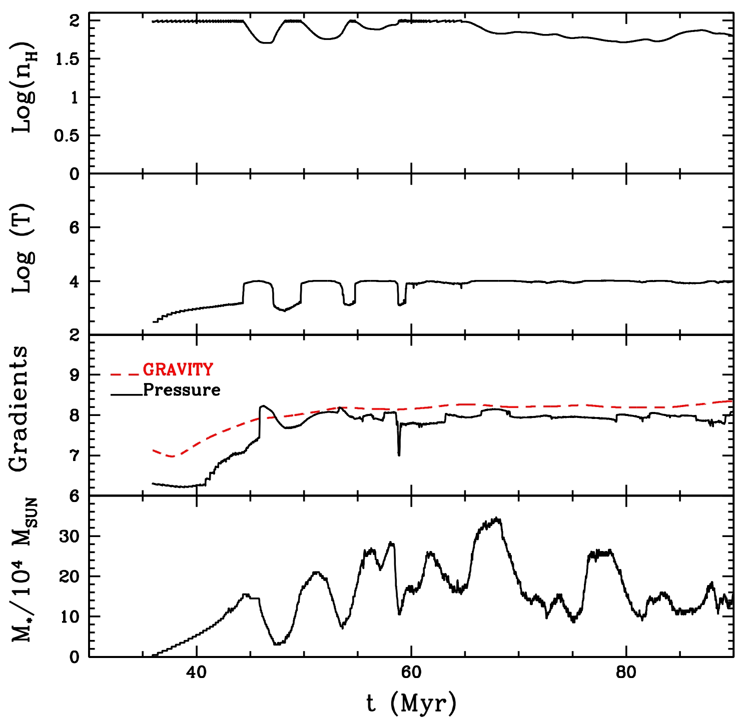

Figure 8.16 Same as figure 8.15 but with a resolution of 30 pc. It shows how the hot bubble cannot develop when the gradients of pressure do not dominate over gravity.

medium stays at the floor temperature of 300 K. The medium is also in hydrostatic equilibrium.

The situation drastically changes when young stars appear. They are not born inside that particular volume. Instead, they are drifting slowly from adjacent cells. The result is that this young population injects energy into the medium, so heating dominates over cooling initially. The system responds by increasing the temperature. As a result, the cooling rate increases and the medium reaches a balance between cooling and heating rates in a very short time-scale. This is because the cooling time is very short in those conditions. The net result is a medium slightly hotter than its surroundings so this over-pressured region expands and the density inside that volume decreases.

Around 10^4 K, the cooling curve is a very steep function of temperature, so the temperature increases very slowly. But, at the same time, the density drops faster. As a result, the cooling rate decreases. This expansion is fueled by a roughly constant injection of energy from massive stars.

When the conditions of eq. 5.5 are fulfilled, the medium can pass through the peak of the cooling curve, somewhere between $10^4 - 10^5$ K. After that, the gas has a low density and a temperature of few millions degrees. As a result, heating dominates over cooling and a hot cavity is formed.

Figure 8.16 shows a different situation. The volume is selected to be the high-density core of a molecular cloud formed in the low-resolution run shown in the top-right panel of figure 8.14. Stellar feedback from the stars formed in that core are able to heat the gas only to 10^4 K. The gradients of pressure do not overcome gravity. The condition of bubble expansion is not fulfilled , eq. (5.7). As a result, the density remains high and a hot bubble can not develop.

8.10 Summary and Conclusions

Heating from stellar feedback has an effect in the ISM only when it dominates over radiative cooling. Section 5 shows the necessary conditions for this heating regime (eq.(5.5-5.7)). We find that a model of cooling below 10^4 K is a key ingredient to fulfill these conditions. Thus, by resolving the conditions of molecular clouds ($T \approx 100$ K and $n_H > 10$ cm^{-3}), we resolve the conditions in which stellar feedback is more efficient in the ISM on galactic scales.

We perform parsec-resolution simulations of a piece of a galactic disk in order to see the effects of stellar feedback and to test our models. When we use a realistic feedback and high resolution, the system has a low star formation rate and it forms hot super-bubbles of 100-pc scales and Kpc-scale galactic chimneys. We found that the cores of these chimneys reach temperatures of $10^7 - 10^8$ K, very low densities ($n_H < 10^{-4}$ cm^{-3}), and outflow velocities exceeding 10^3 km s^{-1}.

We then degrade the resolution to see if this picture of multi-phase ISM holds at a resolution that we can achieve in cosmological simulations. We find that runaway stars help to spread the effect of stellar feedback. They usually explode as supernovae in low-density regions, few 100 pc away from their natal molecular cloud. This is an effect found in nature (Stone, 1991) which enhances the feedback, so it needs to be included in any realistic model of stellar feedback.

Thermal feedback from young stars is able to produce long timescales of gas consumption by dissipating the star-forming gas. As a result, although this gas has high star formation efficiency, subsequent feedback processes produce a low star formation rate, averaged over all cold and dense gas. For example, the gas with a density above the density threshold for star formation can form stars with high efficiency. However, the average star formation efficiency in the simulated clouds is roughly 2.5% over a free-fall time-scale (§8.5). This is roughly consistent with estimations of the star formation efficiency in molecular clouds (Zuckerman & Evans, 1974; Krumholz & McKee, 2005; Krumholz & Tan, 2007).

9 THE ROLE OF STELLAR FEEDBACK IN GALAXY FORMATION

The contents of this chapter will appear in the paper: *The role of stellar feedback in the formation of galaxies*, Ceverino, D., & Klypin, A. 2007, submitted for publication.

In previous sections, we have shown that our models of stellar feedback follow the effect of supernova explosions and stellar winds in the ISM with a resolution of about 50 pc. The result is the formation of super-bubbles and galactic chimneys, both filled with hot and dilute gas. The net result is a multi-phase ISM and galactic outflows with large velocities.

We can now study the effect of stellar feedback in galaxy formation. We apply these feedback models in cosmological hydrodynamics simulations with a similar resolution of 35-70 pc. The simulations follows the formation of a MW-type galaxy starting from primordial density fluctuations in the early Universe.

The computational volume is a 10 h^{-1} Mpc commoving box. We apply a zooming technique (Klypin et al., 2001) to select a Lagrangian volume of 3 virial radius centered in a MW-size halo at redshift $z = 0$. Then, we resimulate that volume with higher resolution. The region has a radius of about 1.5 h^{-1} comoving Mpc. The simulation has about 5 million dark matter particles. They have three different masses. The high-resolution region is resolved with 3.4 million dark matter particles with a 7.5×10^5 $M_\odot$ mass per particle. The high-resolution volume is resolved with about 17 million volume elements at different levels of resolution. The maximum resolution is always between 35 and 70 pc. A short summary of the details of the simulations is given in table 9.1. The cosmological model assumed throughout the paper has $\Omega_m = 0.3$, $\Omega_\Lambda = 0.7$, h=0.7 and $\sigma_8 = 0.9$.

Figure 9.1 shows a slice through the box at an early moment, redshift z=5. The slice shows the density of the gas in units of Hydrogen atoms per cm^3. The high-resolution area at the center shows a cosmic web of filaments. Galaxies are forming at the nodes of this web. They accrete material mainly from the filaments. At these scales of several Mpc, the distribution of gas follows the distribution of dark matter. This is because the cosmological baryonic fraction, the ratio between the mass in gas and the total mass (gas and dark matter) is only 0.15. As a result, the gravity from dark matter dominates the total gravitational field at cosmological distances. However, at galactic scales, the gas decouples from the dark matter because other astrophysical processes: radiative cooling, star formation and stellar feedback, start to play an important role.

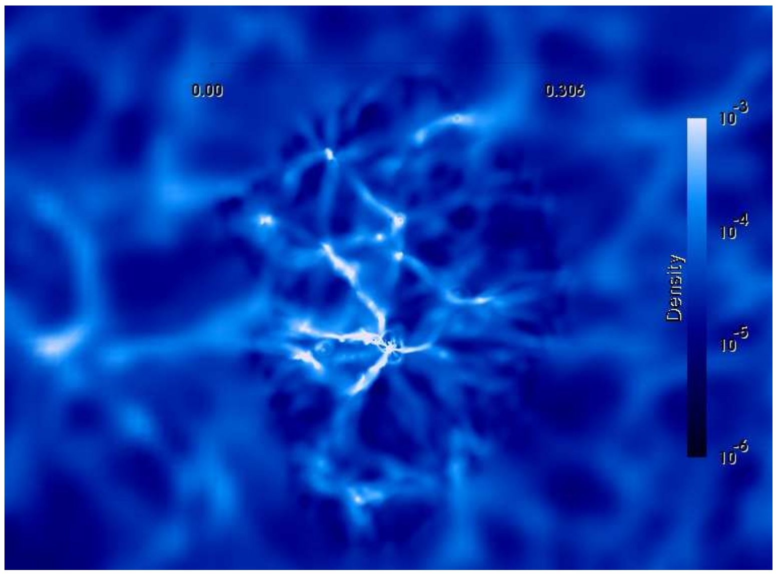

Figure 9.1 Slice through the cosmological box showing the gas density at z=5 in units of Hydrogen atoms per cm^3. It shows a fraction of 6 h^{-1} Mpc from a box of 10 h^{-1} Mpc. The area with more detail at the center is the high resolution region in which galaxies are forming. This area shows a cosmic web of filaments. Galaxies are forming at the nodes of this web.

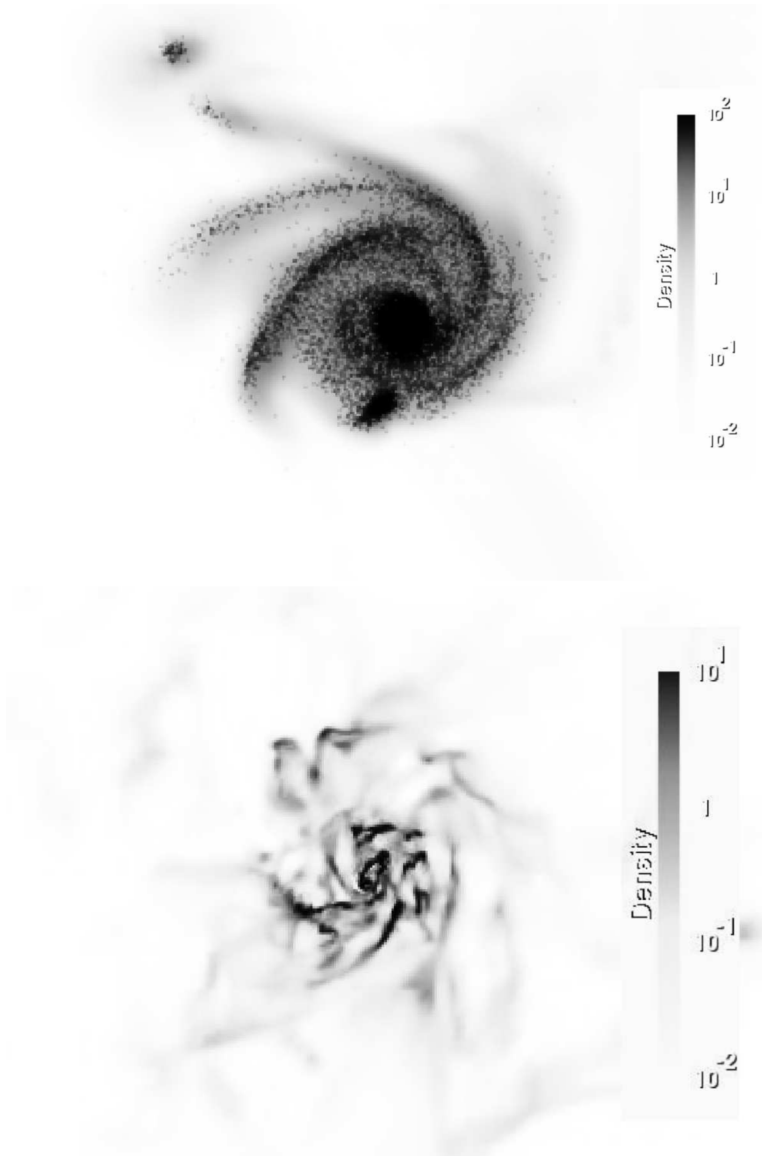

Figure 9.2 Gas density of a MW progenitor at redshift 3. The top panel shows the overcooling case. The distribution has a very concentrated and dense center. Young stars appear as points. The bottom panel shows the heating regime case. The center is less concentrated and the distribution looks clumpy. This is the case of a multi-phase ISM. The size of the images is 30 Kpc in both cases.

9.1 Heating Regime versus Overcooling Regime

We compare two cosmological simulations with the same spatial resolution but different regimes. Table 9.1 shows a summary of the two simulations. The over-cooling model has low star formation efficiency. In addition, a cosmological UV background according to Haardt & Madau (1996) is present over the whole evolution. Finally, a constant model of stellar feedback is used.

In the second simulation the heating regime develops. It has a high efficiency of star formation and the UV background is limited to its value at redshift 8. The supernova model of stellar feedback is used in this case. We use a model of star formation in which each star formation event is treated as a random process (see §6.3). In this way, we keep a moderate galactic star formation rate of ~ 10 $M_\odot$ yr^{-1} inside the main galaxy at redshift 3.

The simulation in the cooling regime has a cold galactic ISM with temperature close to 10^4 K. The simulation in the heating regime develops a 3-phase ISM. Hot bubbles develop naturally. They produce galactic chimneys that combine in a galactic wind. As a result, galactic winds are the natural outcome from stellar feedback.

Figure 9.2 shows the main MW progenitor at redshift 3 for both simulations. The cooling model has a smooth density distribution with a small enhancement due to a pattern of spiral arms. In contrast, the multi-phase model develops a clumpy medium of dense clouds surrounded by low-density bubbles. This is a multi-phase medium.

9.2 Comparison of Circular Velocity Profiles

We can see now the effect of this multiphase medium in the galaxy assembly. We use the profile of circular velocity as a proxy of the mass distribution, $V_c = \sqrt{GM/R}$, where G is the gravitational constant and M is the mass inside a radius R. Figure 9.3 shows the profile of the circular velocity for the same galaxy in the two cases. The simulation with the overcooling problem shows a strong peak in the baryonic component of the circular velocity. Both gas and stars are very concentrated in the first Kpc. In contrast, the simulation with multiphase medium has a more shallow circular velocity profile. This indicates a less concentrated galaxy with less baryons. At the virial radius, R_{vir} =16 Kpc, the virial mass at z=5 is 3.1 $\times 10^{10}$ $M_\odot$. A large fraction of this mass is dark matter, M_{dm} = 2.7 $\times 10^{10}$ $M_\odot$. The mass in gas is M_{gas} = 0.24 $\times 10^{10}$ $M_\odot$ and the baryons locked into stars accounts for only 0.14 $\times 10^{10}$ $M_\odot$.

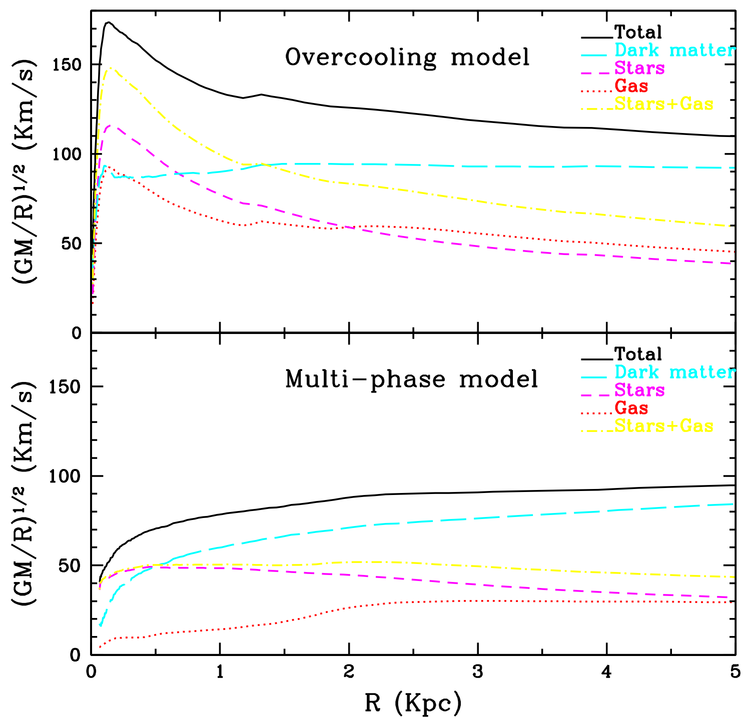

Figure 9.3 Circular velocity profile of the main progenitor of a MW-type galaxy at redshift 5. The top panel shows the results of an inefficient stellar feedback. The galaxy is too concentrated and has a too massive spheroidal component. By contrast, the bottom panel shows a regime in which stellar feedback is more efficient and it can regulate the growth of the galaxy. The maximum resolution in both cases is 70 pc.

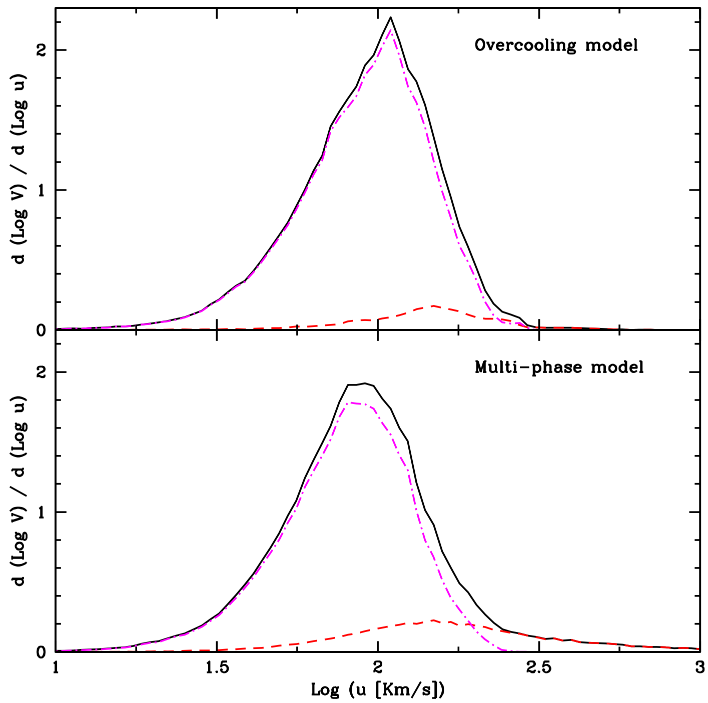

Figure 9.4 Distribution of velocities at the highest levels of the resolution for two models. The dashed curve represents the hot phase with $T > 10^4$ K and the dash-dotted curve represents gas with temperatures bellow 10^4 K. The bottom panel shows a longer tail of high-velocities. These are galactic outflows which can reach velocities exceeding 10^3 km s^{-1}.

Table 9.1. Parameters of cosmological models.

Parameter	Models	
Comoving box size	14.28 Mpc	
Number of DM particles	5.4×10^6	
DM particle mass	$7.5 \times 10^5 M_\odot$	
Number of cells	17.5×10^6	
Max. resolution (proper)	35-70 pc	
Max. number of stars	3.7×10^6	
Min. mass of stellar particle	10^4M$_\odot$	
Model name	Overcooling	Multi-phase
UV flux	H& M96	H& M96 but constant after $z = 8$
Star formation time scale τ	4×10^7 yrs	4×10^6 yrs
Model for stellar energy release	Constant	SN model
Runaway stars	not included	included

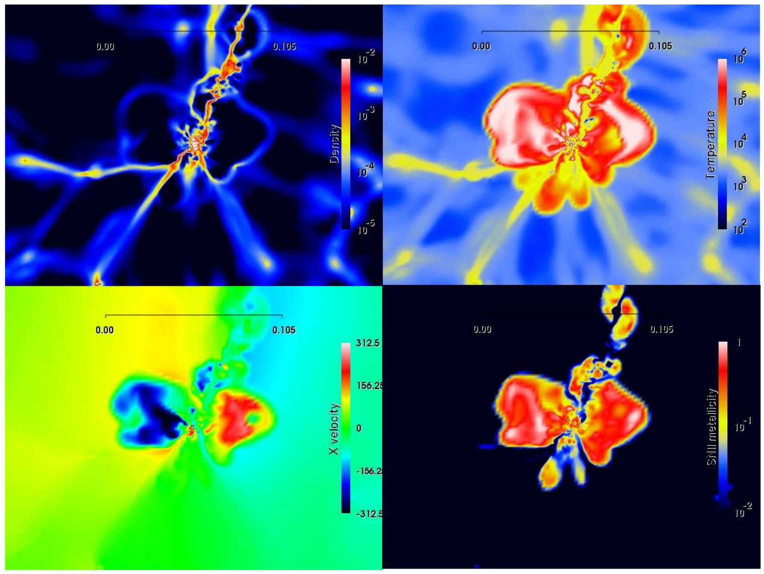

Figure 9.5 This panel shows a galaxy at redshift 3.4 with a resolution of 45 pc. The figures show slices of 600 Kpc on a side of gas density (top left), temperature (top right), velocity in the horizontal direction (bottom left), and metallicity (bottom right). There are inflows of low-metallicity gas in cold filaments, as well as outflows of hot, metal-rich gas produced by chimneys in a multi-phase interstellar medium. Outflow velocities exceeds 300 km s^{-1}. The virial radius is 70 Kpc and the total virial mass is 10^{11} solar masses.

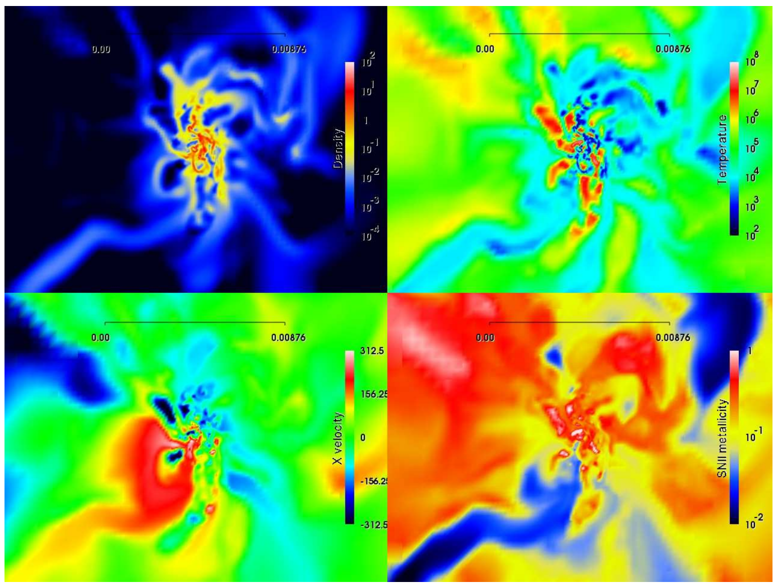

Figure 9.6 The same as in figure 9.5, but now the size of the images is 50 Kpc. It shows a multi-phase ISM of cold and dense clouds surrounded by bubbles of hot and dilute gas. Inflow and outflow velocities can reach 300 km s^{-1}. The outflows are galactic chimneys powered by core-collapse supernova. Therefore, they are rich in α-elements. In contrast, the inflow of gas has almost primordial composition.

9.3 Galactic Winds and Multiphase Medium

The hot bubbles in the multi-phase medium develop galactic fountains that produce hot outflows with very high velocities: larger than 10^3 km s^{-1}. These outflows are not produced in the cooling model. The Figure 9.4 shows the difference in the distribution function of velocities for both cases. We take all cells at the highest levels of refinement. Therefore, we select a volume close to the galaxies in the simulations. The multi-phase model has a bigger fraction of hot gas with much larger velocities than in the cooling model. These outflows contribute to the high-velocity tail of the distribution. In the cooling model, the distribution drops at 300 km s^{-1}, while in the hot case the tail extends beyond 10^3 km s^{-1}.

These galactic-scale outflows can be seen in figure 9.5. It shows a slice of the simulation through the main MW-progenitor at redshift $z = 3.4$. At that redshift, its virial radius is 70 Kpc and the total virial mass is 10^{11} $M_{\odot}$. The gas density panel shows the galaxy embedded in a cosmological web of filaments. The galaxy at the center is blowing a galactic wind of hot and dilute gas with outflows velocities exceeding 300 km s^{-1}. The wind is rich in α-elements and other products of the ejecta of core-collapse supernova. These metal-rich outflows can contribute to the enrichment of the halo and the inter-galactic medium. These outflows can reach even higher velocities and can escape the galactic halo and enrich the inter-galactic medium. The galactic wind is produced by the combination of different galactic chimneys anchored in the multi-phase ISM of the galaxy.

Figure 9.6 shows this multi-phase ISM. Cold and dense clouds coexist with low-density bubbles of very hot gas. Warm gas with intermediate densities and temperatures fills areas of low star formation and inflows of gas with almost primordial composition.

9.4 Density Profile Consistent with a Cuspy Profile

Figure 9.7 shows the inner profile of density of the different components of the galaxy: dark matter, gas and stars at redshift 5. The density slope of the dark matter profile is consistent with a cuspy profile. In contrast, Mashchenko et al. (2007) reported the formation of a core rather than a cusp in the central $\sim$ 300 pc of a much smaller galaxy at high redshift ($\sim 10^9$ $M_{\odot}$ at z=6) in a SPH cosmological simulation. In their case, the mechanism that removes the cusp is gravitational heating from large fluctuations in the gravitational field. These fluctuations are produced by bulk motions of gas clumps driven by stellar feedback (Mashchenko et al., 2006). These motions remove episodically 90% of the mass from the central 100 pc after each burst of star formation.

However, these gas clumps can be overproduced in simulations if the local

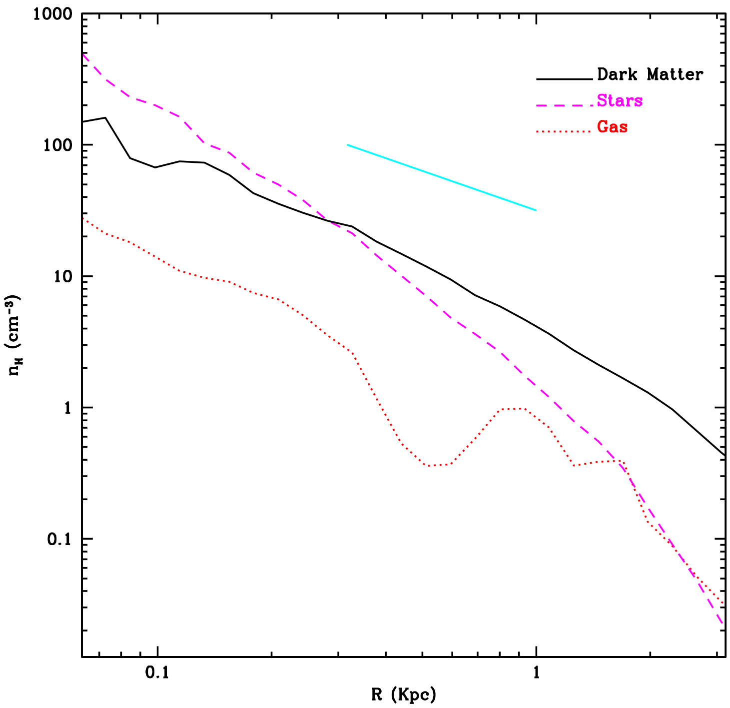

Figure 9.7 Density profile of a galactic halo at redshift 5. The dark matter distribution is consistent with a cusp. The diagonal line shows a slope of -1.

Jeans length is not resolved (Truelove et al., 1997). This produces an artificial gas fragmentation and big clumps of stars. An excessive clumpiness can artificially increase the efficiency of this gravitational heating. In our simulations, we prevent this artificial fragmentation by the implementation of a pressure floor that increases the effective Jeans length at the resolution limit (Robertson & Kravtsov, 2007). However, a direct comparison between our results and Mashchenko et al. (2007) is difficult because we follow the formation of a much bigger galaxy ($\sim 10^{10}$ $M_\odot$ at z=5), in which the effect of this gravitational heating driven by stellar feedback is less important. Therefore, the gravitational heating driven by stellar feedback can not be ruled out in low-mass and gas-rich starburst galaxies.

9.5 Summary and Conclusions

We study the role of supernova explosions and stellar winds in the formation of galaxies. Our approach is to model these processes without the ad-hoc assumptions typically used on stellar feedback. Unlike many currently used prescriptions, we *do not stop cooling* in regions where the energy from stellar feedback is released (Thacker & Couchman, 2000; Brook et al., 2004; Kereš et al., 2005; Governato et al., 2007). Moreover, instead of using a sub-resolution model of a multi-phase medium (Springel & Hernquist, 2003; Cox et al., 2006), we *resolve* that multi-phase medium. This is a more straightforward way to model stellar feedback. It eliminates many ad-hoc assumptions. This approach also produces naturally the outcomes usually associated to stellar feedback: hot bubbles, chimneys and galactic winds.

In our simulations, star formation proceeds in a way consistent with observations of star-forming galaxies (Gao & Solomon, 2004; Kennicutt, 1998). We find a moderate galaxy star formation rate, SFR = 10 $M_\odot$ yr^{-1}, and a significant amount of cold and dense star-forming gas, $M_{\rm dense\,gas} = 10^9\,M_\odot$ inside a 5 Kpc star-forming disk at redshift 3. These values are consistent with observations of nearby starburst galaxies. Using the observed relation between the star formation rate and the amount of star-forming gas of Gao & Solomon (2004), the star formation rate expected for 10^9 $M_\odot$ of cold and dense gas is 20 $M_\odot$ yr^{-1}. This is close to the value found in our simulations. Moreover, the galactic gas consumption time-scale of dense gas, $M_{\rm dense\,gas}/{\rm SFR}$ is ~ 100 Myr. This is consistent with observed values in local starburst galaxies which are usually used as analogs of star-forming galaxies at high redshift (Kennicutt, 1998). From the numbers given above, the gas surface density of the star-forming disk of 5 Kpc radius at redshift 3 is $\Sigma_{\rm gas} = 13$ $M_\odot$ pc^{-2}. Using the Kennicutt fit for nearby star-forming galaxies (Kennicutt, 1998), the expected value for the star formation rate surface density is $\Sigma_{\rm SFR} = 10^{-2}\,M_\odot\ {\rm yr^{-1}\,Kpc^{-2}}$. The measured value from the simulations is $\Sigma_{\rm SFR} = 1.3\times10^{-1}\,M_\odot\ {\rm yr^{-1}\,Kpc^{-2}}$. Although this value is an order of magnitude higher than the expected value from the fit, it is still within the intrinsic spread found in observations. As a result, our simulated high-redshift galaxy seems more compact than the average star-forming galaxy at low-redshift.

Our cosmological simulations with this model of stellar feedback do not have the overcooling problem. The fraction of cold baryons (stars and gas with a temperature bellow 10^4 K) inside the virial radius at z=5 is 0.6 times the cosmological value (f_{cosmo}=0.15). This is consistent with galaxy mass models (Klypin et al., 2002). Instead of a cold disk, we produce a multi-phase ISM with the same features seen in the simulations of the ISM described in section 8: cold clouds, hot super-bubbles and galactic chimneys. The angular momentum problem is also reduced. Instead of a compact object with a strong peak in the rotation curve, we produce more extended galaxies with nearly flat rotation curves. Baryons are less concentrated when stellar feedback plays a role in the formation of galaxies. At the same time, the density profile of dark matter is still consistent with a cuspy profile.

In this picture, galactic chimneys powered by stellar feedback combine into a galactic wind. So, galactic winds appear as the natural outcome of stellar feedback in starburst galaxies at high redshifts. We found typical outflow velocities of 300 km s^{-1} with some exceptional examples of outflows exceeding 1000-2000 km s^{-1}. This is consistent with observation of outflows at high redshift (Law et al., 2007). From a sample of $\approx$ 100 galaxies at redshift $1.9 < z < 2.6$, Steidel et al. (2008) find a mean outflow velocity of 445 km s^{-1}. Some cases have velocities of 1000 km s^{-1}.

This picture is only reproduced if the resolution is high enough to resolve the physical conditions of densities and temperatures of molecular clouds. Our cosmological simulations reach a resolution of 35 pc, which is 10 times better than the typical resolution in previous cosmological simulations (Sommer-Larsen et al., 2003; Abadi et al., 2003; Robertson et al., 2004; Brook et al., 2004; Okamoto et al., 2005; Governato et al., 2007).

10 GALAXY EVOLUTION AT LOW REDSHIFTS

Up to this point, I have only discussed results of galaxy formation up to redshift $z \sim 3$, 2 Gyr after the Big Bang. This is roughly the period when the first cosmic structures and protogalaxies formed. However, this is only a $\sim 1/6$ of the age of the Universe. The problem is that a maximum proper resolution of ~ 30 pc at lower redshifts is computationally too expensive. Basically, the comoving resolution is fixed. As a result, the proper resolution decreases for lower redshifts: $400 \times (1+z)^{-1}$ pc. This has the effect of decreasing the efficiency of thermal feedback, as discussed in §5. In this section I present results at lower redshifts in order to explore the different regimes for galaxy formation up to redshift $z \sim 0.16$ (11.4 Gyr after the Big Bang). This is roughly 4/5 of the age of the Universe ($t_U = 13.5$ Gyr).

Figure 10.1 shows the evolution of the MW-type galaxy as the Universe evolves. These slices show gas temperature at redshifts $z = 2.5, 1.5, 0.8$ at a fixed size of 100 proper Kpc. At redshift $z = 2.5$, a galactic disk is barely seen. The protogalaxy is very small: a few Kpc. The galactic halo, surrounding the protogalaxy, is also small. It has a mass of $2 \times 10^{11} \mathrm{M}_\odot$, mostly dark matter, and a virial radius of 50 Kpc. The main features at this scale are flows of cold ($T \sim 10^4$ K) gas. They can be seen as narrow cold filaments which are coming from Mpc distances and reach the center of the halo. This is the cold mode of accretion, which dominates the gas accretion in low-mass galaxies (Kereš et al., 2005; Birnboim & Dekel, 2003; Dekel & Birnboim , 2006). Halos of this mass can not hold an accretion shock that would heat the gas to high temperatures (Birnboim & Dekel, 2003). As a result, the gas accreted into the galaxy is coming from these cold flows (Kereš et al., 2005).

The opposite regime, the hot mode of accretion, is typical in massive galaxies that build a massive and virialized hot corona. As a result, an accretion shock heats the gas at roughly the virial radius and the galaxy grows by the accretion of hot gas that "rains down" to the disk (Kaufmann et al., 2006). At redshift $z = 1.5$ the halo is in an intermediate regime between the hot and the cold accretion. The halo is more massive: 4×10^{11} $\mathrm{M}_\odot$ inside a virial radius of 100 Kpc. As the halo grows, the cold flows are moving out. This enables the formation of an extended disk. A disk of cold gas can be seen edge-on at z=1.5. At the same time, the halo of hot gas is more prominent than before. Finally, at redshift, $z = 0.8$, the cold flows have been broken into a set of infalling clouds and the hot gas dominates the halo. At this moment, the halo has 10^{12} $\mathrm{M}_\odot$ inside a virial radius of 200 Kpc. The galaxy settles into the hot mode of accretion.

Figure 10.2 shows slices of density and temperature of the galaxy at $z = 0.8$. The temperature plot is the same as in figure 10.1 but the color palette is different.

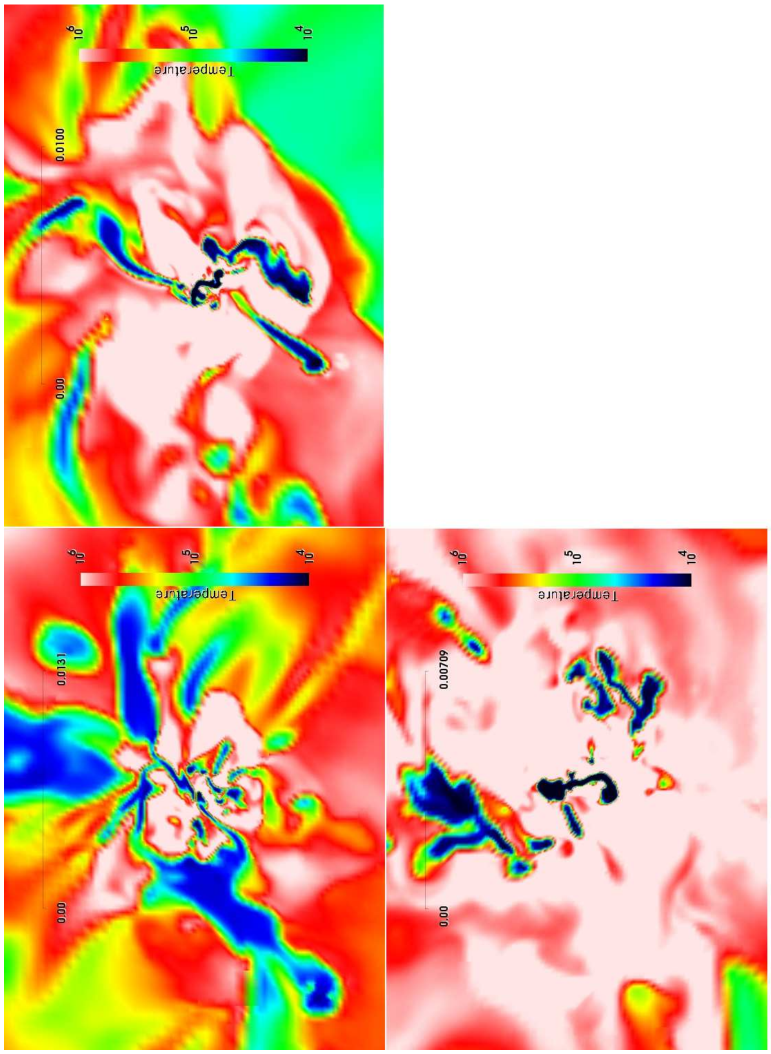

Figure 10.1 Temperature distribution of the galaxy at redshift 2.5 (bottom-left), redshift 1.5 (top-left) and redshift 0.8 (bottom-right). The size is always 100 proper Kpc at any redshift.

It clearly shows a thin gaseous disk, seen edge-on, with a radius of roughly 4 Kpc. At the same time, the halo has a population of cold clouds which resemble the population of high velocity clouds in our galaxy. These cold clouds are embedded in a hot gas corona. However, the importance of these cold clouds in the late accretion of gas is not clear. How massive are they? Are they forming from the hot halo due to thermal instabilities (Kaufmann et al., 2006) or are they coming from cosmological distances and somehow survive the accretion shock? Only future analysis will clarify these issues.

In the same figure 10.2 the stellar disk is overplotted. These are stars younger than 2 Gyr. They form an extended stellar disk. Figure 10.3 shows the edge-on and face-on views of the young stellar disk and the edge-on view of the whole stellar component. We conclude that an inner stellar disk of 4 Kpc is already in place at redshift $z \sim 1$. it is formed by the late accretion of gas in the hot accretion mode. On the other hand, the old stellar population forms a spheroidal component. This population was created at early times, when the cold flows and mergers dominate the accretion of material into the protogalaxy.

Extended galactic disks are formed at these late stages of galaxy formation. Figure 10.4 shows two examples of spiral galaxies at $z = 0.6$. The size of both disks is roughly 20 Kpc. In both cases, the gas distribution shows a pattern of spiral arms, typical for these types of low-mass spiral galaxies.

As a final result of our numerical models, the metals originally ejected in supernovae enriches the galactic outflows. As a result, after several Gyr of evolution, a significant amount of metals has reached cosmological distances. Figure 10.5 shows an example of a slice of 3 Mpc of a side centered in the main galaxy of the simulations. We conclude that SN-driven outflows can be responsible for the metal enrichment of the intergalactic medium.

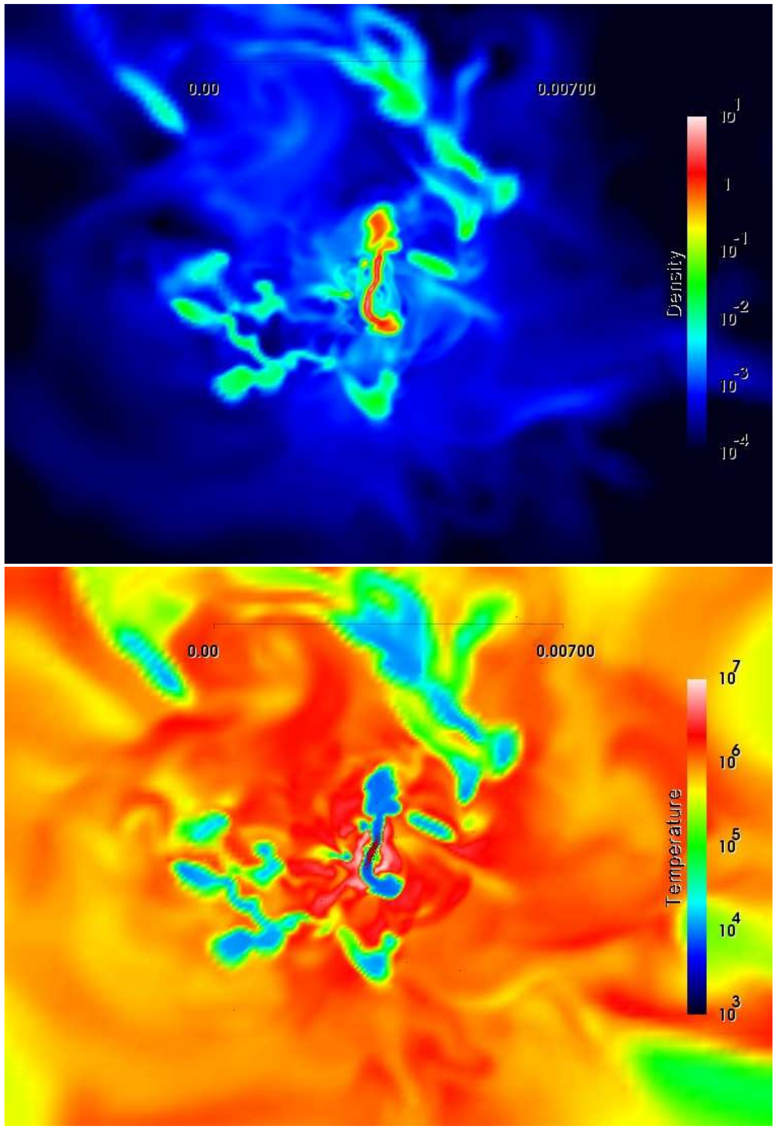

Figure 10.2 Edge-on slices of a galaxy at $z = 0.8$ showing gas density (top) and temperature (bottom). The size in both cases is 100 proper Kpc. A gas disk of 4 Kpc radius is seen edge-on, as well as, an approximately symmetric distribution of cold and dense clouds embedded in a hot gas corona. Young stars are overplotted as points in the temperature plot. They form an extended stellar disk.

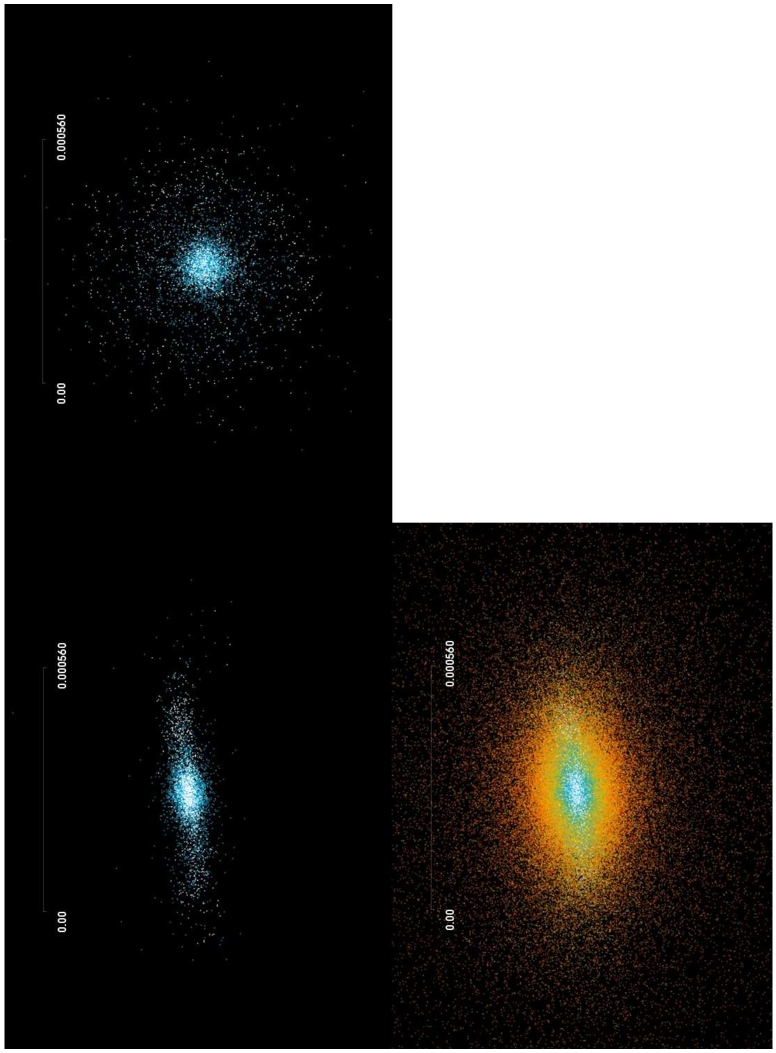

Figure 10.3 Stellar distribution of the system at redshift 1. Top panels show the edge-on view (bottom-left) and face-on view (top-left) of stellar particles younger than 2 Gyr. The bottom-right panel shows all the stellar populations. Blue and white points are stellar particles younger than 2 Gyr and yellow or red are older populations. The size of all panels is 8 proper Kpc.

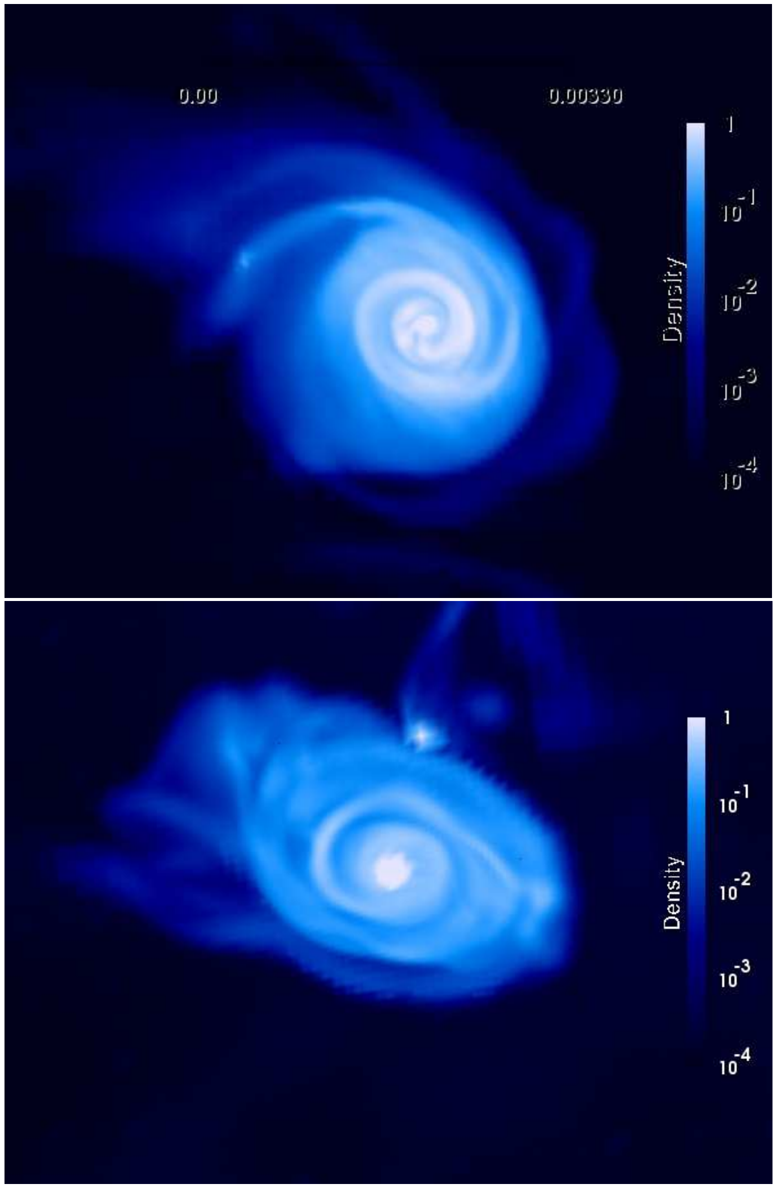

Figure 10.4 Two different low-mass spiral galaxies, progenitors of a MW-size galaxy at redshift $z = 0.6$. Only the gas density is shown. The size of these galactic disks is roughly 20 Kpc.

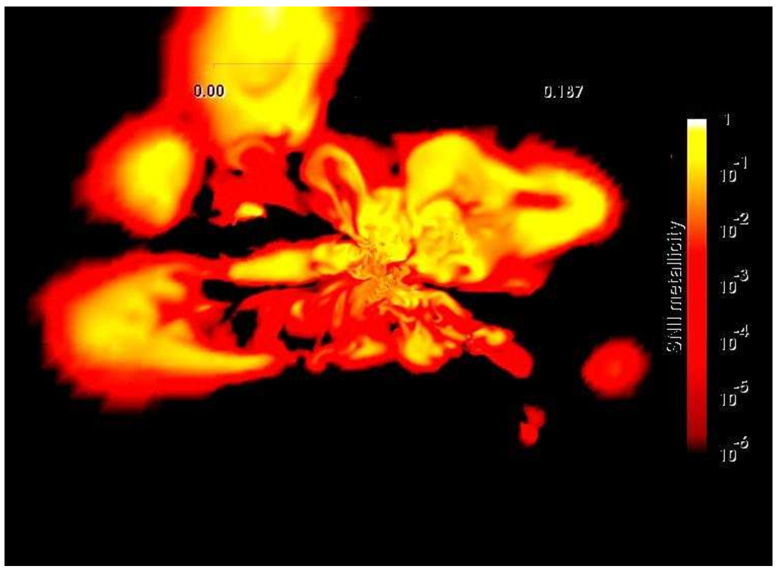

Figure 10.5 Slice at $z = 0.8$ showing metals originally ejected in core-collapsed supernovae in units of solar abundance. The size is 3 Mpc. SN-driven galactic outflows can release a significant amount of metals into the intergalactic medium.

11 SECULAR EVOLUTION IN GALACTIC DISKS: The Role of Resonances

The contents of this chapter were published in the paper: *Resonances in Barred Galaxies*, Ceverino, D., & Klypin, A. 2007, *MNRAS*, 379, 1155.

We can now distinguish the processes that drive the evolution of galactic disks from the processes of disk formation. This is just a simplification because in reality galaxy formation is an ongoing process. However, after a violent epoch of mass assembly into galaxies, the process continues with a slower rate. In this quiescent evolution, slow physical processes start to play a role. This slow evolution is usually called secular evolution. The time scales of these processes are much longer than the dynamical time scale of the system (Kormendy & Kennicutt, 2004) The secular processes relevant for galaxy evolution are the interactions of stars and gas with collective structures, such as bars, spiral arms or triaxial dark matter halos and the interactions between them. Among these processes, secular evolution driven by bars and ovals distortions is the most important component because the forces involved are stronger than in other non-axisymetric features.

11.1 Introduction

It is often assumed that the stellar disk in spiral galaxies can be modeled as an axisymmetric system. Departures from this symmetry are usually treated as weak non-axisymmetric perturbations, like spiral arms (Binney & Tremaine, 1987). However, many spiral galaxies show strong non-axisymmetric features such as central bars. In fact, galaxies with strong bars are very common objects in the Universe. They account for 65 per cent of bright spiral galaxies (Eskridge et al., 2000). Barred galaxies can not be modeled as nearly axisymmetric systems because the dynamics of these galaxies is dominated by a strong bar which rotates around the center. The bar interacts with galactic material and distorts galactic orbits. In particular, some galactic orbits experience dynamical resonances with the bar. The motion in these orbits is coupled with the rotation of the bar: resonant orbits are closed orbits in the reference frame which rotates with the bar. In this frame, the bar is stationary and a resonant orbit can periodically reach the same position with respect to the bar. A resonant orbit is therefore a periodic orbit in this reference frame and its dynamical frequencies are commensurable (Lichtenberg & Lieberman, 1983).

The motion of a star in a galaxy could be described by oscillations in three dimensions: radial oscillation, an oscillation perpendicular to the galactic plane, and an angular oscillation or rotation around the galactic center. In general, these oscillations could be described by three instantaneous orbital frequencies: a radial frequency κ, a vertical frequency ν and angular frequency Ω. The case of a nearly circular orbit in an axisymmetric potential is especially easy to understand and to study analytically using the epicycle approximation (Binney & Tremaine, 1987). However, a general orbit in the gravitational potential of a galaxy is not a nearly circular orbit. This is especially true for barred galaxies where the radial oscillations are not small and orbits can be very elongated. In barred galaxies orbital frequencies may differ significantly from the frequencies in the epicycle approximation.

A resonance happens if the dynamical frequencies of an orbit and the angular frequency of the rotation of the bar, Ω_B, satisfy the following relationship of commensurability:

$$\mathbf{l} \cdot \mathbf{\Omega} = m_B \Omega_B \tag{11.1}$$

where $\mathbf{l}$=(l, m, n) is a vector of integers, $\mathbf{\Omega}$ is a vector of frequencies, $\mathbf{\Omega} = (\kappa, \Omega, \nu)$ and m_B is also a integer. We mostly will be interested in cases with $m_B = m$ and in motions close to the galactic plane: $n = 0$. So, the resonant condition is reduced to

$$l\kappa + m(\Omega - \Omega_B) = 0 \tag{11.2}$$

Thus, each planar resonance is described by a pair of integers, $(l{:}m)$. A resonant $(l{:}m)$ orbit is closed after l revolutions around the center and m radial oscillations in the reference frame which rotates with the bar. Table 11.1 summarizes several examples of these resonances.

One important example is the corotation resonance (CR), $\Omega = \Omega_B$. A star in a resonant orbit of CR rotates around the galaxy center with a speed equal to the rotation speed of the bar. Thus, it does not move in the rotating frame. Other important resonances are the inner and outer Lindblad resonances. As it seems from the rotating frame, a star in one of these resonant orbits makes two radial oscillations during one angular revolution. The resonant orbit has therefore an ellipsoidal shape. The inner Lindblad resonance (ILR) corresponds to the (-1,2) resonance. In this case, the star rotates faster than the bar, $\Omega > \Omega_B$. The opposite case, $\Omega < \Omega_B$, corresponds to the (1:2) resonance, which is the outer Lindblad resonance (OLR).

Significant effort has been made to study motions near resonances in astrophysical systems as well as in plasma physics and in Solar system dynamics (Chirikov, 1960; Lynden-Bell & Kalnajs, 1972; Tremaine & Weinberg, 1984; Weinberg, 2004; Weinberg & Katz, 2007a). One important and difficult problem is that of small divisors or small denominators. Suppose we impose a small perturbation and study the effect of this perturbation. In the case of barred galaxies, the unperturbed case is an axisymmetric model and the perturbation is a weak bar. One may try

Table 11.1 Examples of resonances

Name	l	m	n	$\frac{\Omega-\Omega_B}{\kappa}$
CR	0	1	0	0
ILR	-1	2	0	0.5
OLR	1	2	0	-0.5
UHR	-1	4	0	-0.25

to find a solution to this problem using perturbation series. When this is done, the solution typically has terms with denominator $\mathbf{l} \cdot \mathbf{\Omega} - m_B\Omega_B$, which goes to zero at resonance. The reason for this divergence is the breakdown of the assumption that the solution can be written as a perturbation series. It appears that the correct behavior of the solution cannot be obtained in any order of the perturbation theory (Lichtenberg & Lieberman, 1983, Sec.2.2b). One may think that perturbation theory gives qualitatively correct answer (e.g., predicts large changes in energy and angular momentum), but it fails to estimate the magnitude of the effect. Unfortunately, this is not the case: it gives wrong qualitative answers. Binney & Tremaine (1987, Chapter 3, eqs. (3-123)-(3-129)) give an example of treatment of orbits around a stable corotation resonance (Lagrange points L_4 and L_5). In this case the perturbation expansion gives a divergent amplitude (the solution linearly grows) and the correct treatment in Binney & Tremaine (1987) does not show *any* growth (see also Byrd, Freeman & Buta).

It is important to formulate the situation clearly because this can produce significant confusion. In mathematics the problem is often stated as the problem of perturbations: how orbits change when a perturbation is imposed. In this case one compares perturbed orbits with the same orbits before the perturbation was imposed. Significant deviations are expected to happen for unperturbed trajectories in regions of overlapping resonances of the unperturbed system (Chirikov, 1960). But this is not the problem which we deal with in barred galaxies. In this case we study only perturbed orbits: how they change with time and how they behave close to resonances of the perturbed system. In other words, we do not compare perturbed orbits with the unperturbed trajectories. By itself it is a very interesting problem: formation of bars. At this time we focus exclusively on the evolution under the forces of bars.

This is significantly easier problem. We also simplify the situation by considering bars which do not change with time. First, we start with orbits at exact resonances: $\vec{l} \cdot \vec{\Omega} = m_B \Omega_B$. How do they evolve? The answer is simple: they do not (Lynden-Bell & Kalnajs, 1972). Orbits at exact resonances are closed in the phase-space: after some time they come to exactly the same position in space and have exactly the same velocities. Thus, they have the same angular momentum and the same energy.

Close to the resonances the situation is complex. Lynden-Bell & Kalnajs (1972) argued that there should be significant growth of perturbations in this area. Yet, this argument was based on the perturbation expansion, which is not valid near resonances. We distinguish two types of resonances: elliptic and hyperbolic (Arnold & Avez, 1968). Lagrange points L_4 and L_5 are examples of elliptic resonances: orbits oscillate and librate around those resonances and have the structure of a simple pendulum (Lichtenberg & Lieberman 1983, Sec. 2.4, Murray & Dermott 1999, Sec. 8). Hyperbolic resonances are points on the intersection of separatrixes dividing domains of elliptical resonances (e.g., Lagrange points L_1 and L_2). In this paper we are mostly interested in elliptical resonances.

There is no evolution at resonant orbits for a stationary perturbation and there are no singularities at resonances. Therefore, the small divisor problem can lead to a wrong interpretation of the secular evolution near resonances and their role in barred galaxies. A more careful treatment of the motions in near-resonant orbits reveals that the Hamiltonian near a resonance can be approximated by the Hamiltonian of the one dimensional pendulum in a variable which change slowly near the resonance (Lichtenberg & Lieberman, 1983). So, the motions near every resonance can be approximated by motions of libration, separatrix and rotation around a resonant orbit. Examples of these motions near CR and ILR can be found in section 11.9. Circulating pendulum solutions near CR are also given by Byrd (Freeman & Buta). In general, each fixed point of the pendulum corresponds to an exactly resonant orbit. As the result, each resonance has formally two different types of resonant orbits. One corresponds to the stable or elliptic fixed point, around which the near-resonant orbits librate. The other corresponds to the unstable or hyperbolic fixed point, where the separatrices intersect. In the region around the separatrix, this pendulum approximation fails. The phase-space near the separatrix is more complex that in the case of a pendulum (Voglis, Tsoutsis & Efthymiopoulos). This area may be filled with irregular or chaotic orbits and high-order resonances ($l > 1$). This is usually called the resonance layer (Lichtenberg & Lieberman, 1983). As a result of all this complexity, perturbation theory is not valid at any order near resonances. Small divisors can be removed from one order in the perturbation series, but other small divisors appear in a higher order. So, the right behavior near resonances can only be studied by solving for the exact solution of the equations of motions near resonances.

The phase-space near resonances is mainly populated by trapped orbits in libration around stable resonant orbits. Their exact trajectories are commonly computed in orbit theory (Contopoulos & Grosbøl, 1989; Skokøs et al., 2002). In this field, the potential of a barred galaxy is modeled by a combination of different analytical potentials, like an axisymmetric disk plus a prolate ellipsoid. Then, galactic orbits are computed numerically using this galactic model. In this way, the galactic orbital structure can be studied in detail. Resonant orbits in this case are periodic orbits in a given non-axisymmetric potential. Each stable periodic orbit is the parent of a family of non-closed orbits which remain near to this orbit at any moment (Binney & Tremaine, 1987). The dynamical frequencies of these trapped orbits oscillate around the frequencies of the resonant orbit. Therefore, their average frequencies over time should be close to the frequencies of the resonant or parent orbit.

However, orbit studies have some limitations. They can not follow the self-consistent evolution of barred galaxies. The underlying potential is fixed and does not change due to the redistribution of the orbits. In contrast, N-body models can follow the orbits and the secular evolution of barred galaxies at the same time. However, Weinberg & Katz (2007a) have derived the necessary number of particles in an N-body model which could accurately resolve the dynamics near resonances. These required numbers are well beyond the numbers used in current state-of-the-art models. So, do we have any hope to see the effects of resonances in N-body models? We argue that current N-body models can resolve the dynamics of resonances in the regime relevant for observed barred galaxies. They have strong non-axisymmetric features. In contrast, the particle number criteria of Weinberg & Katz (2007a) were derived in the regime of weak perturbations.

N-body models have been already used to study the resonant interaction between the bar and the halo of dark matter (Holley-Bockelmann et al., 2005; Colín et al., 2006; Athanassoula, 2002, 2003; Martinez-Valpuesta et al., 2006; Weinberg & Katz, 2007b). N-body models open the possibility to sample individual trajectories over time and extract their dynamical frequencies. This allows a better determination of resonant orbits and their dynamics. This has been done in restricted N-body experiments with a frozen non-axisymmetric potential (Holley-Bockelmann et al., 2001; Athanassoula, 2002, 2003; Martinez-Valpuesta et al., 2006). In Athanassoula (2002), the orbital frequencies were estimated using a random population of particles taken from the disk and the halo of a N-body simulation. A frozen barred potential equal to the potential of the simulation was set to rotate with the pattern speed measured in the simulation at a given moment. Each orbit was computed in this stationary potential. Finally, the dynamical frequencies of each orbit were estimated using a spectral analysis. Some of the orbits were trapped near resonant orbits in the disk and in the halo. The slowdown of the bar was linked to the loss of angular momentum of nearly resonant orbits in the inner disk. At the same time, the gain of angular momentum of the halo was linked to the gain of angular momentum of near-resonant orbits in the halo.

However, little work has been published on the detection of resonances in a fully self-consistent N-body model of a barred galaxy. The purpose of this study was to detect and characterize the resonances present in barred galaxies. This study may also find new insights into the dynamics near resonances and their role in barred galaxies. This section is organized as follows. §11.2 - §11.4 present the N-body models analyzed in this paper. §11.5 describes the methods used to measure the dynamical frequencies of the particles. §11.6 - §11.7 describe the main results of resonances in the disk and in the halo. §11.8 describes the capture at corotation as an example of resonant capture. §11.9 - §11.10 compare these results with an analytical galactic model. Finally, §11.11 is devoted to the discussion and §11.12 is the summary and conclusion.

11.2 Initial Conditions

The initial conditions of the N-body models are described in detail in Valenzuela & Klypin (2003). The generation of the models follows the method of Hernquist (1993). The model initially has only a stellar exponential disk and a dark matter halo. No bar is initially present in the model but the system is unstable and forms a bar. The density of the stellar disk in cylindrical coordinates is approximated by the following expression:

$$\rho_d(R,z) = \frac{M_d}{4\pi z_0 R_d^2} e^{-\frac{R}{R_d}} sech^2(z/z_0), \tag{11.3}$$

where z_0 is the scale height of the disk, R_d is the exponential length and M_d is the mass of the disk. The scale height is assumed to be initially constant through the disk. The vertical velocity dispersion σ_z is given by the scale height and the surface stellar density Σ:

$$\sigma_z^2(R) = \pi G z_0 \Sigma(R), \tag{11.4}$$

where G is the gravitational constant. The radial velocity dispersion σ_R is also related to the surface density:

$$\sigma_R(R) = Q\frac{3.36 G\Sigma(R)}{\kappa(R)}, \tag{11.5}$$

where $\kappa(R)$ is the epicycle frequency at a given radius and Q is the Toomre stability parameter, assumed constant through the disk. The rotational velocity

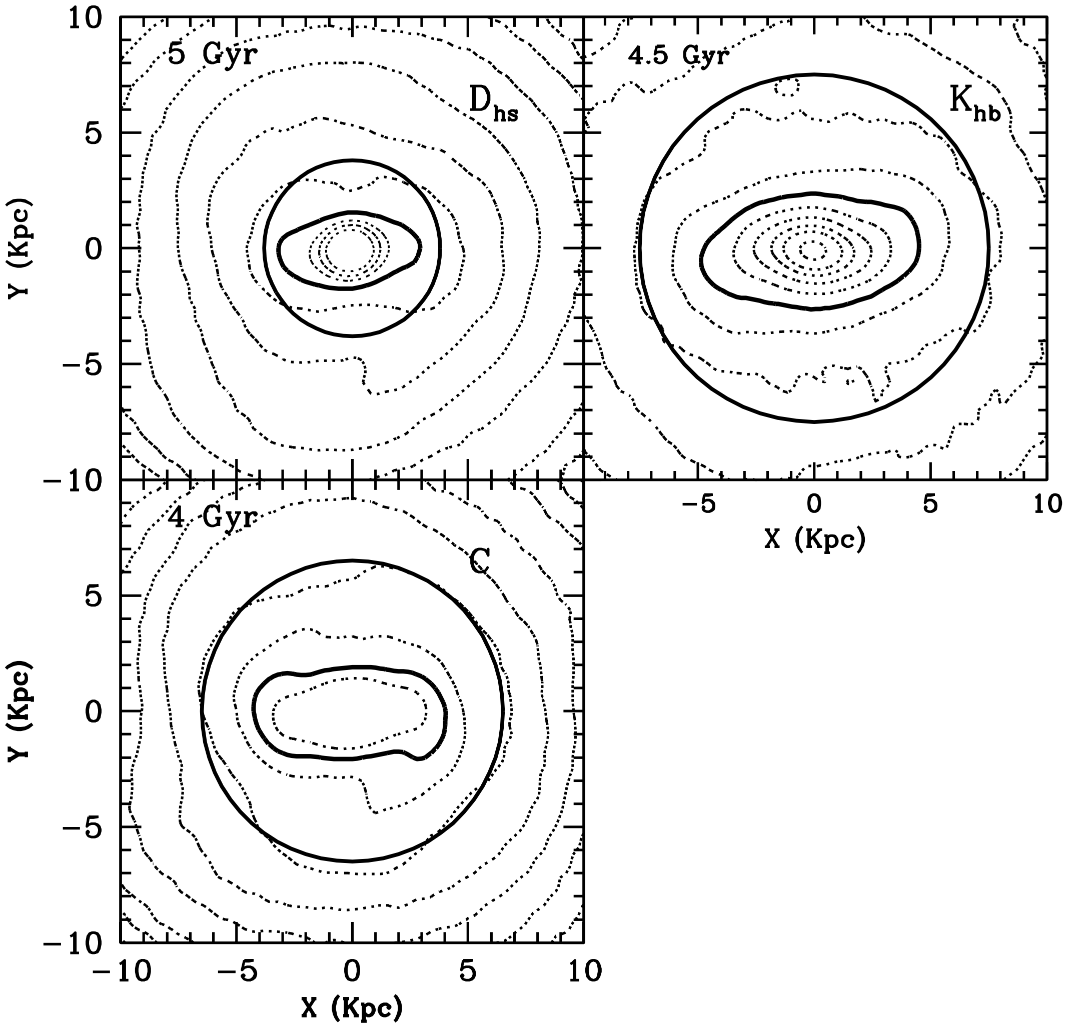

Figure 11.1 Face-on views of the three N-body models of barred galaxies. The contours show levels of equal surface density. Their scale is logarithmic with a step of 0.5 dex. The scale is the same for all figures. The circles represent the corotation radius for each model. The model K_{hb} develops a larger and slower bar than the model D_{hs}. The model C has a strong and massive bar.

Table 11.2 Initial parameters of models

Parameter	D_{hs}	K_{hb}	C
Disk Mass (10^{10}M$_\odot$)	5.0	5.0	4.8
Total Mass (10^{12}M$_\odot$)	1.43	1.43	1.0
Disk exponential length (kpc)	2.57	3.86	2.9
Disk exponential height (kpc)	0.20	0.20	0.14
Stability parameter Q	1.8	1.8	1.2
Halo concentration C	17	10	19
Total number of particles (10^5)	38.0	27.2	97.7
Number of disk particles (10^5)	4.60	2.33	12.9
Particle mass (10^5M$_\odot$)	1.07	2.14	0.37
Maximum resolution (pc)	22	22	100.
Time Step ($10^4 yrs$)	1.48	0.95	12.

V_ϕ and its dispersion σ_ϕ are computed using the asymmetric drift approximation and the epicycle approximation,

$$V_\phi^2(R) = V_c^2(R) - \sigma_R^2(R)\left(\frac{2R}{R_d} + \frac{\kappa^2(R)}{4\Omega^2(R)} - 1\right), \tag{11.6}$$

$$\sigma_\phi^2(R) = \sigma_R^2(R)\frac{\kappa^2(R)}{4\Omega^2(R)}, \tag{11.7}$$

where V_c is the circular velocity at a given radius and Ω is the angular frequency in the epicycle approximation.

The density profile of a cosmological motivated dark matter halo is initially well approximated by the NFW profile (Navarro et al., 1997),

$$\rho_{\rm dm}(r) = \frac{\rho_s}{x(1+x)^2},\ x = r/r_s, \tag{11.8}$$

$$M_{\rm vir} = 4\pi\rho_s r_s^3\left[\ln(1+C) - \frac{C}{1+C}\right],\ C = \frac{r_{\rm vir}}{r_s}, \tag{11.9}$$

where $M_{\rm vir}$ and C are the virial mass and the concentration of the halo. The radial velocity dispersion of dark matter particles is related with the mass profile of the system, M(R),

$$\sigma_{R,\rm dm}^2 = \frac{1}{\rho_{\rm dm}}\int_R^\infty \rho_{\rm dm}\frac{GM(R)}{R^2}dR. \tag{11.10}$$

Finally, the other two components of the velocity dispersion of dark matter are equal to $\sigma_{r,\rm dm}^2$, assuming an isotropic velocity distribution. This assumption remains valid in the central parts of dark matter halos (Colín et al., 2000).

11.3 Description of the Models

We analyze two of the N-body models of barred galaxies described in Colín et al. (2006). We also include the model C of Valenzuela & Klypin (2003). These three models are consistent with normal high surface brightness galaxies. The dark matter does not dominate in the models in the first two scale lengths, $R \leq 2R_d$ (Klypin et al., 2002). The parameters of the models are presented in Table 11.2. These models do not cover a large range of parameters. This is done in Colín et al. (2006). Instead, we have selected three models with very different initial conditions. D_{hs} has a more concentrated halo and a shorter disk length than K_{hb}. For example, the dark matter contribution to the initial circular velocity is equal to the contribution of the disk at 7 Kpc in the model D_{hs} and 10 Kpc in the model K_{hb}. As a result, D_{hs} is initially more centrally concentrated than K_{hb}. The disk is hot, $Q \approx 1.8$, in these two models. In contrast, the model C has a cold disk, $Q \approx 1.2$. In addition, the halo of this model has a higher concentration than the models from Colín et al. (2006) but its exponential length is in between the values of the other two models. As a result, 6.5 Kpc is the radius in which the contribution of the halo and the disk to the initial circular velocity are equal. All these differences are reflected in the bar evolution and therefore, they are also reflected in the resonant structure. All three models develop a relatively strong bar (Fig. 11.1). However, the bar in the model D_{hs} is shorter and rotates faster than the bar in the model K_{hb}. This affects strongly the resonant structure. All three models show a slow evolution in the pattern speed of the bar, Ω_B, so it could be considered nearly constant over a period of 1-2 Gyr (Colín et al., 2006). This is a suitable situation for the analysis of resonances because the resonant structure is stable if Ω_B is constant.

11.4 The Code

These simulations were performed with the Adaptive Refinement Tree (ART) N-body code (Kravtsov et al, 1997; Kravtsov, 1999). The code computes the density and gravitational potential in each cell of a uniform grid. If the number of particles in a cell exceeds a given threshold, the cell is split in 8 smaller cells. This creates the next level of a refinement mesh. The procedure is recursive. The result is a refined mesh which accurately matches high density regions with arbitrary geometry. This spatial refinement is followed by a temporal refinement. More refined regions have a shorter time step. This is necessary to follow accurately the trajectory of particles. The code was extensively tested. Additional tests on the long-term stability of equilibrium systems were performed in Valenzuela & Klypin (2003). These tests are important to study the secular evolution in barred galaxies. The results showed that the effect of two-body scattering is negligible. The relaxation time scale was roughly equal to 4.5×10^4 Gyr for a system with 3.5 million particles.

11.5 Measurement of Orbital Frequencies

We measure the orbital frequencies of all particles over a given period of time. This time average is an estimate of the instantaneous orbital frequencies used in the resonant condition (Eq. 11.2). The measurements are done using the trajectories of all particles. In the models K_{hb} and D_{hs}, each trajectory is sampled with

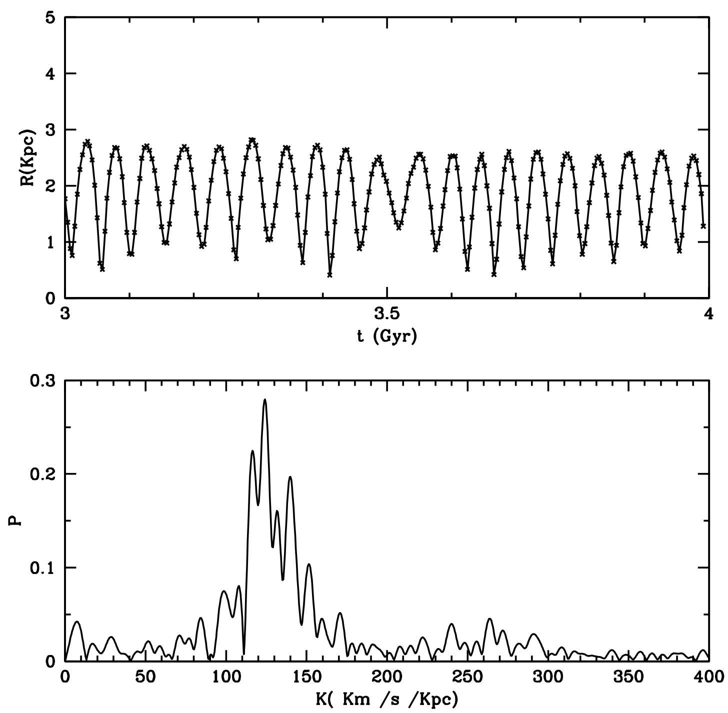

Figure 11.2 Example of a measurement of a radial frequency, κ, of a particle using the Fourier spectrum of its radial oscillations. The top panel shows the radius of a particle as a function of time for K_{hb} and the bottom panel presents the Fourier decomposition of its radial trajectory, where P is the power spectrum. The radial frequency is measured as the maximum peak of the spectrum, $\kappa = 126$ Km s^{-1} Kpc^{-1}.

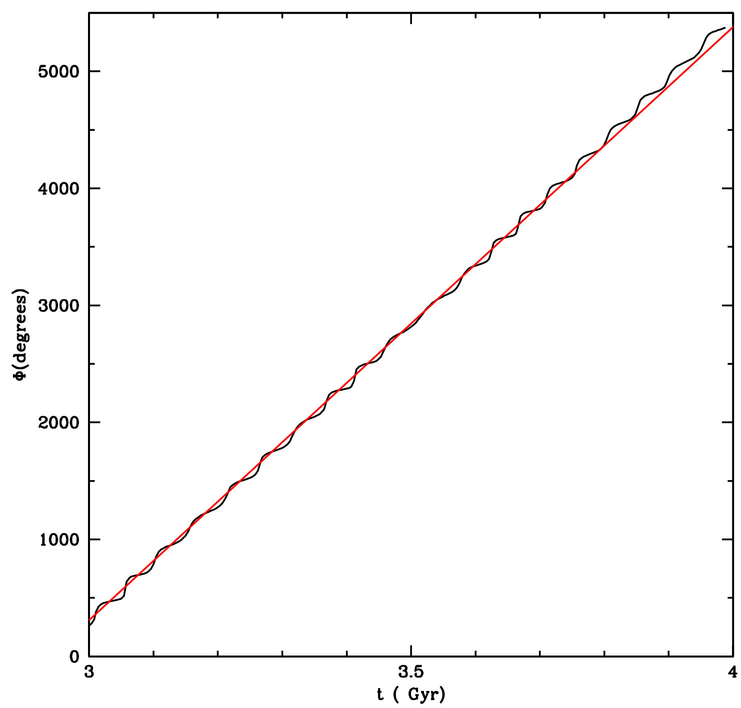

Figure 11.3 Example of a angular frequency measurement of a particle using its angular position along its trajectory. The Figure shows the angular positions over time for a particle selected in K_{hb}. The straight line has a slope equal to the measured angular frequency, $\Omega = 88$ Km s^{-1} Kpc^{-1}.

$N_t = 250$ discrete points per Gyr. Therefore, two consecutive points are separated by 4×10^6 yr. Each trajectory during a single sampling step is integrated with more than 270 time steps. The trajectories are recorded in cylindrical coordinates. The orbital frequencies are estimated by tracking the radius and the azimuthal angle as functions of time.

The radial frequency, κ, is measured from the Fourier analysis of the radial oscillations. Fig. 11.2 shows an example of the radial oscillations for one trajectory. We subtract the average radius from the signal and perform a discrete Fourier analysis. The result is the power spectrum of the orbit (P_k). It is based on the harmonics amplitudes, A_k and B_k, in the Fourier decomposition:

$$A_k = \frac{1}{N_t} \sum_i R_i \cos(\omega_k t_i), B_k = \frac{1}{N_t} \sum_i R_i \sin(\omega_k t_i) \tag{11.11}$$

$$P_k = \sqrt{A_k^2 + B_k^2}. \tag{11.12}$$

where R_i is the value of the radius at a given time t_i and ω_k is a discrete frequency in the Fourier space. We use 1200 discrete frequencies to sample the Fourier space from zero to a maximum frequency of 600 Km s^{-1} Kpc^{-1} for D_{hs}. This maximum frequency is well below the Nyquist frequency. In our case, the Nyquist frequency ($\kappa_N = \pi/\Delta$) is 770 Km s^{-1} Kpc^{-1}, where Δ is the interval of 4×10^6 yr between snapshots. In that way, we avoid aliasing problems that arise close to the Nyquist frequency. The bottom panel of the Fig. 11.2 shows an example of the spectrum of the trajectory. The radial frequency is measured as the frequency of the maximum peak in the Fourier spectrum.

However, the gravitational potential is slowly evolving during the period in which the frequencies are measured. This introduces radial modes of low frequency at the top of the orbital oscillations. As a result, 5 per cent of the particles have radial oscillations modulated by an oscillation of low frequency. For these particles, we need to remove these low frequency modes to be able to extract the orbital oscillations. In order to remove these modes from the signal, we define a low cutoff frequency of 12 Km s^{-1} Kpc^{-1}. If the frequency of the maximum peak of the spectrum is below this cutoff, the corresponding mode is subtracted from the radial oscillation. Then, we repeat the Fourier analysis. The procedure ends when the maximum of the spectrum lies beyond the cutoff frequency or when we remove all the significant peaks of the spectrum. In the last case, we reject the particle because its trajectory does not have significant radial oscillations. However, this technique prevents us from detecting radial frequencies lower than the cutoff frequency. These radial oscillations would correspond to trajectories in the edge of the disk, where the effect of the bar is very small. So, these trajectories are not useful for study resonances.

The spectral analysis used for radial frequencies was proved less reliable for angular frequencies (Athanassoula, 2002). In contrast with radial oscillations, the azimuthal angle does not oscillate around a mean value. The angle sweeps periodically all values between 0 and 2π. As a result, the angular frequency is measured using the average period of the angular revolutions in that interval of time. Each angular period is defined as the time that the particle takes to complete one angular revolution starting from a given point of the trajectory. Fig. 11.3 shows an example of the angular positions of one trajectory and the computed angular frequency.

We performed an orbital frequency analysis of all particles in the three models. The following orbits were rejected from a further study: Retrograde orbits, orbits with radial frequencies higher than a maximum frequency of 600 Km s^{-1} Kpc^{-1} and orbits with no significant radial oscillations ($\kappa \leq 12$ Km s^{-1} Kpc^{-1}). In total, we rejected only 10 per cent of the particles in K_{hb} and 30 per cent of the particles in D_{hs}. The higher fraction in D_{hs} is due to a higher concentration of particles at the center. One half of the rejected particles in D_{hs} have very high frequencies and almost radial orbits. They spend all their time very close to the center, so they are not involved in global motions with the bar. As a result, we selected only particles with well defined orbital frequencies during a given interval of time.

11.6 Detection of the Main Resonances

Once the orbital frequencies are measured in our three models, their main resonances become evident using frequency maps. They are commonly used to study resonances between planetary orbits in the Solar system (Laskar, 1990) and in orbital studies of elliptical galaxies (Holley-Bockelmann et al., 2001). In our case, a frequency map displays angular frequencies along the horizontal axis and radial frequencies in the vertical axis. This is a clear way to display the resonant structure of a model in the space of its orbital frequencies. Each point in this space represents the mean orbital frequencies of an individual particle over a fixed period of time. In a frequency map, all the orbits near a particular resonance lie along a line defined by the resonant condition (Eq. 11.2). Ω_B is computed as the average pattern speed in this period of time (Colín et al., 2006). Any set of integers defines a line in the frequency map. As a result, points along a given resonant line correspond to particles close to the resonance by definition.

Fig. 11.4 shows the frequency map of the model D_{hs} for 1 Gyr. We can clearly see a concentration of particles near resonances. In particular, a narrow line of points is clearly visible along the ILR. This resonance covers a big range of angular and radial frequencies. The concentration of orbits near the CR is also specially strong. These particles are forced by the bar to rotate with the bar pattern speed. Other resonances are also visible. For example, the ultra-harmonic (-1:4) resonance (UHR) can be seen as a small cloud of points which intersects

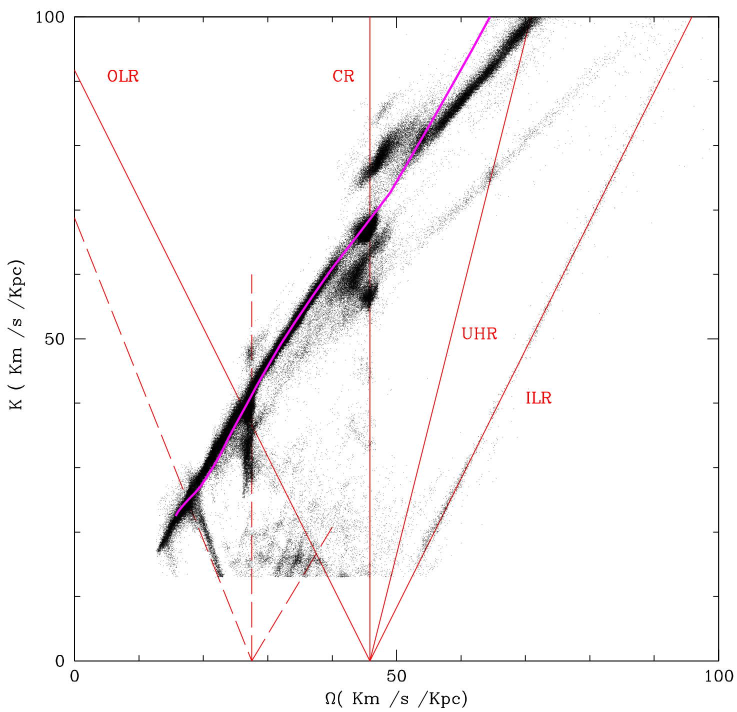

Figure 11.4 Frequency map for D_{hs}. The horizontal axis shows angular frequencies (Ω) and the vertical axis shows radial frequencies (κ). Each point represents the average frequencies of a particle over 1 Gyr. Clustering of points along straight lines with certain slopes indicates the presence of resonances. The lines are computed using the resonant condition (eq. 11.2). Ω_B is computed as the average pattern speed in this period of time. The main resonances are labeled. In addition, the dash lines correspond the CR, ILR and OLR of another non-axisymmetric pattern with a different pattern speed. The grey curve (magenta in the color version) is the result of the epicycle approximation which breaks down inside the corotation radius, where the orbits are very elongated.

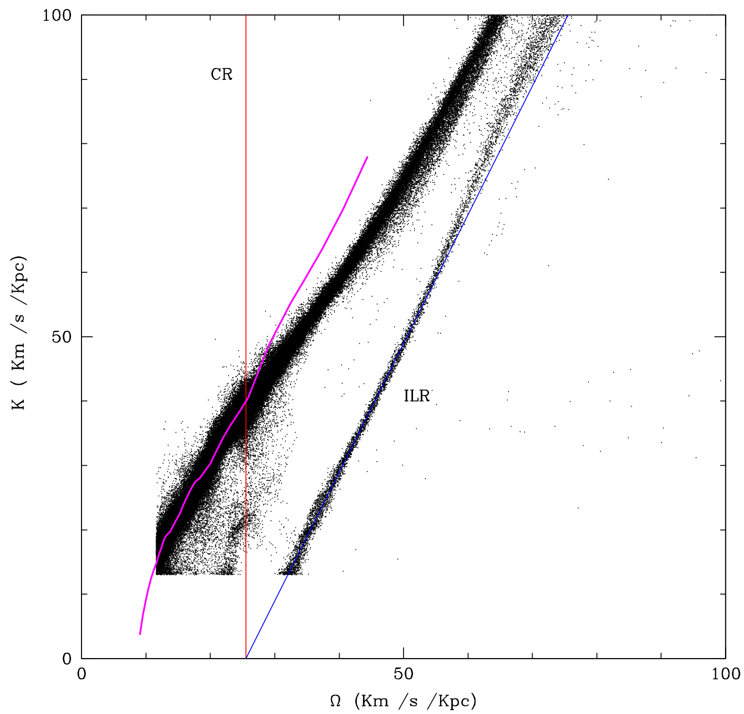

Figure 11.5 Frequency map for K_{hb} (massive bar) for a period of 0.5 Gyr. As in Fig. 11.4, lines indicate the main resonances and the grey curve (magenta in the color version) represents the epicycle approximation. The resonant structure shows a strong clustering of points along the ILR line. This is an indication of a large number of particles trapped near ILR orbits.

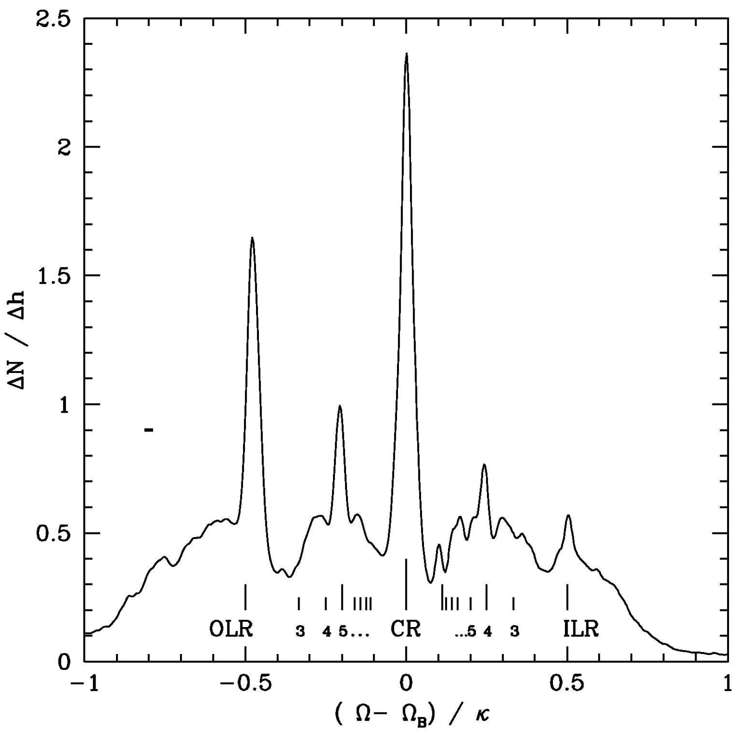

Figure 11.6 Distribution of the ratio $(\Omega - \Omega_B)/\kappa$ for D_{hs} for a period of 1 Gyr. The vertical axis shows the fraction of particles per unit of bin in the frequency ratio. Vertical lines represent low order resonances ($\pm$1:m) and CR. The peaks show a strong indication of trapping resonances. The error-bar at the upper-left corner is the 1σ error using Poisson noise.

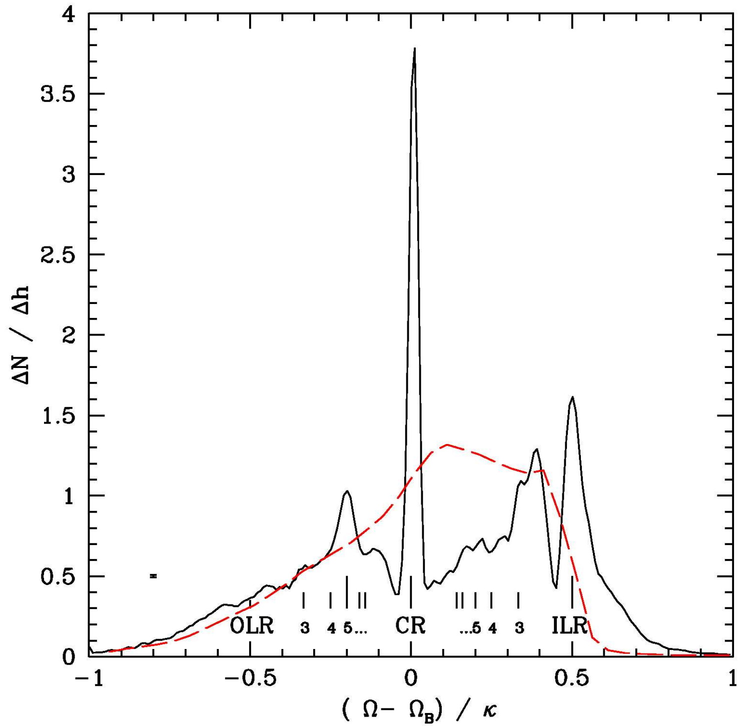

Figure 11.7 Distribution of the ratio $(\Omega - \Omega_B)/\kappa$ for K_{hb} for a period of 2 Gyr. The vertical axis shows the fraction of particles per unit bin in the frequency ratio. The error-bar on the left is the 1σ error using Poisson noise. Strong peaks at CR and ILR are clearly present. The dash line shows the distribution for a period of 0.5 Gyr before the formation of the bar. No peaks are found before the formation of the bar. The formation of these resonant peaks is linked to the capture of particles near resonant orbits.

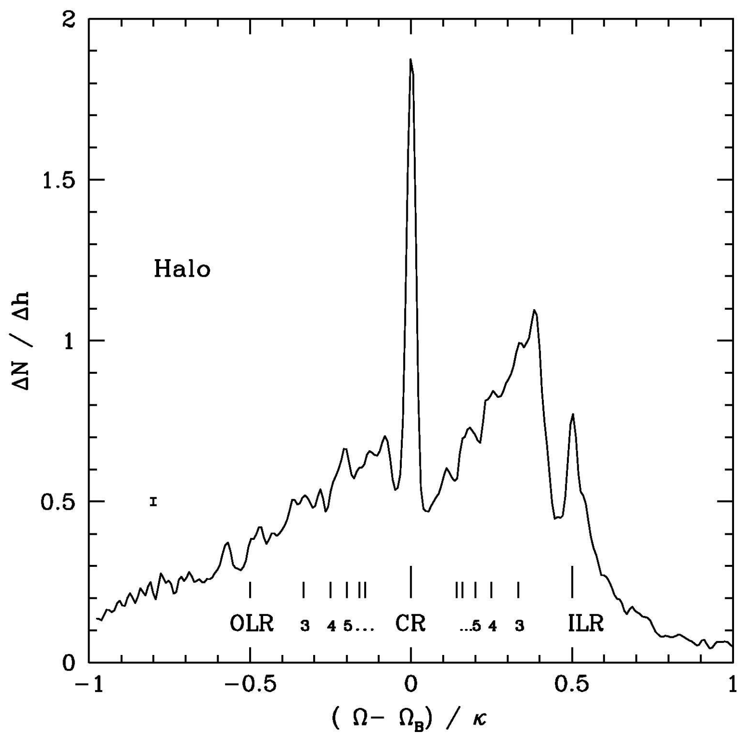

Figure 11.8 Distribution of the ratio $(\Omega - \Omega_B)/\kappa$ for particles in the halo chosen to stay close to the disk of K_{hb}. The lines show resonances as Fig. 11.6 and 11.7. The CR and ILR are clearly present in the halo. The error-bar is the 1σ error using Poisson noise.

the line corresponding to the UHR. The OLR is very prominent. It intersects a line of constant angular frequency, $\Omega = 27$ Km s^{-1} Kpc^{-1}. This may be the CR of another non-axisymmetric pattern. This is supported by the fact that both OLR and ILR are also present for this second pattern. The OLR line is specially well populated. As a result, the model D_{hs} may exhibit an overlap of resonances corresponding to two different non-axisymmetric features.

As another example, Fig. 11.5 shows the frequency map for the model K_{hb} for a period of 0.5 Gyr. This model has a more massive bar which also rotates slower than in the model D_{hs} discussed before. As a result, the resonant structure appears more compressed in this model. Its points extend over a smaller fraction of the frequency space. In addition, the corotation radius is larger. So, resonances beyond corotation, $\Omega < \Omega_B$, extend over the outer disk and they have less available material to capture. Therefore, OLR is not even present in this model. On the other hand, ILR is much stronger. It has more points clustered along the ILR line. This is the effect of a massive bar. The clustering of points near resonant lines in the frequency maps is a signature of trapped particles near resonant orbits.

However, the majority of the points lies on a region spread diagonally across the frequency map. This feature is formed by particles at resonance, as well as particles out of resonance. It can be approximated by the epicycle approximation up to CR. We use the rotation curve of each model to estimate the epicycle frequencies. This approximation deviates from the dynamical frequencies inside the corotation radius. Orbits inside the corotation radius are elongated and their frequencies are higher than the expected values of nearly circular orbits. This is the region dominated by non-circular motions.

It is difficult to identify other resonances which lie on the crowded areas of a frequency map. As a result, we use the distribution of the ratio $(\Omega - \Omega_B)/\kappa$ (Athanassoula, 2002) to detect the resonances of low order in l ($\pm 1 : m$). Each of these resonances has a unique value of this ratio. Fig. 11.6 shows the histogram of $(\Omega - \Omega_B)/\kappa$ for the model D_{hs} for a period of 1 Gyr. The distribution has peaks at the values of different resonances. We found 5 of them: OLR, (1:5), CR, (-1:4) and ILR. Fig. 11.7 shows the distribution of $(\Omega - \Omega_B)/\kappa$ in K_{hb} for a period of 2 Gyr. As we expected from the frequency map, the peak corresponding to the ILR is stronger than in D_{hs}. This is a common feature of systems with large bars.

In these histograms, there is an underlying distribution of particles which do not contribute to any resonant peak. They do not participate in any resonant motion with the bar. Thus, this background of particles should be present even before the formation of the bar. We performed a frequency analysis of the model K_{hb} during the first 0.5 Gyr, before the bar formation. The distribution is shown in Fig. 11.7 as a dashed curve. There are no significant peaks because there is no bar which captures particles near resonant orbits at this early stage of the simulation. As the simulation evolves, the bar forms and the distribution of

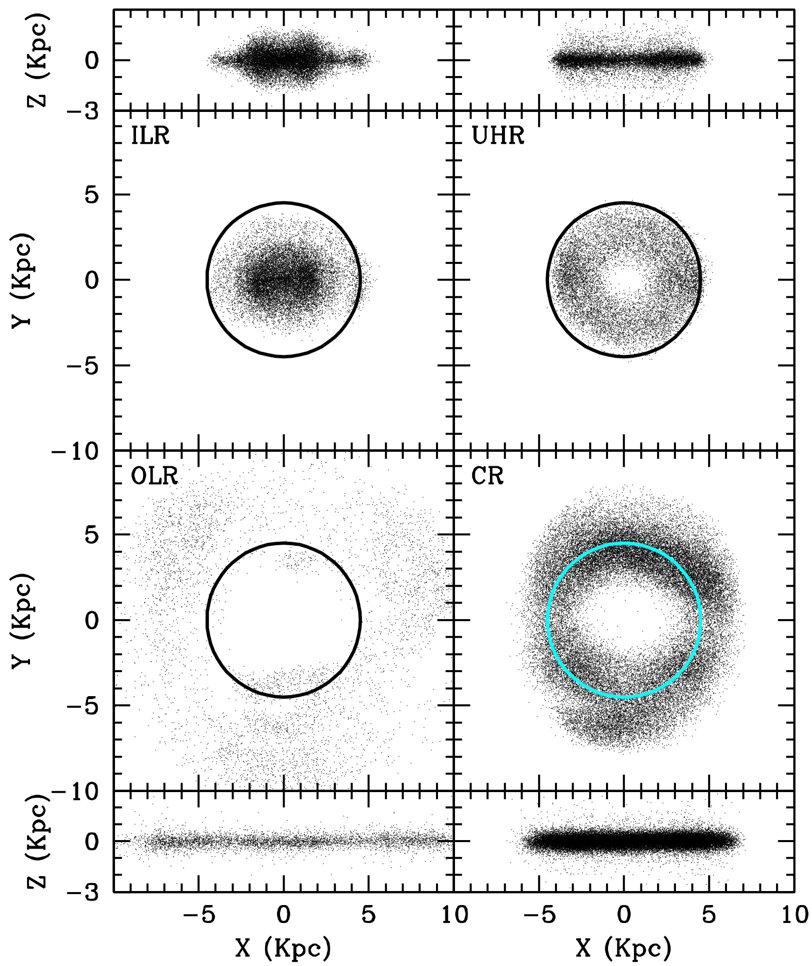

Figure 11.9 Spatial distributions of the particles at different resonances in D_{hs}. Each plot is labeled with the corresponding resonance. All resonances form rings except the ILR. This resonance is not localized at a given radius. A circle marks the corotation radius.

$(\Omega - \Omega_B)/\kappa$ changes dramatically. The tail of high frequencies and high values of $(\Omega - \Omega_B)/\kappa$ grows. This is produced by particles that are sinking into the centre. However, the most dramatic change is the formation of the resonant peaks. Some particles are captured by the bar near some specific resonant orbits. This produces a clustering of particles near specific dynamical frequencies and the formation of the resonant peaks in the distribution of $(\Omega - \Omega_B)/\kappa$. This clustering causes the surrounding areas outside the resonances to be depopulated. This is reflected in gaps in the distribution of $(\Omega - \Omega_B)/\kappa$ at both sides of a resonance. These gaps are very clear for CR and ILR of K_{hb} but they are also visible for the (-1:5) and (1:4) resonances of D_{hs}.

We apply the same technique to find resonances in the halo. We select particles with a height from the plane lower than 3 pc, so that the particles are close to the disk. We also reject retrograde orbits. Fig. 11.8 shows the distribution of $(\Omega - \Omega_B)/\kappa$ for the halo of K_{hb} for a period of 2 Gyr. The pattern of resonances in the halo is very similar than the resonances in the disk. In particular, CR and ILR are clearly present.

11.7 Spatial Distribution of Particles at Resonances

We have seen the clustering of particles near resonances in the space of dynamical frequencies. But, what is their distribution in the coordinate space? Are they localized around a specific radius or are they spread over a broad region of the system? Fig. 11.9 shows the spatial distribution of the particles at the main resonances in D_{hs}. These are the disk particles which form the main peaks in the Fig. 11.6. They are confined into broad areas. Thus, particles near resonances populate a broad region of space. For example, particles trapped at CR stay at a broad ring around the corotation radius. However, the distribution is not uniform along the ring. There are fewer particles near the ends of the bar and more particles at both sides of the bar. This asymmetry is related to the position of the Lagrange points of the system, as we will see in §11.8. Other rings are also formed at UHR and OLR.

However, particles at ILR do not form a ring. The ILR is not localized around a given radius. Fig. 11.10 shows the particles near ILR for the model K_{hb}. They are concentrated in an elongated structure that resembles the bar. Particles at ILR can pass very close to the centre and they have very elongated orbits. As a result, they span a wide range of radii. This result implies that ILR extends over a broad range of energies. This fact was outlined in different papers. Athanassoula (2003) pointed out the fact that the ILR resonant orbits are in fact the members of the x1 family of closed orbits. Athanassoula (1992) studied the energy range in which these resonant orbits are stable so they are able to capture orbits around

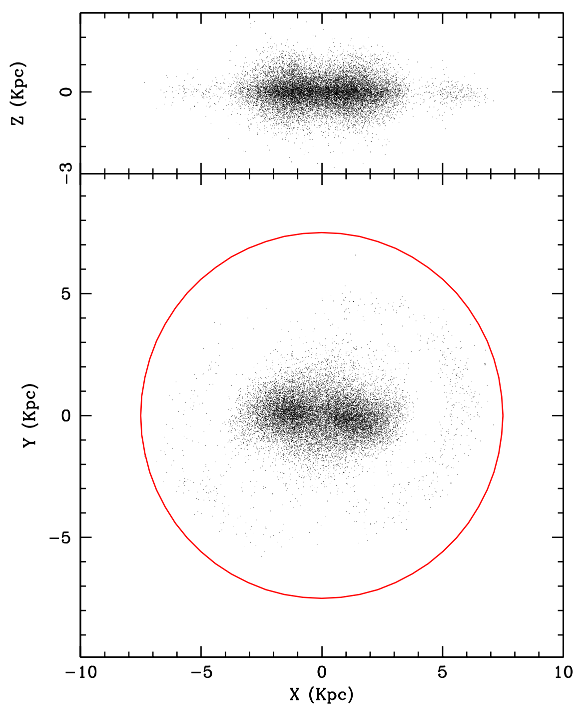

Figure 11.10 Spatial distribution of the particles at ILR in K_{hb}. The bottom panel shows a face-on view. The distribution resembles the bar. ILR particles can pass very close to the centre and span a wide range of radii. A circle marks the corotation radius. the top panel shows the vertical distribution. This edge-on view has a clear rectangular shape.

them. They found that ILR orbits are stable over a significant range of values of the Jacobi energy. Weinberg & Katz (2007a) also found that ILR orbits extend to very small radii.

In general, the vertical distribution near these resonances is very flat. This is expected because we are focusing on planar resonances, so we do not expect resonant motions in the vertical direction. However, ILR is a clear exception. Its edge-on view has a clear rectangular shape (Fig. 11.10). This distribution again resembles the bar. Edge-on views of N-body bars show the same rectangular shape (Athanassoula & Misiriotis, 2002). A frequency analysis of motions in the vertical direction shows some particles trapped in the vertical ILR with the same values of their radial and vertical frequencies. The trajectories of these particles have their radial and vertical oscillations coupled.

11.8 Corotation Capture

In previous sections, we saw that resonances can capture particles with specific frequency ratios. Now we are going to focus on the details of this capture mechanism and to describe what happens with the particles after being trapped near a resonance. We take CR, $\Omega = \Omega_B$, as an example, because it is easy to visualize. We use the model C of Valenzuela & Klypin (2003) to study the particles near CR. Particles which stay near CR during a period of 1 Gyr centred at 3.5 Gyr are selected. Fig. 11.11 and 11.12 show their spatial distribution and their density profiles at different moments. At 0.1 Gyr, just before bar formation, the particles are spread in an axisymmetric and extended distribution around the centre. This distribution is strongly affected by the formation of the bar. They gain angular momentum and evolve in to a ring at the corotation radius. As a result, these particles evolve when they are being trapped at CR during the formation of the bar. After that, the distribution is stable for more than 4 Gyr or 20 bar rotations. As we discussed in §11.7, the ring is not uniform. It shows a stronger concentration of particles in two broad areas 90° away from the major axis of the bar. In addition, the surface density profile of these particles shows a stationary peak close to the corotation radius (Fig. 11.12). These particles are still trapped near CR several Gyr after the formation of the bar. Therefore, CR prevents a secular evolution in the trajectories of the particles trapped around it.

We can now study in detail how CR prevents the secular evolution of trapped particles in an almost stationary model, in which Ω_B is almost constant. We start with the spatial distribution of the change in angular momentum of particles in the disk. We compute the change of angular momentum of each particle between two different moments. That change contributes to the average angular momentum change at the position of the particle in an intermediate moment. The result is a field of angular momentum change. If these two moments are very close, that field is a good approximation to the instantaneous change of angular momentum in the disk. In other words, we are measuring the torque field produced by the bar and the spiral arms (Fig. 11.13). This torque has a similar shape of a torque from an elongated structure in rotation. It shows a 180° symmetry. The bar is rotating in anti-clockwise direction. Therefore, the particles which are close to the bar and moving ahead of the bar, are being pushed backwards by the bar and they lose angular momentum (black areas in Fig. 11.13). At the same time, particles which are moving behind the bar, are being pushed forwards. Therefore they gain angular momentum (dark grey areas in Fig. 11.13).

However, small changes in angular momentum over short periods of time can accumulate over a longer period. This can produce a much stronger change in angular momentum over a long period of time. Fig. 11.14 shows only the areas with the largest variations in angular momentum over a much longer interval of time than in Fig. 11.13. The selected interval is nearly one period of the bar, 150 Myr. The choice of different intervals produces similar results. The largest change of angular momentum lays mainly near the corotation radius and away from the major and minor axes of the bar. The two areas of positive change of angular momentum do not cover the same area. One is bigger than the other. However, this asymmetry is not permanent. It oscillates slowly with time. As a result, the net effect of this asymmetry is averaged out. Other peaks are also found inside the bar, a region dominated by ILR orbits. Finally, other peaks beyond the corotation radius could be attributed to the OLR.

Near the corotation radius, particles which are moving behind the bar for a significant interval of time accumulate small increments of angular momentum over that interval. The net effect is a significant increase in their angular momentum. The opposite is true for particles which stay ahead of the bar for a long period of time. They lose a significant amount of angular momentum. The main question is now how this change in angular momentum affects the evolution of these particles. The naïve idea is that a particle that increases its angular momentum evolves strongly. However, a particle initially in one of the areas of maximum positive change in angular momentum near CR (grey/red areas in Fig. 11.13) gains angular momentum and moves outward. As a result, the particle rotates slower than the bar, $\Omega < \Omega_B$. It lags the bar and starts to move to the area of negative angular momentum change (black/blue areas in Fig. 11.13). In that area, the particle loses the angular momentum gained previously and moves inwards. As a result, it starts to rotate faster than the bar, $\Omega > \Omega_B$, and to move towards the area of positive change of angular momentum. In that area, the particle gains angular momentum and the cycle starts again. As a result, the changes in angular momentum are compensated along the trajectory of each particle near CR. These oscillations of angular momentum produces no net torque over a long

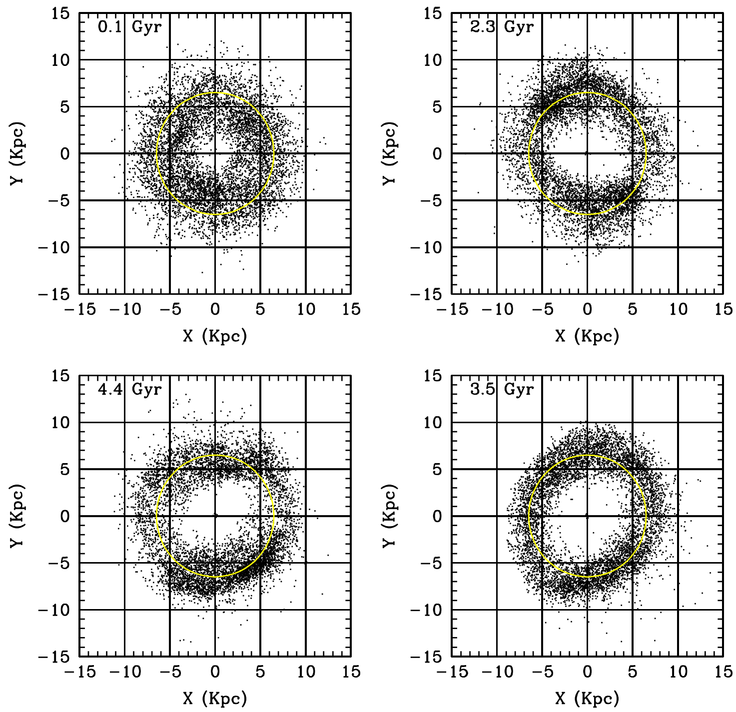

Figure 11.11 Spatial distribution of the particles selected for being near CR at 3.5 Gyr at 4 different moments. The particles are taken from the model C. At 0.1 Gyr, the bar is still not formed. After, bar formation, the distribution of these particles is stationary for more than 4 Gyr. Particles trapped near CR stay there for a long time. The circle represents the corotation radius.

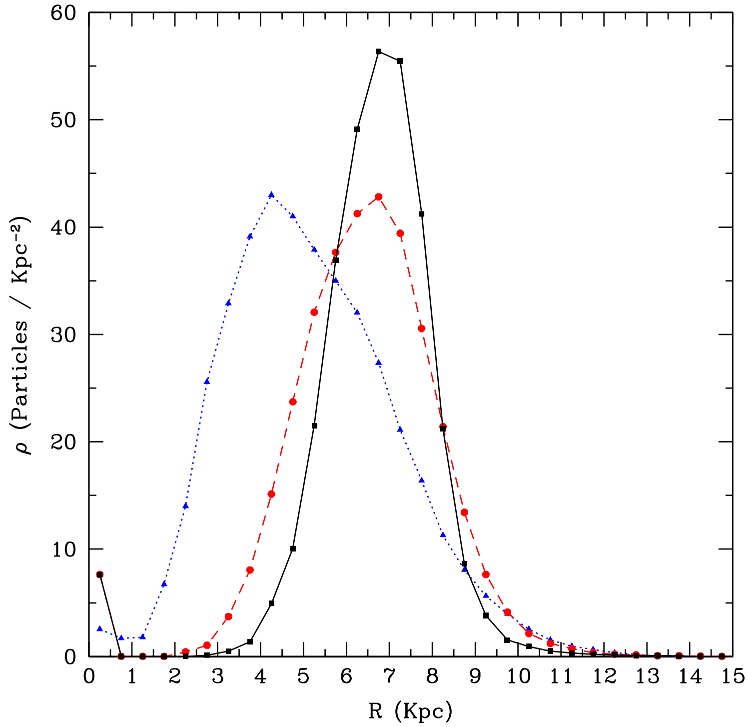

Figure 11.12 Evolution of the surface density profile of particles selected for being near CR at 3.5 Gyr for model C. The full curve corresponds to the distribution of the particles at 3.5 Gyr. The dotted curve shows the same particles at 0.1 Gyr, before the bar formation. The dashed line is for 4.5 Gyr, 1 Gyr after the moment in which the particles are selected for being at CR. As the bar forms, some particles get trapped near corotation radius. After that, the profile shows a peak centered at the corotation radius. The distribution shows little evolution for 4 Gyr.

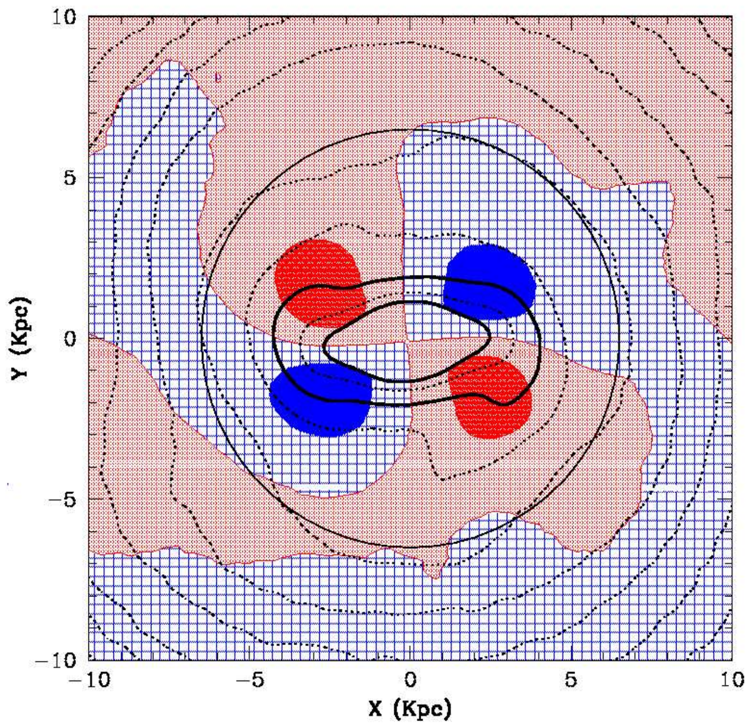

Figure 11.13 Spatial distribution of the instantaneous angular momentum change measured in a short interval of 28 Myr in model C. See electronic version of a color version of this plot. The two black leaves (dark blue) are areas with a strong negative torque. The two dark grey leaves (dark red) have a strong positive torque. Finally, the broad areas filled with squares (light blue) have a small negative torque, while the areas colored with a light grey (light red) have a small positive torque. The bar is rotating in anti-clockwise direction. The particles which are close to the bar and moving ahead of the bar, lose angular momentum (black/blue areas). At the same time, particles which are moving behind the bar, gain angular momentum (dark grey/red areas).

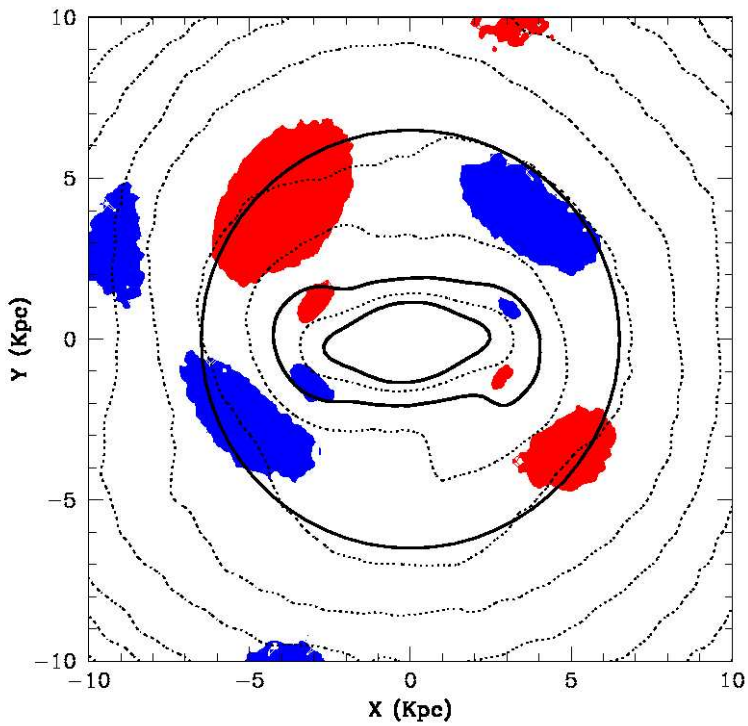

Figure 11.14 Distribution of the peaks in the change in angular momentum in the disk for a longer period of time (150 Myr). The grey (red) areas show the position of the particles with the maximum increment in their angular momentum. The black (blue) areas show the position of the particles with the maximum decrement of angular momentum. Those areas lie mainly along the corotation radius (black circle)

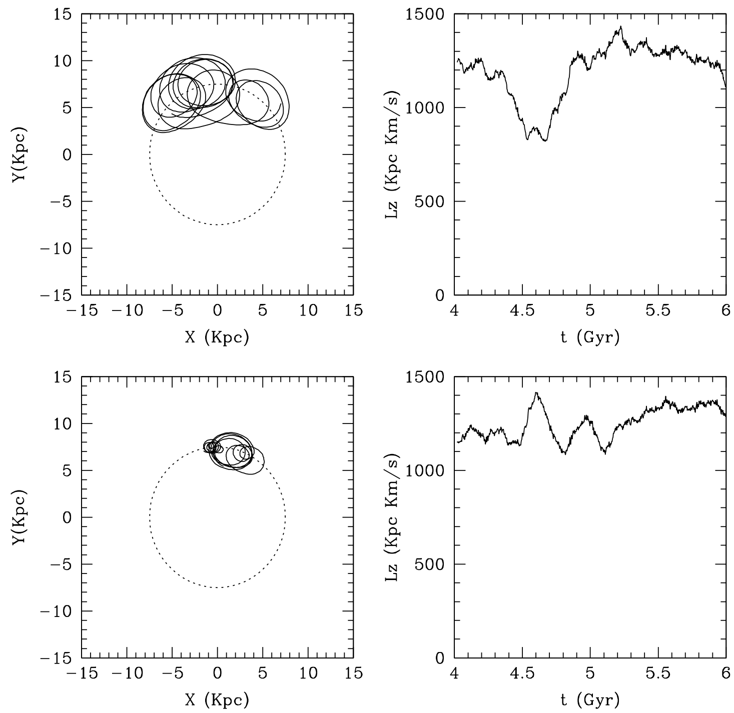

Figure 11.15 Example of two trajectories of particles near CR for 2 Gyr in the model K_{hb}. They are selected for being near CR between 4 Gyr and 4.5 Gyr. The left panels show their trajectories in the reference frame which rotates with the bar. The bar is always along the horizontal axis. The dotted circle is at the corotation radius. The example at the top is a trajectory in libration around a stable Lagrange point The trajectory at the bottom is even closer to this point. The right panels show the angular momentum of both trajectories over 2 Gyr. The angular momentum oscillates, but there is no overall change of angular momentum. These trajectories do not evolve. As a result, CR prevents the evolution for orbits trapped around it.

period of time. CR actually prevents the evolution of the particles trapped near the corotation radius.

Fig. 11.15 provides two examples which illustrate this previous idea. They are taken from the model K_{hb}. The particles are selected to be near CR between 4 and 4.5 Gyr. Then, we plot their trajectories for the next 2 Gyr. We select the non-inertial frame which rotates with the bar. In that frame, the bar is always along the horizontal axis and a particle exactly at CR is not moving in this frame. The top panels of Fig. 11.15 show a particle which slowly oscillates once along a section of the corotation ring during 2 Gyr. The particle moves between the areas in which the change of angular momentum is positive and negative. As a result, the changes in its angular momentum cancel each other. The net result of this oscillation is an almost no change in the angular momentum. The particle is trapped in an orbit of libration for several Gyr and many orbits.

The bottom panels of Fig. 11.15 show an orbit closer to CR. It also librates at the corotation radius but the amplitude of the oscillations are much smaller than in the previous case. Actually, during the last Gyr of the simulation, the particle spends several orbits around a single point in the rotating frame. The angular momentum during this time is almost constant. So, the net transfer of angular momentum near that point is minimum. In other examples, the orbits librate in a similar way but around another point on the other side of the corotation ring.

This trapping mechanism near CR is actually well known in galactic and celestial mechanics. The situation is equivalent to the motions of arbitrary amplitude around the stable Lagrange points of a stationary non-axisymmetric system. The equations of motion can be reduced to the equations of a pendulum (Binney & Tremaine, 1987, Chapter 3, eqs. (3-123)-(3-129)). Particles trapped near CR librate slowly around one of the stable Lagrange points. A particle exactly at this point is exactly at CR. A close example of such a resonant orbit is shown in the bottom panels of Fig. 11.15. This orbit moves along the corotation radius with the same angular velocity of the bar rotation. CR keeps particles in libration orbits for a long time and for many periods. While particles are trapped, their orbits do not evolve. As a result, CR prevents the evolution of the particles trapped around it and minimize their angular momentum transfer.

11.9 Comparison with an Analytical Model

As we saw in the previous section, CR captures particles around two stable Lagrange points. The stability around these points is mainly determined by the topology of the gravitational potential around them. Therefore, we can approximate this potential with a simple analytical model which captures the main features of a strongly barred system. Such a model can be used to clarify the

Table 11.3 Set of parameters for the analytical model.

Miyamoto disk:	
Disk Mass ($10^{10}M_\odot$)	5
A (kpc)	4
B (kpc)	1
NFW halo:	
r_s (Kpc)	28.7
ρ_0 ($10^6M_\odot$ Kpc$^-3$)	3.12
Prolate ellipsoid:	
Bar mass ($10^{10}M_\odot$)	1
Semimajor axis (Kpc)	4
Semiminor axis (Kpc)	1
Pattern speed (km s^{-1} Kpc^{-1})	36

results of N-body simulations. The analytical potential consists of a Miyamoto disk, a NFW halo and a homogeneous prolate ellipsoid. The ellipsoid rotates with a given pattern speed Ω_B. The corresponding expressions are described in section 11.10 and the parameters of the model are given in Table 11.3. It reproduces a strongly barred galaxy. Its circular velocity profile is shown in Fig. 11.16. Using this background potential, we can compute the trajectories of a set of particles and follow their resonant interactions with the bar. This analytical model can catch some fundamental aspects of resonances, like trapped orbits near resonances. At the same time, this simple model does not have the inherent complexity of a self-consistent N-body simulation. As a result, it is easy to interpret. Then, this interpretation can be used to understand better the resonant phenomena in more complex and realistic cases, like in N-body models.

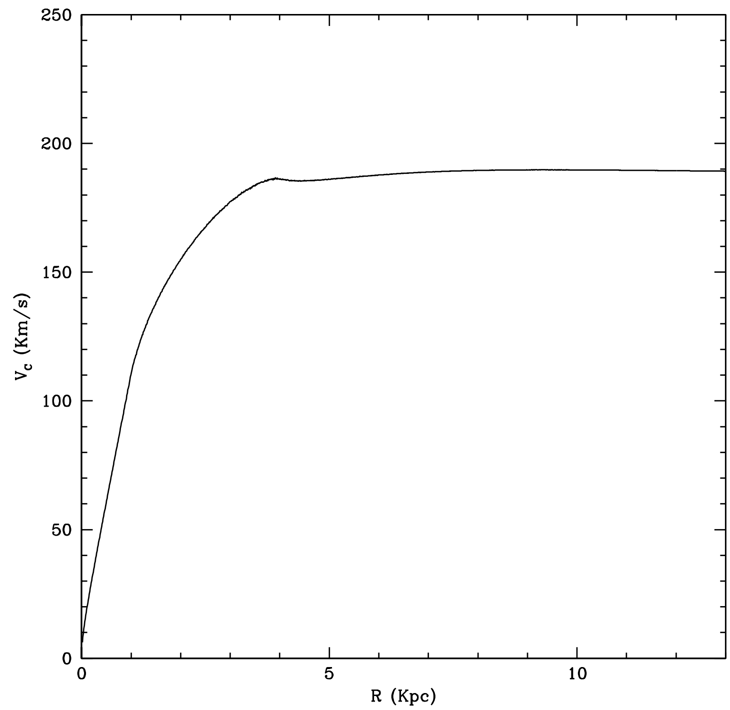

Figure 11.16 Circular velocity profile of the analytical model of a barred galaxy. The model corresponds to a typical high surface brightness barred galaxy with a maximum circular velocity close to 190 km s^{-1}.

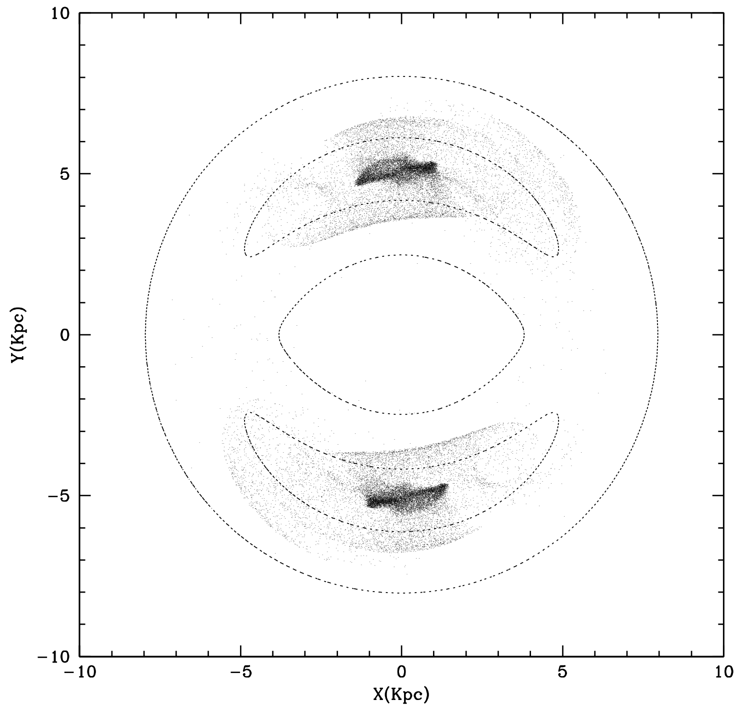

Figure 11.17 Spatial distribution of the particles trapped at CR after 100 bar rotations (17 Gyr) The distribution fills two lobes around the stable Lagrange points. It resembles the distribution of particles trapped near CR in the N-body models (Fig. 11.9 and 11.11). The background contours are contours of equal effective potential.

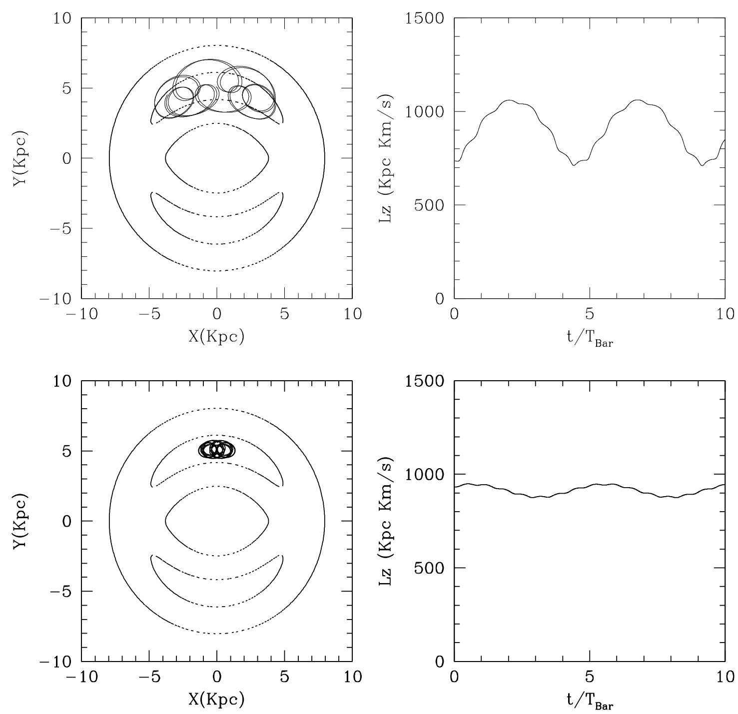

Figure 11.18 Two examples of trajectories trapped near CR, as in Fig. 11.15. The trajectories librate around the stable Lagrange point and their angular momentum oscillates with no net change of angular momentum after approximately 5 bar periods.

Fig. 11.17 shows particles trapped near CR at two stable Lagrange points. The initial configuration is a set of 32^3 particles distributed uniformly inside two small spheres of 0.1 Kpc in radius. Each one is centered at each stable Lagrange point. The distribution of velocities is initially centered on the circular velocity at the corotation radius. The dispersion is 25 per cent of that velocity. After 100 bar rotations, almost all particles fill two banana-shape areas at both sides of the bar. They are still trapped around the stable Lagrange points. They cover a broad area along the corotation radius. This supports the results discussed in §11.8 for a self-consistent N-body experiment. The distribution of the particles near CR in Fig. 11.9 and 11.11 resembles the distribution of the particles trapped around the two stable Lagrange points in Fig. 11.17. The region of trapped particles is not an infinitesimal volume around the stable points. It extends over a broad volume both in spatial and phase space. The distribution of the energies of these particles cover a range which is 10 per cent of the energy at the Lagrange point. CR covers a significant volume in phase space, although the only particle formally at resonance is the one which moves with one of the stable points.

In general, these trapped particles move in libration orbits around the Lagrange points. They are trapped for a cosmologically significant period of time. Fig. 11.18 shows two examples of libration orbits and the change of their angular momentum. These examples can be compared with the examples taken from the N-body model and discussed in §11.8. The first example has a large amplitude of libration. As a result, the angular momentum oscillates significantly. However, the angular momentum oscillates and the net change is canceled in a libration period. As a result, the net angular momentum transfer over many orbits is zero. The bottom panels of Fig. 11.18 show another example. Its amplitude of libration is much smaller than in the first example. The oscillations in the angular momentum are also much smaller. This example is similar to the second example of §11.8. The particle is closer to CR and remains in a stable orbit which minimizes the transfer of angular momentum. This supports the interpretation that resonances prevent the orbital evolution of trapped particles.

Similar conclusions can be obtained for other resonances. In the case of the ILR, the resonant orbits are closed orbits elongated along the bar. The top panels of Fig. 11.19 show an example of a ILR orbit. The angular momentum oscillates significantly but the net change of angular momentum averaged over one orbit is zero. As we pointed in §11.7, the ILR orbits are known as the $x1$ family. They are the backbone of the orbits which support the bar (Skokøs et al., 2002; Athanassoula, 1992). These resonant orbits capture particles around them in a similar way that corotation does. The bottom panels of Fig. 11.19 show one example of a trajectory trapped around the ILR orbit. The trajectory librates around the closed orbit. The angular momentum is modulated by this libration but again the net average change over many periods is zero. The main difference between CR and ILR is that ILR orbits are a set of orbits instead of two Lagrange points. The result is that the ILR resonance covers a larger volume in phase space which covers the bar, as we saw in the distribution of ILR particles in Fig. 11.10. The trajectories in Fig. 11.19 are stable forever. We tracked them for more than 100 bar rotations and there is no indication of evolution in their trajectories. As we saw before, particles trapped at resonance do not evolve. For the ILR, particles are trapped by a set of $x1$ orbits and forced to move within the bar as the bar rotates.

However, what happens with the particles trapped at resonance when the bar evolves? In this case, the resonant structure also evolves. The volume in the phase-space which satisfies a particular resonant condition drifts through the phase-space. Does the trajectory initially trapped at a resonance follow it or is scattered off resonance? In order to address this issue, we follow the same ILR trajectories when the bar slows its rotation. The top panels of Fig. 11.20 show the imposed bar pattern speed. It remains constant for 30 initial bar rotations (5 Gyr), then it decreases linearly for other 30 initial bar rotations and finally remains constant for 40 initial bar rotations. At the end, the bar pattern speed decreases to 40 per cent of its original value over 5 Gyr. From each trajectory, we extract the specific angular momentum averaged over time for an orbit in the rotating frame and its radial and angular frequencies over the orbit. The radial frequency is computed as $\kappa = 2\pi/T_p$, where T_p is the period of the radial oscillations, defined as the time between apocenters. At the same time, the angular frequency is defined as $\Omega = \Delta\Phi/T_p$, where $\Delta\Phi$ is the angle swept by the trajectory between apocenters in the inertial frame. Using these frequencies and the pattern speed of the bar, we can check the resonant condition for ILR (Eq. 11.2).

The left side of Fig. 11.20 shows the orbit which is initially trapped exactly at ILR. Before any evolution, the averaged angular momentum remains constant and the resonant condition is fulfilled. During the slowdown of the bar, the angular momentum of the trajectory decreases at almost the same rate of the change in the pattern speed. The trapped particle follows the slowdown of the bar. More important is the fact that the trajectory remains close to the resonance although the system evolves. The particle is trapped at resonance and oscillates around the resonant orbit as the system evolves as a whole. This tracking of a resonance is true even for trajectories further from the exact resonant orbit but still trapped around it. The right side of Fig. 11.20 shows an example. The oscillations around the resonant condition are larger than in the previous case, but the trajectory is not scattered off resonance when the system evolves. The same results can be found for bigger rates of change in the pattern speed. Only when the pattern speed decreases to one half of its original value in less than one bar period, the oscillations around the resonant condition become wider.

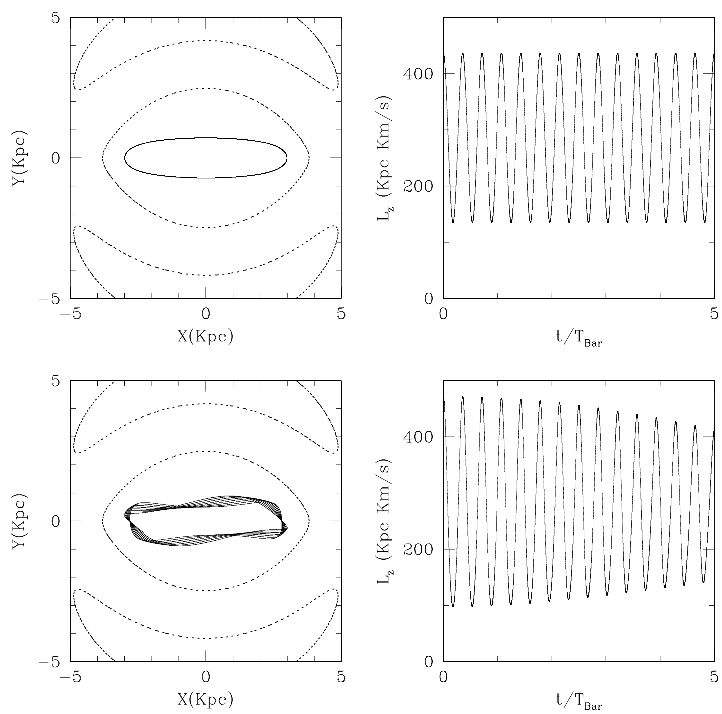

Figure 11.19 Two examples of trajectories as in Fig. 11.15 but for the ILR. The top panels show an example of a ILR orbit. The angular momentum oscillates but average change of angular momentum is zero. The bottom panels show one example of a trajectory trapped around the ILR orbit. The trajectory librates around the closed orbit. The angular momentum is modulated by this libration but again the net average change over many periods is zero.

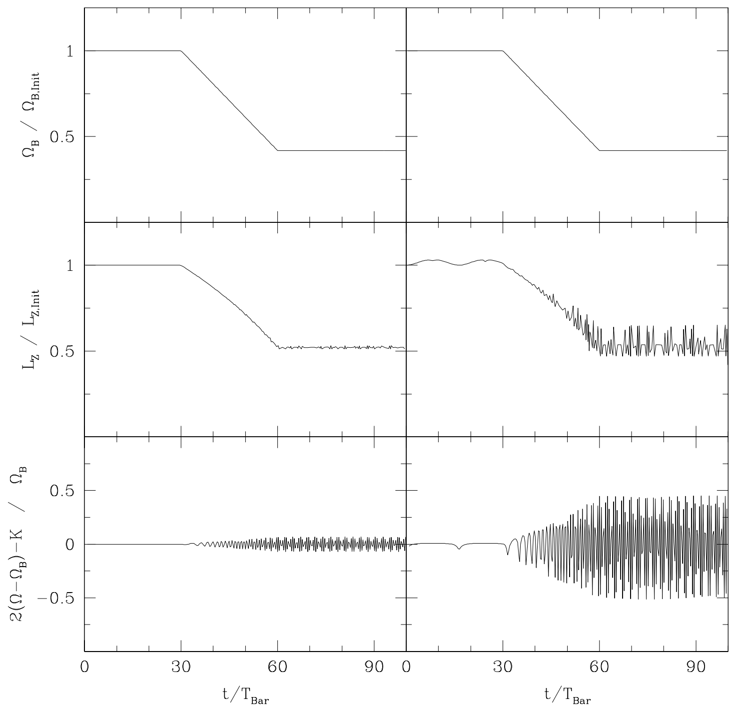

Figure 11.20 Left and right panels show two different examples of particles near ILR when the bar slows its rotation during 30 bar rotations between 30 and 60 bar rotations. Top panels show the evolution of the bar pattern speed. Middle panels show the evolution of the angular momentum averaged over a single orbit. Bottom panels show the ILR condition (eq. 11.2) scaled by Ω_B. During the slowdown of the bar, the trajectory exactly at ILR(left) and the trajectory trapped near ILR(right) remain near resonance. They track the resonance and follow the bar evolution.

11.10 An Analytical Galactic Potential

The 3D potential used in §11.9 consists of three components. First, A Miyamoto potential represents the disk:

$$\Phi_D(\mathbf{x}) = -\frac{GM_D}{\sqrt{x^2 + y^2 + (A + \sqrt{B^2 + z^2})^2}} \tag{11.13}$$

where M_D is the mass of the disk, A and B are the horizontal and vertical scale-lengths. The dark matter halo is modeled using a NFW halo:

$$\Phi_H(\mathbf{x}) = -4\pi G\rho_s r_s^2 \frac{\ln(1 + r/r_s)}{r/r_s}, \; r = \sqrt{x^2 + y^2 + z^2} \tag{11.14}$$

Finally, the contribution of the bar is modeled as a prolate homogeneous ellipsoid. The potential of a point inside the ellipsoid is given by

$$\Phi_B(\mathbf{x}) = -\pi G\rho \left(I(\mathbf{a})a_1^2 - \sum A_i(\mathbf{a})x_i^2 \right) \tag{11.15}$$

where $x_i = \{x, y, z\}, i = 1, 3$. a_1 is the semimajor axis of the bar and $a_2 = a_3$ is the semiminor axis. $I(\mathbf{a})$ and $A_i(\mathbf{a}), i = 1, 3$ are defined by the relations:

$$I(\mathbf{a}) = \frac{1}{e} \ln \frac{1+e}{1-e} \tag{11.16}$$

$$e = \sqrt{1 - \frac{a_1^2}{a_3^2}} \tag{11.17}$$

$$A_1(\mathbf{a}) = \frac{1-e^2}{e^2} \left[\frac{1}{1-e^2} - \frac{1}{2e} \ln \frac{1+e}{1-e} \right] \tag{11.18}$$

$$A_2(\mathbf{a}) = A_1(\mathbf{a}) \tag{11.19}$$

$$A_3(\mathbf{a}) = 2\frac{1-e^2}{e^2} \left[\frac{1}{2e} \ln \frac{1+e}{1-e} - 1 \right] \tag{11.20}$$

Similarly, the potential of a point outside the ellipsoid is given by:

$$\Phi_B(\mathbf{x}) = -\pi G\rho \frac{a_1 a_2 a_3}{\acute{a}_1 \acute{a}_2 \acute{a}_3} \left(I(\acute{\mathbf{a}})\acute{a}_1^2 - \sum A_i(\acute{\mathbf{a}})x_i^2 \right) \tag{11.21}$$

where

$$\acute{a}_i^2 = a_i^2 + \lambda(\mathbf{x}) : \sum \frac{x_i}{\acute{a}_i^2} = 1. \tag{11.22}$$

11.11 Discussion

Resonances play an important role in barred galaxies. Stable resonant orbits can capture disk and halo material in near-resonant orbits. The bar itself is a manifestation of this resonant capture. The $x1$ family of closed orbits are ILR resonant orbits that capture particles in elongated orbits along the bar major axis (Athanassoula, 2003). These orbits support the orbital structure of the bar (Skokøs et al., 2002; Athanassoula, 1992).

Resonances prevent the dynamical evolution of the material trapped near resonant orbits. This material does not experience a net change of angular momentum although the angular momentum oscillates strongly over an orbital period (Fig. 11.19). A particle exactly at resonance with the bar has no evolution in its trajectory. The change in angular momentum over an orbital period is zero. The particle exactly at resonance stay at a resonant closed orbit forever. As a result, resonances tend to minimize the exchange of angular momentum between trapped material and the bar.

Therefore, the mere presence of resonances in barred galaxies do not drive their secular evolution. Orbits trapped at resonance only evolve if the bar evolves as a whole (Fig. 11.20). In this case, resonances drift as the bar evolves. Particles anchored near resonant orbits track the resonances and consequently evolve. As a result, the evolution at resonances is linked to the evolution of the bar. For example, if the bar slows its rotation, the Lagrange points move outwards. As a result, CR moves outwards and trapped particles, which track the motion of CR, move also outwards. The result is that these particles near CR gain angular momentum and evolve. At the same time, ILR particles trapped by the bar lose angular momentum. This angular momentum is not lost because the particles are near a resonance. It is lost because there is a net torque, which produces a slowdown of the bar and of the trapped particles trapped near ILR.

This torque can be the result of the dynamical friction with the dark matter halo. Resonances in the halo can also play an important role in this interaction. ILR particles in the halo form an ellipsoidal structure in the inner halo (Colín et al., 2006). This halo bar exerts a torque on the stellar bar that slows its rotation. This is an interaction between different structures trapped at ILR. As a result of this interaction, ILR particles in the stellar bar can lose angular momentum and ILR particles in the halo can gain it. This interpretation is consistent with the results on the angular momentum change near resonances in the case of the bar slowdown (Athanassoula, 2003). However, this mechanism of change of angular momentum at resonances is very different from the resonant transfer of angular momentum predicted in perturbation theory (Athanassoula, 2003; Lynden-Bell & Kalnajs, 1972).

The resonances found in Athanassoula (2003) are consistent with the resonances found in our models. However, the models in Athanassoula (2003) have a stronger ILR, CR was weaker and outer resonances like OLR were almost absent. These differences are due to differences in the corotation radius. Based on the initial rotation curve and the pattern speed of the model MQ2 of Athanassoula (2003), the corotation radius was roughly 20 Kpc, 5.7 times its disc scalelength. This is 5 times larger than the corotation radius in our model D_{hs}. Thus, the models in Athanassoula (2003) have most of the material of the disk within the corotation radius. This material can only be captured by inner resonances like ILR. That results in a strong ILR peak. On the other hand, little material lies at corotation radius and beyond. Therefore, CR, OLR and other outer resonances can trap only a few particles. This is why their peaks in the $(\Omega - \Omega_B)/\kappa$ histogram of Athanassoula (2003) are much smaller than in our model D_{hs}.

Recently, Weinberg & Katz (2007a) discussed the dynamics of the interaction between a bar and a dark matter halo and described the requisites needed to follow this resonant interaction accurately. The first criterion stated that a N-body model should have enough phase-space coverage at resonances. In order to ensure the correct resonant behavior, the phase space near resonances should be populated with enough particles. The phase-space volume near resonances is defined by the separatrix which divides trapped from non-trapped orbits in the phase space near a resonance. This volume covers the region of trapped orbits which librate around the stable resonant orbit. Weinberg & Katz (2007a) argue that 10 particles inside one tenth of that resonant region are enough to obtain the correct behavior at resonances. Our model D_{hs} has around 1.5×10^4 disk particles near ILR and 4.1×10^4 near CR. These are trapped particles which stay in the libration region near resonances. As a result, resonances are well populated in our N-body models. This is because the region of trapped orbits is large (Fig. 11.6, 11.7, 11.8).

The second criterion deals with the artificial noise in the potential and the effects of two-body scattering. They can introduce an artificial diffusion of orbits. The characteristic diffusion length should be smaller than the resonance width, defined by the size of the region of trapped orbits. Otherwise, particles can artificially diffuse out of a resonance. We have seen that these regions near resonances are large. So, this second criterion is also achieved.

11.12 Summary and Conclusions

We have detected dynamical resonances in N-body models of barred galaxies with evolving disks in live dark matter halos. The dominant resonances are the corotation resonance (CR) and the inner Lindblad resonance (ILR), although other low order resonances, like the outer Lindblad resonance (OLR) or the ultra-harmonic resonance (UHR) are also present (Fig. 11.6, 11.7, 11.8). Resonances in the halo are also found.

In general, resonances cover broad areas of the disk (Fig. 11.9). Particles at CR are distributed in a wide ring at the corotation radius. On the other hand, the epicycle frequencies are not equal to the natural frequencies of particles inside the corotation radius, where non-circular motions are important. This is specially true for the ILR. this resonance is not localized at a given radius. Particles at ILR are found mainly in elongated orbits inside the bar. Their distribution resembles the bar (Fig. 11.10)

In all three studied models, we find that resonances capture particles and force them to move in trajectories near stable resonant orbits. For example, the corotation resonance traps particles in libration orbits around the two stable Lagrange points of the system. As a result, the angular momentum oscillates with the period of the libration motion but the net change over many orbits is zero. Therefore, these trapped particles do not evolve. We conclude that resonant trapping tends to minimize the change of angular momentum of the particles trapped around them. However, the trapped particles can participate in the global evolution of the bar because they are locked at resonances. They are still trapped during the slowdown of the bar (Fig. 11.20). As a result, ILR particles can lose angular momentum during this slowdown. Particles trapped at resonances only evolve when the bar evolves as a whole.

REFERENCES

Aarseth, S. J. 1963, MNRAS, 126, 223

Abadi, M. G., Navarro, J. F., Steinmetz, M., & Eke, V. R. 2003, ApJ, 591, 499

Arnold V. I., Avez A., 1968, Ergodic problems of classical Mechanics, W.A. Benjamin, Inc.

Athanassoula E., 1992, MNRAS, 259, 328

Athanassoula E., 2002, ApJL, 569, L83

Athanassoula E., Misiriotis A., 2002, MNRAS, 330, 35

Athanassoula E., 2003, MNRAS, 341, 1179

de Avillez, M. A. 2000, MNRAS, 315, 479

de Avillez, M. A., & Breitschwerdt, D. 2004, A&A, 425, 899

de Avillez, M. A., & Breitschwerdt, D. 2007, ApJL, 665, L35

Bardeen, J. M., Bond, J. R., Efstathiou, G., 1987, ApJ, 321, 28

Barnes, J., & Efstathiou, G. 1987, ApJ, 319, 575

Barnes, J. E., & Hernquist, L. 1996, ApJ, 471, 115

de Bernardis, P., et al., 2000, Nature, 404, 955

Benson, A. J., Frenk, C. S., Baugh, C. M., Cole, S., & Lacey, C. G. 2003, MNRAS, 343, 679

Bett, P., Eke, V., Frenk, C. S., Jenkins, A., Helly, J., & Navarro, J. 2007, MNRAS, 376, 215

Binney J., Tremaine S., 1987, Galactic Dynamics. Princeton Univ. Press, Princeton, NJ

Birnboim, Y., & Dekel, A. 2003, MNRAS, 345, 349

Blaauw, A. 1961, Bull. Astron. Inst. Netherlands, 15, 265

Blanton M. R. et al., 2003, ApJ, 594, 186

de Blok, W. J. G., McGaugh, S. S., Rubin, V. C., 2001, AJ, 122, 2396

Blumenthal, G. R., Faber, S. M., Primack, J. R., & Rees, M. J. 1984, Nature, 311, 517

Bond, J. R., et al., 2000, arXiv:astro-ph/0011378

van den Bosch, F. C., Burkert, A., & Swaters, R. A. 2001, MNRAS, 326, 1205

Brook, C. B., Kawata, D., Gibson, B. K., & Freeman, K. C. 2004, ApJ, 612, 894

Bullock, J. S., Kolatt, T. S., Sigad, Y., Somerville, R. S., Kravtsov, A. V., Klypin, A. A., Primack, J. R., & Dekel, A. 2001, MNRAS, 321, 559

Bullock, J. S., Dekel, A., Kolatt, T. S., Kravtsov, A. V., Klypin, A. A., Porciani, C., & Primack, J. R. 2001, ApJ, 555, 240

Byrd G., Freeman T., Buta R., 2006, AJ, 131, 1377

Cen, R., & Ostriker, J. P. 1999, ApJ, 514, 1

Ceverino, D., Klypin, A. ArXiv e-prints, 712, arXiv:0712.3285

Chirikov B. V., 1960, Journal of Nuclear Energy, 1, 253

Clark, P. C., Bonnell, I. A., Zinnecker, H., & Bate, M. R. 2005, MNRAS, 359, 809

Cole, S., et al., 2005, MNRAS, 362, 505

Colella, P., & Woodward, P. R. 1984, Journal of Computational Physics, 54, 174

Colella, P., & Glaz, H. M. 1985, Journal of Computational Physics, 59, 264

Colín P., Klypin A., Kravtsov A., 2000, ApJ, 539, 561

Colín P., Valenzuela O., Klypin A., 2006 ApJ, 644, 687

Conroy, C., et al., 2007, ApJ, 654, 153

Contopoulos G., Grosbøl P., 1989, A&AR, 1, 261

Courteau S., 1997, AJ, 114, 2402

Cox, D. P. 2005, ARA&A, 43, 337

Cox, T. J., Jonsson, P., Primack, J. R., & Somerville, R. S. 2006, MNRAS, 373, 1013

Cox, T. J., Dutta, S. N., Di Matteo, T., Hernquist, L., Hopkins, P. F., Robertson, B., & Springel, V. 2006, ApJ, 650, 791

Crocce, M., & Scoccimarro, R. 2007, ArXiv e-prints, 704, arXiv:0704.2783

Cuesta, A. et al., 2007, in preparation

Davis, M., Efstathiou, G., Frenk, C. S., & White, S. D. M. 1985, ApJ, 292, 371

Dekel, A., & Silk, J. 1986, ApJ, 303, 39

Dekel, A., & Birnboim, Y. 2006, MNRAS, 368, 2

Diemand, J., Kuhlen, M., & Madau, P. 2007, ApJ, 657, 262

D'Onghia, E., Burkert, A., Murante, G., & Khochfar, S. 2006, MNRAS, 372, 1525

D'Onghia, E., & Navarro, J. F. 2007, MNRAS, 380, L58

Dray, L. M., Dale, J. E., Beer, M. E., Napiwotzki, R., & King, A. R. 2005, MNRAS, 364, 59

Eisenstein, D. J., & Hu, W. 1999, ApJ, 511, 5

Elmegreen, B. G., Efremov, Y., Pudritz, R. E., & Zinnecker, H. 2000, Protostars and Planets IV, 179

Eskridge P. B., et al. 2000, AJ, 119, 536

Fall S.M., Efstathiou G., 1980, MNRAS, 193, 189

Feigelson, E. D., et al. 2005, ApJS, 160, 379

Ferland, G. J., Korista, K. T., Verner, D. A., Ferguson, J. W., Kingdon, J. B., & Verner, E. M. 1998, PASP, 110, 761

Ferrière, K. 1998, ApJ, 503, 700

Ferrière, K. M. 2001, Reviews of Modern Physics, 73, 1031

Fukugita, M., & Peebles, P. J. E. 2004, ApJ, 616, 643

Gao, Y., & Solomon, P. M. 2004, ApJ, 606, 271

Gao, L., Navarro, J. F., Cole, S., Frenk, C., White, S. D. M., Springel, V., Jenkins, A., & Neto, A. F. 2007, ArXiv e-prints, 711, arXiv:0711.0746

Gerritsen, J. P. E., & Icke, V. 1997, A&A, 325, 972

Gies, D. R. 1987, ApJS, 64, 545

Godunov, S., Mat.Sb. 47, no. 3, 271-306

Governato, F., et al. 2004, ApJ, 607, 688

Governato, F., Willman, B., Mayer, L., Brooks, A., Stinson, G., Valenzuela, O., Wadsley, J., & Quinn, T. 2007, MNRAS, 374, 1479

Governato, F., Mayer, L., & Brook, C. 2008, ArXiv e-prints, 801, arXiv:0801.1707

Greene, T. P., & Young, E. T. 1992, ApJ, 395, 516

Guedel, M., Briggs, K. R., Montmerle, T., Audard, M., Rebull, L., & Skinner, S. L. 2007, ArXiv e-prints, 712, arXiv:0712.0476

Gunn, J. E., & Gott, J. R. I. 1972, ApJ, 176, 1

Haardt, F., & Madau, P. 1996, ApJ, 461, 20

Haehnelt, M. G., Steinmetz, M., & Rauch, M. 1998, ApJ, 495, 647

Hahn, O., Porciani, C., Carollo, C. M., & Dekel, A. 2007, MNRAS, 375, 489

Hayashi, E., et al., 2004, MNRAS, 355, 794

Hernquist L., 1993, ApJS, 86, 389

Hetznecker, H., & Burkert, A. 2006, MNRAS, 370, 1905

Hillenbrand, L. A., & Hartmann, L. W. 1998, ApJ, 492, 540

Holley-Bockelmann K., Mihos J. C., Sigurdsson S., Hernquist L., 2001, ApJ, 549, 862

Holley-Bockelmann K., Weinberg M., Katz N., 2005, MNRAS, 363, 991

Holtzman, J., 1989, ApJS, 71, 1

Hoogerwerf, R., de Bruijne, J. H. J., & de Zeeuw, P. T. 2000, ApJL, 544, L133

Jenkins, A., et al., 2001, MNRAS, 321, 372

de Jong R. S. van der Kruit P. C., 1994, A&AS, 106, 451

Jungwiert, B., Combes, F., & Palouš, J., 2001, A&A, 376, 85

Katz, N. 1992, ApJ, 391, 502

Kauffmann G., Guiderdoni B., White S. D. M., 1994, MNRAS, 267, 981

Kaufmann, T., Mayer, L., Wadsley, J., Stadel, J., & Moore, B., 2006, MNRAS, 370, 1612

Kaufmann, T., Mayer, L., Wadsley, J., Stadel, J., & Moore, B. 2007, MNRAS, 375, 53

Kennicutt R. C. Jr., Tamblyn P., Congdon C. E., 1994, ApJ, 435, 22

Kennicutt, R. C., Jr. 1998, ApJ, 498, 541

Kennicutt, R. C., Jr., et al. 2007, ApJ, 671, 333

Kereš, D., Katz, N., Weinberg, D. H., & Davé, R. 2005, MNRAS, 363, 2

Khokhlov, A. 1998, Journal of Computational Physics, 143, 519

Klypin, A., Kravtsov, A. V., Valenzuela, O., & Prada, F. 1999, ApJ, 522, 82

Klypin, A., Kravtsov, A. V., Bullock, J. S., & Primack, J. R. 2001, ApJ, 554, 903

Klypin, A., Zhao, H., & Somerville, R. S. 2002, ApJ, 573, 597

Klypin, A., Hoffman, Y., Kravtsov, A. V., & Gottlöber, S. 2003, ApJ, 596, 19

Kormendy, J., & Kennicutt, R. C., Jr. 2004, ARA&A, 42, 603

Korpi, M. J., Brandenburg, A., Shukurov, A., Tuominen, I., & Nordlund, Å. 1999, ApJL, 514, L99

Kraichnan, R. H. 1967, Physics of Fluids, 10, 1417

Kravtsov, A. V., Klypin, A. A., & Khokhlov, A. M. 1997, ApJS, 111, 73

Kravtsov, A. V. 1999, Ph.D. Thesis,

Kravtsov A.,, 2003, *ApJ* (Letters 590, 1

Kroupa, P., Aarseth, S., & Hurley, J. 2001, MNRAS, 321, 699

Krumholz, M. R., & McKee, C. F. 2005, ApJ, 630, 250

Krumholz, M. R., & Tan, J. C. 2007, ApJ, 654, 304

Lada, C. J., & Lada, E. A. 2003, ARA&A, 41, 57

Lake, G., & Carlberg, R. G. 1988, AJ, 96, 1587

Laskar J., 1990, Icarus, 88, 266

Law, D. R., Steidel, C. C., Erb, D. K., Larkin, J. E., Pettini, M., Shapley, A. E., & Wright, S. A. 2007, ApJ, 669, 929

Lee, J., & Shandarin, S. F. 1998, ApJ, 500, 14

Leitherer, C., et al. 1999, ApJS, 123, 3

Lichtenberg A. J., Lieberman M. A., 1983, Regular and Stochastic Motion. Springer-Verlag, New York

Lifshitz, E.M., Khalatnikov, I.M., 1963, Adv. Phys., 12, 465

Lynden-Bell D., Kalnajs A. J., 1972, MNRAS, 157, 1

Mac Low, M.-M., & Ferrara, A. 1999, ApJ, 513, 142

Martinez-Valpuesta I., Shlosman I., Heller C., 2006, ApJ, 637, 214

Mashchenko, S., Couchman, H. M. P., & Wadsley, J. 2006, Nature, 442, 539

Mashchenko, S., Wadsley, J., & Couchman, H. M. P. 2007, ArXiv e-prints, 711, arXiv:0711.4803

Mayer, L., Governato, F., & Kaufmann, T., 2008, Advanced Science Letters, in press.

McCray, R., & Snow, T. P., Jr. 1979, ARA&A, 17, 213

McKee, C. F. 1999, NATO ASIC Proc. 540: The Origin of Stars and Planetary Systems, 29

Miller, G. E., & Scalo, J. M. 1979, ApJS, 41, 513

Moore, B., Ghigna, S., Governato, F., Lake, G., Quinn, T., Stadel, J., & Tozzi, P. 1999, ApJL, 524, L19

Murray C. D., Dermott, 1999, Solar system Dynamics, Cambridge University Press Princeton, NJ

Naab, T., Johansson, P. H., Ostriker, J. P., & Efstathiou, G. 2007, ApJ, 658, 710

Navarro, J. F., & Benz, W. 1991, ApJ, 380, 320

Navarro, J. F., & White, S. D. M. 1993, MNRAS, 265, 271

Navarro, J. F., & White, S. D. M. 1994, MNRAS, 267, 401

Navarro, J. F., Frenk, C. S., & White, S. D. M. 1995, MNRAS, 275, 56

Navarro J. F., Frenk C. S., White S. D. M., 1997, ApJ, 490, 493

Navarro, J. F., & Steinmetz, M. 1997, ApJ, 478, 13

Navarro, J. F., & Steinmetz, M. 2000, ApJ, 538, 477

Navarro, J. F., et al., 2004, MNRAS, 349, 1039

Netterfield, C. B., et al., 2002, ApJ, 571, 604

Norman, C. A., & Ikeuchi, S. 1989, ApJ, 345, 372

Okamoto, T., Eke, V. R., Frenk, C. S., & Jenkins, A. 2005, MNRAS, 363, 1299

Oppenheimer, B. D., & Davé, R. 2006, MNRAS, 373, 1265

O'Shea, B. W. et al., 2004, arXiv:astro-ph/0403044

Peacock, J. A., & Dodds, S. J. 1996, MNRAS, 280, L19

Peebles, P. J. E. 1970, AJ, 75, 13

Persic M., Salucci P., Stel F., 1996, MNRAS, 281, 27

Poveda, A., Ruiz, J., & Allen, C. 1967, Boletin de los Observatorios Tonantzintla y Tacubaya, 4, 86

Prada, F., et al., 2006, ApJ, 645, 1001

Press, W. H., & Schechter, P. 1974, ApJ, 187, 425

Quinn, T., Katz, N., & Efstathiou, G. 1996, MNRAS, 278, L49

Rees M.J., Ostriker J.P., 1977, MNRAS, 179, 541

Robertson, B., Yoshida, N., Springel, V., & Hernquist, L. 2004, ApJ, 606, 32

Robertson, B., Bullock, J. S., Cox, T. J., Di Matteo, T., Hernquist, L., Springel, V., & Yoshida, N. 2006, ApJ, 645, 986

Robertson, B., & Kravtsov, A. 2007, ArXiv e-prints, 710, arXiv:0710.2102

Rosen, A., & Bregman, J. N. 1995, ApJ, 440, 634

Rosolowsky, E., Keto, E., Matsushita, S., & Willner, S. P. 2007, ApJ, 661, 830

Rubin, V. C., Ford, W. K. J., & . Thonnard, N. 1980, ApJ, 238, 471

Sheth, R. K. & Tormen, G., 1999, MNRAS, 308, 119

Sheth, K., Vogel, S. N., Wilson, C. D., & Dame, T. M. 2008, ApJ, 675, 330

Silk J., 1977, ApJ, 211, 638

Simon, J. D., Bolatto, A. D., Leroy, A., Blitz, L., & Gates, E. L. 2005, ApJ, 621, 757

Scalo, J., Vazquez-Semadeni, E., Chappell, D., & Passot, T. 1998, ApJ, 504, 835

Scott, J., Bechtold, J., Morita, M., Dobrzycki, A., & Kulkarni, V. P. 2002, ApJ, 571, 665

Skokøs Ch., Patsis P.A., Athanassoula E., 2002, MNRAS, 333, 847

Slyz, A. D., Devriendt, J. E. G., Bryan, G., & Silk, J. 2005, MNRAS, 356, 737

Somerville, R. S., & Primack, J. R. 1999, MNRAS, 310, 1087

Sommer-Larsen, J., Gelato, S., & Vedel, H. 1999, ApJ, 519, 501

Sommer-Larsen, J., Götz, M., & Portinari, L. 2003, ApJ, 596, 47

Spergel, D. N., et al. 2007, ApJS, 170, 377

Spitzer, L. J. 1990, ARA&A, 28, 71

Springel, V., Yoshida, N., & White, S. D. M. 2001, New Astronomy, 6, 79

Springel, V., & Hernquist, L. 2003, MNRAS, 339, 289

Springel, V., & Hernquist, L. 2005, ApJL, 622, L9

Springel, V., et al., 2005, Nature, 435, 629

Steidel, C. C. et al., 2007, in preparation

Stone, R. C. 1991, AJ, 102, 333

Tasker, E. J., & Bryan, G. L. 2006, ApJ, 641, 878

Tegmark, M., et al., 2004, ApJ, 606, 702

Thacker, R. J., & Couchman, H. M. P. 2000, ApJ, 545, 728

Tinker, J. et al., 2008a, in preparation

Toomre, A., & Toomre, J. 1972, ApJ, 178, 623

Townsley, L. K., Feigelson, E. D., Montmerle, T., Broos, P. S., Chu, Y.-H., & Garmire, G. P. 2003, ApJ, 593, 874

Tremaine S., Weinberg M.D., 1984, MNRAS, 209, 729

Truelove, J. K., Klein, R. I., McKee, C. F., Holliman, J. H., II, Howell, L. H., & Greenough, J. A. 1997, ApJL, 489, L179

Tully R. B., Fisher J. R., 1977, A&A, 54, 661

Valenzuela O., Klypin A., 2003, MNRAS, 345, 406

Valenzuela, O., Rhee, G., Klypin, A., Governato, F., Stinson, G., Quinn, T., & Wadsley, J., 2007, ApJ, 657, 773

van Leer, B. 1979, Journal of Computational Physics, 32, 101

Vázquez-Semadeni, E., Passot, T., & Pouquet, A. 1995, ApJ, 441, 702

Vázquez-Semadeni, E., Ballesteros-Paredes, J., & Klessen, R. S. 2003, ApJL, 585, L131

Vitvitska, M., Klypin, A. A., Kravtsov, A. V., Wechsler, R. H., Primack, J. R., & Bullock, J. S. 2002, ApJ, 581, 799

Voglis N., Tsoutsis P., Efthymiopoulos C., 2006, MNRAS, 373, 280

Wada, K., & Norman, C. A. 2001, ApJ, 547, 172

Wada, K., & Norman, C. A. 2007, ApJ, 660, 276

Wadsley, J. W., Stadel, J., & Quinn, T. 2004, New Astronomy, 9, 137

Walker, M. G., et al., 2007, ApJL, 667, L53

Wang, J., Townsley, L. K., Feigelson, E. D., Broos, P. S., Getman, K. V., Roman-Zuniga, C., & Lada, E. 2007, ArXiv e-prints, 711, arXiv:0711.2024

Warren, M. S., Abazajian, K., Holz, D. E., & Teodoro, L. 2006, ApJ, 646, 881

Weinberg, M. D., 2004, preprint (astro-ph/0404169)

Weinberg M. D., Katz N., 2007a, MNRAS, 1499

Weinberg M. D., Katz N., 2007b, MNRAS, 1500

White, S. D. M., & Frenk, C. S. 1991, ApJ, 379, 52

White, S. D. M. 1976, MNRAS, 177, 717

White, S. D. M., & Rees, M. J. 1978, MNRAS, 183, 341

Wood M. A., 1992, ApJ, 386, 539

Woosley S. E., Weaver T. A., 1995, ApJS, 101, 181

Yepes, G., Kates, R., Khokhlov, A., & Klypin, A. 1997, MNRAS, 284, 235

Zuckerman, B., & Evans, N. J., II 1974, ApJL, 192, L149

Zwicky, F. 1957, Berlin: Springer, 1957,